

THE NATURE OF THE METAL-MOLECULE
INTERFACE REVEALED THROUGH
TUNNELING SPECTROSCOPY

by

JUSTIN P. KREIL

GREGORY J. SZULCZEWSKI, COMMITTEE CHAIR

SHANE C. STREET

ARUNAVA GUPTA

SHANLIN PAN

PATRICK LECLAIR

A DISSERTATION

Submitted in partial fulfillment of the requirements
for the degree of Doctor of Philosophy
in the Department of Chemistry
in the Graduate School of
The University of Alabama

TUSCALOOSA, ALABAMA

2013

Copyright Justin Kreil 2013

ALL RIGHTS RESERVED

ABSTRACT

This dissertation describes the fabrication and characterization of molecular tunnel junctions made with a series of carboxylic acid derivatives chemisorbed to amorphous aluminum oxide (AlO_x) electrodes with a variety of top metal electrodes. Para-substituted benzoic acids, terminal-substituted long alkyl chain (C₁₆) alkanolic acids, and octadecylphosphonic acid were prepared on the native oxide of aluminum by a solution self-assembly technique.

The self-assembled monolayers (SAMs) were characterized via x-ray photoelectron spectroscopy (XPS) and water contact angles. For the benzoic acid derivatives, several trends became apparent. The polarity of the solvent used during self-assembly was critical to monolayer formation. Solvents that were polar and protic in nature produced low coverage monolayers. In contrast, non-polar solvents produced much higher coverage monolayers. The thickness of the monolayers determined via XPS suggests that the plane of the aromatic ring is perpendicular to the AlO_x surface with the carboxylate functional group chemisorbed in a bidentate chelating geometry. A similar

saturation coverage was achieved for each benzoic acid derivative at $\sim 2.7 \times 10^{14}$ molecules cm^{-2} . At saturation coverage, the benzoic acids and hydroxyls are present in an approximate ratio of 1:1. When Pb was vapor deposited on top of the benzoic acid derivatives and XPS measurements were obtained, only 4-SH benzoic acid showed a chemical reaction in the form of S-Pb. Au also showed a complete chemical reaction with 4-SH benzoic acid with a shift in the S(2s) peak 1.2 eV lower in binding energy indicative of a S-Au bond formation.

Contact angle and XPS results of the long alkyl chain SAM derivatives reveal a higher surface coverage of molecules on AlOx when compared to the benzoic acids. Electrical measurements including: I vs. V, dI/dV [normalized as $G(V)$] vs. V, and IETS were also obtained.

$G(V)$ measurements obtained on tunnel junctions without SAMs showed large offsets in the $G(V)$ minimum [$G(V)_{\text{min}}$] conductance due to polar hydroxyl groups native to the AlOx surface introducing large asymmetry in the barrier. Upon addition of the carboxylic and phosphonic acid monolayers, the $G(V)_{\text{min}}$ shifted closer to zero bias. For tunnel junctions made with benzoic acid SAMs and Pb, several trends emerged. First, as the coverage of the SAM increased, the $G(V)_{\text{min}}$ decreased. Second, as the size of the para-substituent increased, the $G(V)_{\text{min}}$ decreased. Finally

when a reactive para-substituent such as thiol is used, the barrier asymmetry is completely reversed due to a bond formation at the S-Pb interface.

$G(V)$ measurements obtained on various alkanolic acid SAMs showed no offset in the $G(V)_{\min}$. The data obtained was fit to a model to extract the tunnel barrier properties. The results showed that when a reactive terminal group such as thiol is used, the effective thickness of the tunnel barrier is larger than samples made with CH_3 terminated SAMs. This suggests that less of the top metal can penetrate through monolayers when a chemical reaction occurs at the metal-molecule interface. Data obtained for tunnel junctions made with octadecylphosphonic acid SAMs showed very little penetration of the top metal likely due to higher saturation coverage and better packing.

LIST OF ABBREVIATIONS AND SYMBOLS

\AA	Angstrom
ψ^2	Tunneling probability
x	Distance into tunneling barrier
m^*	Effective mass of an electron
$V(x)$	Height of tunneling barrier
$E(x)$	Energy of tunneling electron
K_B	Boltzmann constant
d	Effective barrier thickness
$\bar{\phi}$	Average barrier height
$\Delta\phi$	Barrier asymmetry
I	Current
V	Voltage
mV	Millivolts
dI/dV	Derivative of current and voltage, conductance
$G(V)$	Normalized conductance
cm	centimeter
AlOx	Nonstoichiometric amorphous aluminum oxide
ITO	Indium tin oxide
OLEDs	Organic light emitting diodes
R	Resistance

T	Temperature
IETS	Inelastic tunneling spectroscopy
PPMS	Physical property measurement system
°C	Degrees Celsius
PVD	Physical vapor deposition
QCM	Quartz crystal microbalance
M	Molarity (mol/Liter)
nm	Nanometer
XPS	X-ray photoelectron spectroscopy
KE	Kinetic energy
BE	Binding energy
eV	Electronvolts
GPIB	General-purpose interface bus
mA	Milliamps
mW	Milliwatts
s	Seconds
θ	Measured contact angle
f_1	Fractional coverage for a saturated monolayer
f_2	Fractional coverage for hydroxylated surface without SAM ($1-f_1$)
λ_{Al}	Inelastic mean free path of Al photoelectrons
UPS	Ultraviolet photoelectron spectroscopy
XRD	X-ray diffraction
DRS	Diffuse reflectance spectroscopy

ACKNOWLEDGEMENTS

This dissertation would not be possible without the support from many people.

First and foremost, I would like to thank God through which all things are possible.

I would like to thank my research advisor Dr. Gregory Szulczewski for his guidance, support, and encouragement throughout my time at UA. His strong work ethic and vibrant enthusiasm are unmatched by most. I will be forever grateful for all the help he has given me.

I would like to thank my research committee members Dr. Arunava Gupta, Dr. Shane Street, Dr. Shanlin Pan, and Dr. Patrick LeClair for all of their support. Particularly, I would like to thank Dr. Arunava Gupta for all of his help with my research seminar and Dr. Patrick LeClair for his countless hours teaching me the electrical measurements and giving me guidance through helpful discussion.

I also thank the Department of Chemistry, the Graduate School, and The University of Alabama for giving me this amazing opportunity.

Furthermore, I would like to acknowledge all of my current and former group members including Dr. Weihao Xu, Dr. Jian Tang, Dr. Jon Brauer, Ed Ellingsworth, and Kim Anderson. They have all made countless contributions to this dissertation.

Finally I would like to thank my wife, family, and friends. Trina has been with me through countless trials and tribulations and always supported me without hesitation. I cannot thank her enough for her sacrifice, love, and encouragement. My father, who is my best friend, has supported me and taught me to be a better person. I also thank my mother for her love and encouragement and my sisters for their support.

CONTENTS

ABSTRACT.....	ii
LIST OF ABBREVIATIONS AND SYMBOLS.....	v
ACKNOWLEDGEMENTS.....	vii
LIST OF TABLES.....	xii
LIST OF FIGURES.....	xiii
CHAPTER 1 - INTRODUCTION.....	1
1.1 Basic Physics of Electron Tunneling.....	1
1.2 Organic Molecules in Tunnel Junctions.....	6
1.3 SAMs in Electrical Devices.....	11
1.4 The Metal-Molecule Interface.....	13
1.5 Issues with Top Contacts.....	13
1.6 Outline of Dissertation.....	15
CHAPTER 2 - EXPERIMENTAL METHODS.....	18
2.1 Introduction.....	18
2.2 Device Fabrication.....	18
2.2.1 Substrate Processing.....	18
2.2.2 Film Deposition.....	19
2.2.3 Addition of Organic Molecules into Tunnel Junctions.....	21
2.2.3.1 Spin-Coating of Organic Molecules on AlOx.....	22

2.2.3.2 Self-Assembled Monolayers (SAMs) on AlO _x	22
2.3 Characterization of SAMs on AlO _x	23
2.2.3.1 Contact Angle Measurements.....	23
2.2.3.2 X-ray Photoelectron Spectroscopy.....	25
2.4 Electrical Characterization Methods.....	29
2.4.1 Current (I) vs. Voltage (V) and dI/dV vs. V...	29
2.4.2 Inelastic Tunneling Spectroscopy.....	32
2.4.3 Resistance vs. Temperature Measurements.....	33
 CHAPTER 3 - SURFACE CHARACTERIZATION OF CARBOXYLIC ACID DERIVATIVES ON AMORPHOUS ALUMINUM OXIDE FILMS.....	 35
3.1 Introduction.....	35
3.2 Contact Angle Measurements of SAMs on AlO _x	35
3.3 XPS Study of Benzoic Acid Derivatives.....	43
3.4 XPS of Benzoic Acids with Pb or Au Vapor Deposited...	55
3.5 XPS of Alkanoic and Phosphonic Acid Derivatives.....	60
3.6 Conclusions.....	65
 CHAPTER 4 - TUNNELING SPECTROSCOPY OF BENZOIC ACID DERIVATIVES.....	 68
4.1 Introduction.....	68
4.2 Hydroxylated Aluminum Oxide Surfaces and Tunnel Junctions.....	69
4.3 Benzoic Acid SAMs with Pb Top Electrodes.....	72
4.4 Benzoic Acid SAMs with Ag Top Electrodes.....	90
4.5 Benzoic Acid SAMs with Au Top Electrodes.....	95
4.6 Conclusions.....	100

CHAPTER 5 - TUNNELING SPECTROSCOPY OF ALKANOIC ACID MONOLAYERS.....	101
5.1 Introduction.....	101
5.2 Alkanoic and Phosphonic Acid SAMs in Tunnel Junctions.....	103
5.3 Alkanoic Acid Tunnel Junctions with Co Top Electrodes.....	104
5.4 Alkanoic Acids with Ni and Ag Top Electrodes.....	108
5.5 Tunnel Junctions Made with Octadecylphosphonic Acid.....	114
5.6 Conclusions.....	116
CHAPTER 6 - CONCLUSIONS AND FUTURE WORK.....	117
6.1 Conclusions.....	117
6.2 Future Work.....	119
REFERENCES.....	121

LIST OF TABLES

Table 3.1: Contact angle measurements obtained for spin coating and self assembly of benzoic acids on AlOx.....	38
Table 3.2: Contact angle measurements for various para-substituted halogenated benzoic acid derivatives. Solution concentration was 10^{-6} M.....	40
Table 3.3: Contact angle measurements for various benzoic acid derivatives on AlOx. Each measurement was taken after a 10^4 s exposure to a 10^{-3} M solution.....	41
Table 3.4: Table of XPS C (1s) binding energies for various carbon species and the halogen to Al^{3+} ratio for the various para-substituted benzoic acid SAMs.....	53
Table 4.1: Table of peak positions and their respective vibrational assignments for 4-F benzoic acid. The reference positions are obtained from reference 18.....	74
Table 4.2: Table of peak positions and their respective vibrational assignments for 4-SH benzoic acid. The reference positions are obtained from reference 112.....	87
Table 4.3: Summary of the values obtained from the Brinkman model for tunneling through benzoic acid SAMs.....	94
Table 5.1: Summary of Brinkman model parameters for heptadecanoic acid and mercaptohexadecanoic acid SAMs with Co, Ni, or Ag top electrodes.....	107

LIST OF FIGURES

Figure 1.1: Diagram of quantum tunneling of an electron through a barrier. (a) The barrier is too thick and the wave function decays. (b) If the barrier is thin enough, then the electron has some probability of tunneling through to the other side.....	3
Figure 1.2: Schematic diagram for a metal-insulator-metal tunnel junction. (a) A rectangular tunnel barrier with barrier heights equal on each side and thus no asymmetry. (b) A trapezoidal tunnel barrier with asymmetry.....	4
Figure 1.3: Schematic diagram of benzoic acid SAMs chemisorbed to an AlO _x substrate.....	8
Figure 2.1: A schematic diagram of the vapor deposition system.....	20
Figure 2.2: (a). Cross sectional diagram of samples made. (b) Top down view of samples made with wiring for electrical characterization.....	24
Figure 2.3: Photograph of Ramé-Hart system.....	26
Figure 2.4: Schematic diagram of the X-ray photoelectron generation. The difference between E_{vac} and E_f is due to the spectrometer work function.....	27
Figure 2.5: Experimental setup for electrical measurements in Patrick LeClair's lab.....	30
Figure 2.6: Schematic of IETS setup in the LeClair laboratory.....	31
Figure 2.7: Schematic drawing of current vs. voltage, dI/dV , and d^2I/dV^2 . The second derivative corresponds to molecular vibrations in tunnel junctions.....	34
Figure 3.1: Survey spectra of para-substituted halogenated benzoic acid SAMs on AlO _x	44

Figure 3.2: Survey spectra for 4-CN and 4-SH benzoic acid on AlOx substrates.....	45
Figure 3.3: High resolution spectra of the Al (2p) region for an Al surface with 4-Cl benzoic acid (a) and for an Al surface with no SAM (b). The peak at 75.4 eV is from the Al ³⁺ (2p) and the peak at 72.8 eV is the Al ⁰ (2p) peak.....	47
Figure 3.4: High-resolution spectra of halogen regions for halogenated SAMs on AlOx.....	48
Figure 3.5: High-resolution spectra for the N (1s) region for 4-CN benzoic acid (a) and the S (2p) region for 4-SH benzoic acid (b).....	50
Figure 3.6: High-resolution spectra of the C (1s) region for para-substituted halogenated benzoic acid SAMs. Raw data is shown in black dots. Fit data for the varying C(1s) species are shown as: C-O at highest binding energy, C-X middle binding energy, and C-H at lowest binding energy.....	51
Figure 3.7: Schematic diagram for benzoic acid derivatives chemisorbed to an AlOx surface at saturation coverage.....	54
Figure 3.8: High-resolution XPS spectra of Pb(4f) region for SAMs with 1 Å of Pb deposited.....	56
Figure 3.9: High-resolution XPS spectra of various halogen regions of benzoic acid SAMs with (dash) and without (solid) 1 Å of Pb deposited. A pass energy of 80 eV was used for the 4-Cl SAM with 1 Å of Pb to. All other spectra were recorded with pass energies set to 40 eV.....	58
Figure 3.10: High-resolution XPS of the S(2p) region for 4-SH benzoic acid (black) and after Pb deposition: 1Å (red), 2Å (blue), and 3Å (green).....	59
Figure 3.11: XPS of the S(2s) region for 4-SH SAM (black) without and with 6 Å Au (red) vapor deposited.....	61
Figure 3.12: Survey spectra of (a) heptadecanoic acid, (b) mercaptohexadecanoic acid, and (c) octadecylphosphonic acid...	62

Figure 3.13: High-resolution XPS of the C (1s) region for heptadecanoic acid (a), mercaptohexadecanoic acid (b), and octadecylphosphonic acid (c). Raw data is shown as dots. Fitting for C-H (red), C-O (blue), and C-X (green), where X = (3.13a) C-contamination, (3.13b) C-S, (3.13c) C-P.....	63
Figure 3.14: High-resolution XPS spectrum for the P (2p) region for octadecylphosphonic acid.....	66
Figure 4.1: G(V) spectrum for a representative air oxidized Al/AlO _x /Pb tunnel junction.....	71
Figure 4.2: IETS of 4-F benzoic acid with Pb top electrodes taken at 4K with a 5 mV ac modulation.....	73
Figure 4.3: G(V) for tunnel junctions containing 4-I SAMs after exposure to a 10 ⁻⁴ M 4-I solution for 10, 100, 1,000, and 10,000 seconds.....	76
Figure 4.4: G(V) _{min} shift (open circles) and contact angle (dots) vs. exposure time to a 10 ⁻⁴ M solution for 4-I benzoic acid....	77
Figure 4.5: G(V) for 4-F, 4-Cl, 4-Br, and 4-I respectively....	79
Figure 4.6: G(V) _{min} shift (open circles) and van der Waals radius (dots) for the various halogenated benzoic acid derivatives with Pb top electrodes.....	80
Figure 4.7: Schematic diagram of Pb penetration after vapor deposition for 4-F (a) and 4-I (b) SAMs. Much of the Pb penetrates through a 4-F SAM and adsorbs on the polar hydroxyl groups while very little Pb penetrates the 4-I SAM.....	81
Figure 4.8: G(V) for 4-CN benzoic acid with Pb top electrodes.....	83
Figure 4.9: G(V) for 4-SH benzoic acid with Pb top electrodes.....	85
Figure 4.10: IETS of 4-SH with Pb top electrodes taken at 3K with a 10 mV ac modulation.....	86
Figure 4.11: Schematic diagram of overall barrier shape for tunnel junctions with: no SAM (a), halogen-substituted benzoic acid SAMs (b), and 4-SH benzoic acid (c). The barrier asymmetry for (b) varies depending on how much of the Pb penetrates through the SAM and adsorbs on the polar hydroxyl groups.....	89

Figure 4.12: G(V) for 4-F, 4-Cl, 4-Br, and 4-I with Ag top electrodes. All have G(V) _{min} near zero bias.....	92
Figure 4.13: G(V) for 4-CN benzoic acid with Ag top electrodes.....	93
Figure 4.14: G(V) for tunnel junctions of 4-I benzoic acid with Au top electrodes. Exposure to a 10 ⁻⁴ M solution of 4-I was varied from 10, 100, and 1000s. Arrow indicates G(V) _{min}	96
Figure 4.15: G(V) for 4-SH benzoic acid with Au top electrodes.....	98
Figure 4.16: IETS of 4-SH benzoic acid with Au top electrodes taken at 4K with an 8 mV ac modulation.....	99
Figure 5.1: G(V) for heptadecanoic acid (a) and mercaptohexadecanoic acid (b) with Co top electrodes.....	106
Figure 5.2: Log of resistance for all junctions with heptadecanoic acid (a) and mercaptohexadecanoic acid (b) made with Co top electrodes.....	109
Figure 5.3: Schematic diagram of Co penetration into heptadecanoic acid SAMs (a) and mercaptohexadecanoic acid (b). Diagram is not to scale.....	110
Figure 5.4: G(V) for heptadecanoic acid (a) and mercaptohexadecanoic acid (b) SAMs made with Ni top electrodes.....	111
Figure 5.5: G(V) for heptadecanoic acid (a) and mercaptohexadecanoic acid (b) with Ag top electrodes.....	113
Figure 5.6: G(V) for octadecylphosphonic acid with Co top electrodes.....	115

CHAPTER 1 - INTRODUCTION

In this chapter the basic physics of electron tunneling will be introduced to provide the necessary background information to understand the work described in this dissertation. The second half of this chapter will be dedicated to the modification of amorphous aluminum oxide surfaces by adsorption of carboxylic acid derivatives. Since this dissertation is based on the study of electron tunneling through organic monolayers, the advantages of placing organic molecules in tunnel junctions for basic research and the motivations to study this will be offered. Most of the focus will be made on experiments with alkanolic and phosphonic acid monolayers used in electrical devices. The focus will be on gaining a better understanding of the metal-molecule interface. The chapter ends with an outline of this dissertation.

1.1 Basic physics of Electron Tunneling

According to classical physics, an electron that encounters a potential energy barrier greater than its kinetic energy will be repelled. However, due to the quantum mechanical nature of matter, an electron has some probability of tunneling through

the energetic barrier as long as it is sufficiently thin enough. The nature of quantum tunneling is based on the electron's wave-like behavior.¹ The wave-like behavior is described by the electron's wave-function. The wave-function describes the probability of the electron existing on both sides of the potential barrier, see Figure 1.1. The tunneling probability (ψ^2) can be written in the following formula^{2,3}:

$$\psi^2(x) \propto e^{-kx} \quad (1.1)$$

$$k(x, E_x) = \sqrt{\frac{2m^*(V(x)-E_x)}{\hbar^2}} \quad (1.2)$$

where x is the distance into the barrier, m^* is the effective mass of an electron, $V(x)$ is the height of the barrier, and E_x is the energy of the electron in the direction perpendicular to the interface.

A simplistic example of electron tunneling is through a metal-vacuum-metal junction. When two metal electrodes are connected their Fermi levels align. There are two limiting types of tunnel barriers, as shown in Figure 1.2. The first case is when the barrier heights of each side are equal in energy. The other is when one side of the barrier is higher or lower than the other. As a bias is applied, electrons tunnel from the Fermi

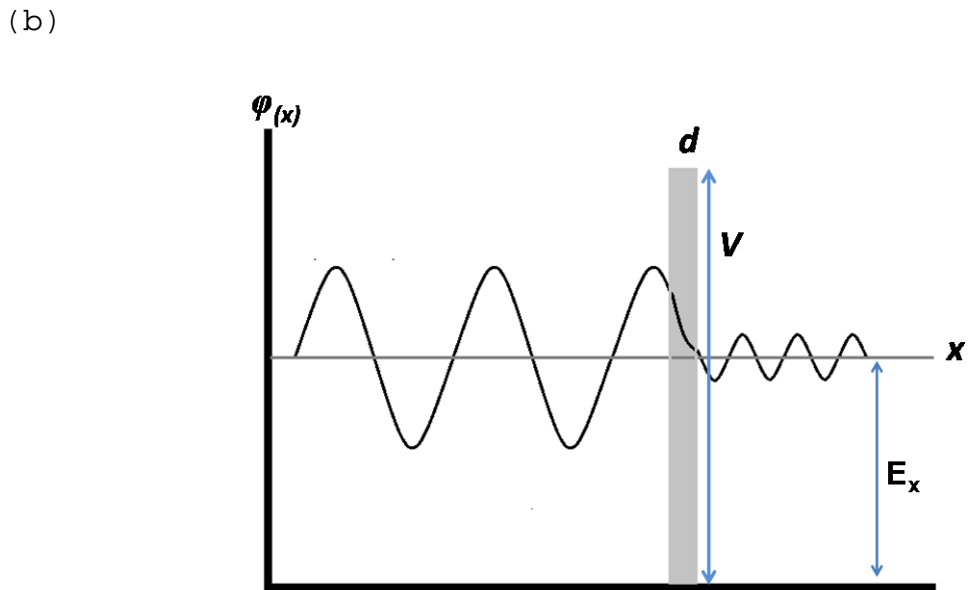
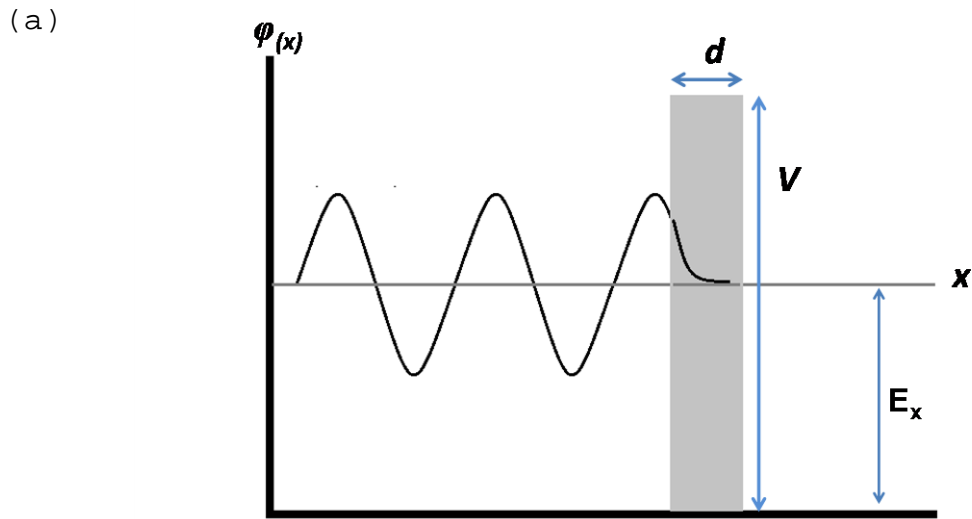
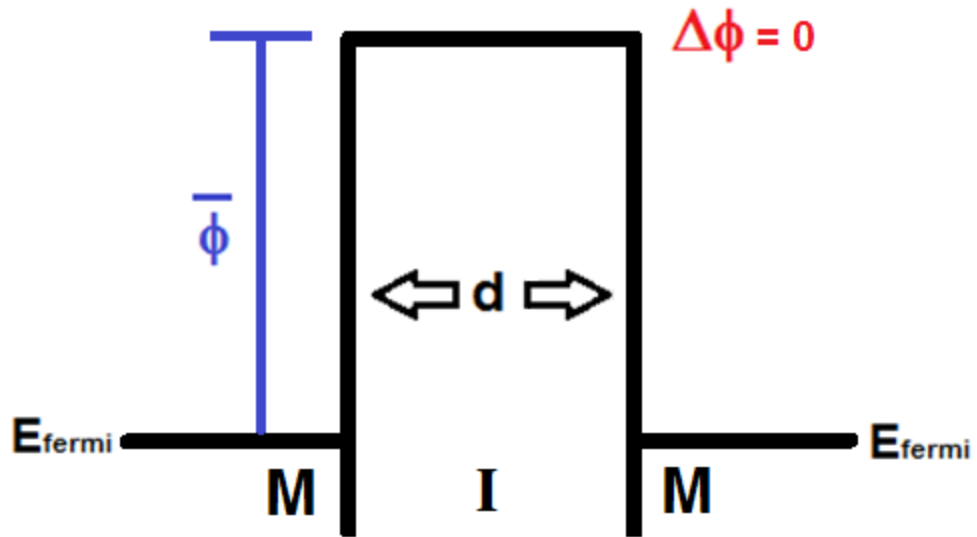


Figure 1.1. Diagram of quantum tunneling of an electron through a barrier. (a) The barrier is too thick and the wave function decays. (b) If the barrier is thin enough, then the electron has some probability of tunneling through to the other side.

(a)



(b)

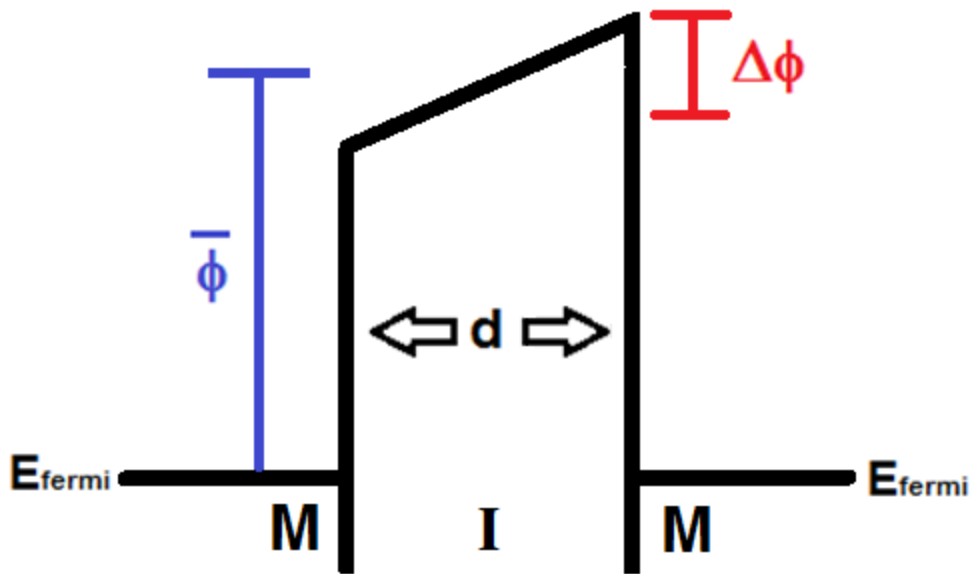


Figure 1.2. Schematic diagram for a metal-insulator-metal tunnel junction. (a) A rectangular tunnel barrier with barrier heights equal on each side and thus no asymmetry. (b) A trapezoidal tunnel barrier with asymmetry.

level of one electrode, through the insulating layer, and into empty states of the other metal electrode.

Giaever won the Nobel prize in physics for his work that demonstrated electron tunneling using superconducting Pb electrodes.⁴ Simmons was one of the first to bridge experimental tunneling data with a general theory.⁵ In his model, taking current/voltage measurements would allow the barrier width (d) and average barrier height ($\bar{\phi}$) to be calculated. Unfortunately, very few tunnel junctions have barrier heights that are equivalent (in energy) on both sides of the tunnel barrier and thus $\bar{\phi}$ only gives general information about the barrier. Brinkman *et al.* expanded upon the Simmons model to allow one to calculate the barrier asymmetry ($\Delta\phi$), or the difference in barrier heights, from current voltage measurements.⁶ This model will be referred to as the BDR model. To calculate the barrier parameters with the BDR model, one must obtain dI/dV measurements either via a lock-in amplifier or numerically. Once the measurements are made, the data is normalized so $dI/dV = G(V)/G(0) = 1$ at zero bias.⁶ The BDR model yields the following equation:

$$\frac{G(V)}{G(0)} = 1 - \left(\frac{A_0 \Delta\phi}{16\bar{\phi} \left(\frac{3}{2}\right)} \right) eV + \left(\frac{9}{128} \frac{A_0^2}{\bar{\phi}} \right) (eV)^2 \quad (1.3)$$

where $\Delta\phi = \phi_2 - \phi_1$, $A_0 = 4(2m)^{1/2}d/3\hbar$, and $G(0) = (3.16 \times 10^{10} \bar{\phi}^{1/2}/d \exp(-1.025 d \bar{\phi}^{1/2}))$. Using this model, the barrier width (d), average height ($\bar{\phi}$), and asymmetry ($\Delta\phi$) can be calculated. There are several limits to this model. The barrier thickness must be at least 10 Å, $\Delta\psi/\bar{\psi}$ must be less than 1, and the offset in minimum conductance [$G(V)_{\min}$] must be less than 50 mV. When a barrier is highly asymmetric the $G(V)_{\min}$ in the normalized conductance shifts from zero bias. This shift is proportional to the amount of asymmetry in the barrier.

1.2 Organic Molecules in Tunnel Junctions

Organic molecules have been widely used in tunnel junctions. Kuhn was the first to demonstrate transport through long alkyl "fatty acid" chains chemisorbed to aluminum oxide (AlOx) surfaces.⁷ He observed an exponential decrease in the current density with increasing alkyl chain length. This unequivocally demonstrated that the mode of transport through these molecules was by tunneling.

Once this important discovery was made, many other groups used a wide variety of alkanolic acid derivatives on surfaces and investigated their possible uses in tunnel junctions.⁸⁻¹⁴ The carboxylic acid group was shown to chemisorb in a bidentate fashion to AlOx through a carboxylate bond via an acid-base

reaction with surface hydroxyl groups.^{8,13-17} The evidence for carboxylate binding came from various inelastic tunneling spectroscopy (IETS) and infrared spectroscopy studies. The early IETS work showed the absence of the carbonyl stretching mode expected to be near 1700 cm^{-1} .¹⁸⁻²² Instead the characteristic modes for the asymmetric and symmetric stretching modes of a carboxylate group at $\sim 1560\text{ cm}^{-1}$ and 1450 cm^{-1} were observed. Figure 1.3 illustrates the carboxylic acid SAMs chemisorbed to AlOx surfaces. Once the mode of binding was verified, other groups followed up with further studies.²³⁻²⁵

Other carboxylic acids adsorbed to AlOx substrates included alkanolic acids of various chain lengths. Alkanolic acids placed on surfaces via self assembly adsorb kinetically via a Langmuir isotherm.⁹ The molecular packing and coverage on the surface is extremely dense.^{8-10,23} Contact angle measurements confirmed this with values between 97 to 115° . In general at low coverage, alkanolic acids lay flat on the surface. As the coverage increases, the SAMs stand perpendicular to the surface with a tilt between 10 to 25° from surface normal.⁸⁻¹⁰ Intermolecular interactions between molecules assists in packing and rearrangement to form dense monolayers. When alkanolic acid SAMs are placed in tunnel junctions, increasing the chain length decreases the tunneling current demonstrating tunneling as the mode of transport.²⁴

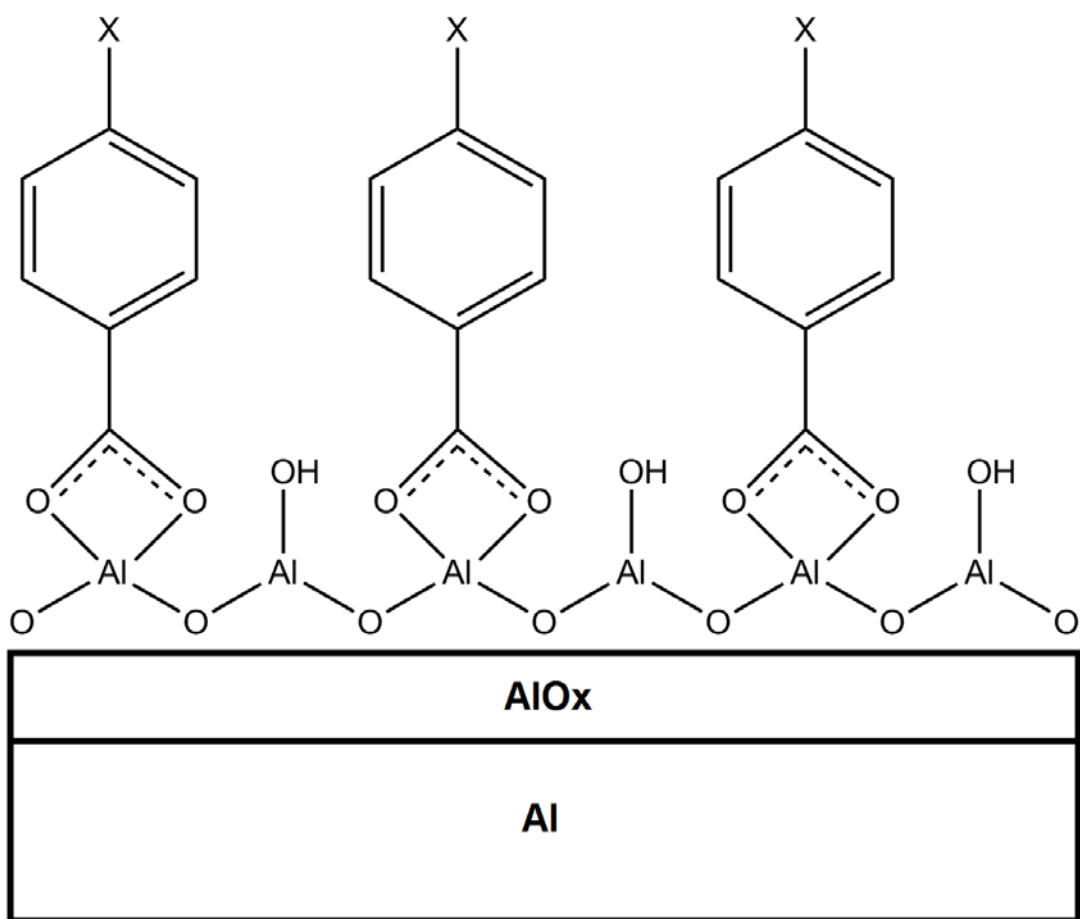


Figure 1.3. Schematic diagram of benzoic acid SAMs chemisorbed to an AlOx substrate.

Benzoic acids were another class of carboxylic acid derivatives studied extensively using IETS.¹⁸⁻²² Much was learned about this class of molecules. Using a multiple specular reflectance IR method, one group was able to monitor the intensity of the carboxylate modes for 4-bromobenzoic acid from sub-monolayer to monolayer coverage.¹⁸ They observed the intensity of the symmetric band increased as coverage increased, while the intensity of the asymmetric band was considerably lower and did not increase with coverage. The transition dipole moment of the symmetric carboxylate stretch is orientated primarily in the plane of the aromatic ring.²⁵ Consequently they determined that the molecule is oriented with the aromatic ring perpendicular to the surface even at sub-monolayer coverage. They discovered similar results with other benzoic acids derivatives. Other groups used IETS to study benzoic acid derivatives on AlOx.¹⁹⁻²² They observed peaks for all other vibrational modes of the molecules. This confirmed that the molecules remained completely intact when placed inside a tunnel junction.

Benzoic acid derivatives have also been shown to modify the electronic properties of various surfaces. One group showed that the work function of indium tin oxide (ITO) and AlOx was modified when benzoic acids were adsorbed.^{26,27} They used a Kelvin probe technique to measure the work function of benzoic acids

with various dipole moments and found a strong correlation between dipole moment and the change in the work function. As the dipole moment increased in electronegativity at the para substituent, the work function of ITO and AlOx increased. They measured an unmodified work function for AlOx to be 4.1 eV. They discovered that it could be tuned to 4.02 eV for molecules with positive dipoles facing away from the surface and up to 5.32 eV for ones with large negative dipoles facing vacuum.²⁷ Another group placed benzoic acid derivatives on GaAs and showed a decrease in the barrier height as the negativity of the dipole moment away from the GaAs surface increased.²⁸

Only minimal studies have been done to determine the surface coverage of benzoic acids on AlOx substrates.^{18,29} One group used neutron activation analysis and reported a coverage of 2.3×10^{14} molecules cm^{-2} .¹⁸ Another group used tritiated benzoic acid and a scintillation detector to measure coverage. They determined a saturation coverage of 6×10^{14} molecules cm^{-2} .²⁹ The latter value seems considerably high, however, as the saturation coverage of hydroxyl groups has been shown to be only 5×10^{14} hydroxyls cm^{-2} .³⁰

Another class of molecules placed on AlOx and investigated for possible uses in tunnel junctions is phosphonic acids. Phosphonic acids have been shown to bind with tridentate geometries via phosphonate bonds to oxide surfaces.³¹⁻³³ They have

been shown to pack extremely dense self assembled monolayers with typical contact angles of 100° or greater. Long chain phosphonic acid monolayers can also exhibit large tilt from the surface normal at approximately 35° due to bond angle constraints from the phosphonate binding group.³⁴ Due to the large tilt from the surface, the distance for tunneling is smaller than alkanolic SAMs. Defects in phosphonic acid SAMs have also decreased the effective tunnel distance.³⁵⁻³⁶ These defects are greater when the chain length is shorter and SAMs exhibit "liquid-like" behavior and have a higher probability of laying flat on the surface.³⁶ These defects are more prevalent when the chain length is less than 12 carbon atoms in length.³⁶ As the chain length increases, van der Waals interactions between molecules help to stabilize more crystalline growth perpendicular to the surface.^{35,36} Even in long chain phosphonic acid SAMs that are well packed, conformational defects still decrease the effective tunnel distance.

1.3 SAMs in Electrical Devices

Organic SAMs show much promise in new technologies. They have been used in organic light emitting diodes (OLEDs) to decrease the energy of hole and electron injection into electro-active layers by modifying the work function of metals.^{37,38} Aromatic SAMs have been used in organic field effect transistors

(OFETs) to improve charge injection and on/off ratios.³⁹ They have also been used in templates for covalent bonding in biosensors.⁴⁰

In recent years organic SAMs have been used in spintronic devices. Octanethiol SAMs have been used in molecular tunnel junctions in which low energy electrons pass through the molecular barrier while remaining spin polarized.⁴¹ Magnetoresistance as large as 30% has been reported in benzene dithiol tunnel junctions.³⁹ A range of other aromatic SAMs^{43,44} have also been used in organic spin valves with reports of magnetoresistance even at room temperature.⁴³ Finally, phosphonic acid SAMs have also shown to exhibit stable and efficient spin transport properties with TMR values as high as 35% at low temperatures.⁴⁵

The use of organic SAMs in devices has many advantages over pure inorganic devices. Organic SAMs have orbital energies that can be tuned for various applications.⁴⁶ Solution processing is far cheaper than most industrial applications that require high vacuum and ultra-clean rooms. Finally, the use of organic SAMs proves to be very beneficial to the environment as they can potentially break down easier in landfills. As a result, using organic SAMs in devices proves to be a promising avenue of research possibility.

1.4 The metal-Molecule Interface

Alkanethiols SAMs have also been studied in tunnel junctions by numerous groups.⁴⁷⁻⁵³ Alkanethiols chemisorb to Au and Ag via a thiolate bond. Experimental evidence confirms the mode of transport through the SAMs is tunneling.⁴⁸⁻⁵¹ The identity of the functional group facing the top metal electrodes has been shown to have a substantial effect on the tunneling characteristics of molecular tunnel junctions. Cui *et al.* studied how changing the functional group from CH₃ to SH influenced the tunneling characteristics when using an Au coated STM tip as a top electrode.⁵⁴ They found that when SH was used, the contact resistance was much lower than CH₃ terminated SAMs. When SH is used as the functional group, the top metal electrode chemisorbs to the heteroatom, thus increasing the tunneling current density. Similar observations have been made with other systems.⁵⁵⁻⁵⁸ Thus the nature of the metal molecule interface and whether it is chemisorbed vs. physisorbed is a critical factor in electron tunneling through SAMs.

1.5 Issues with Top Contacts

Alkanethiols exhibit similar problems as alkanic acid SAMs; even at high packing density conformational defects are present.^{59,60} When thermal evaporation is used to deposit a top electrode, the yield of non-shortened devices can be as low as

1%.⁵⁰ To limit the amount of penetration of the top metal electrode, some have used "reactive" terminal groups such as: COOH, COOCH₃, OCH₃, CN, and SH. Reactive groups decrease the penetration of vapor deposited top metals by interacting and forming metal complexes.⁵⁹⁻⁶⁰ Another method to limit the penetration is increasing the terminal group intermolecular interactions. One group used a K to modify alkanethiolate SAMs.⁶¹ The K increased the ionic interactions between terminal groups such as CO₂⁻, CH₃, and CO₂H. The increased ionic interaction between terminal groups decreased the amount of Au penetration into the SAMs.⁶¹

Various soft contacting methods have also been developed to limit the amount of shorting.^{49,51-55} These soft contact methods employ the use of GaIn or Hg drops to limit the amount of penetration into the SAM. Liquid metals are fine for fundamental studies but have very limited practical uses in real world electronic devices. A cheap and reliable method of placing the top metal electrode on tunnel junctions is needed.

In summary, organic SAMs can be excellent candidates for study in molecular tunnel junctions. A fundamental understanding of the metal-molecule interface is needed to assist in the development of future organic-based tunnel devices. Even though there have been some studies on how making small changes to an organic monolayer affects the tunneling characteristics of a

junction, there is still much to be learned. Motivated by this lack of fundamental understanding, the goal of this dissertation is focused on the effect metal-molecule interface on quantum tunneling of electrons through various SAMs including benzoic and alkanolic acids bonded to AlOx. Specifically, we would like to understand how varying the para substituent (atom facing the top metal electrode) influences the metal-molecule interface and how that affects the tunnel barrier.

In order to concisely refer to each molecule, the following notation will be used. Each benzoic acid derivative name will be shortened and called by its para-substituent. For example, 4-F benzoic acid will be referred to as 4-F. Additionally, the non-stoichiometric oxygen rich aluminum oxide will be labeled AlOx.

1.5 Outline of Dissertation

In this dissertation, electron tunneling through organic SAMs was investigated to gain a fundamental understanding of electron transport through similar SAMs with small changes to the para-substituents. The first part of the dissertation gave a brief overview of electron tunneling. A theoretical model on electron tunneling through asymmetric barriers was reviewed. The last part of this introduction provided an overview of how SAMs have been used in tunnel junctions and described their

advantages and disadvantages versus their pure inorganic counterparts.

In chapter 2, the device fabrication techniques used in this dissertation will be described, including: physical vapor deposition, spin-coating, and self-assembly. It will also discuss methods used to characterize SAMs on AlOx surfaces, including contact angle measurements and X-ray photoelectron spectroscopy. Finally, the electrical transport measurements will be discussed in great detail.

In chapter 3, surface characterization of the organic SAMs on AlOx will be presented, including: contact angle and XPS measurements. Contact angle data provides evidence that the SAMs chemisorb to the AlOx surface via an adsorption isotherm that can be modeled to a Langmuir isotherm. At saturation coverage, the surface coverage between benzoic acid derivatives is equivalent and approximately one molecule adsorbs to every two available surface sites.

In chapter 4, electrical characterization of benzoic acid derivatives will be presented. Here current vs. voltage measurements will be explained in terms of how the para-substituent effects the tunneling. Changes in the tunnel barrier properties will also be discussed with Pb, Au, and Ag top electrodes.

In chapter 5, electrical characterization of long chain alkanolic acids will be given. Current vs. voltage measurements will be presented and the resulting tunnel barrier properties will be discussed in terms of how the para-substituents effect the tunneling with Co, Ni, and Ag top electrodes.

In chapter 6 a summary and conclusions will be given. Finally, a brief statement about future experiments will be offered.

CHAPTER 2 - EXPERIMENTAL METHODS

2.1 Introduction

The experimental techniques and methods used in this dissertation will be described in this chapter. Section 2.2 covers device fabrication including substrate processing, film deposition, and addition of organic molecules into the junctions via self assembly. Section 2.3 discusses qualitative and quantitative chemical characterization of organic monolayers on aluminum oxide substrates including water contact angle measurements and XPS. Section 2.4 will cover characterization of organic molecular tunnel junctions by various electrical characterization methods, including current (I) vs. voltage (V), dI/dV vs. V, d^2I/dV^2 vs. V, and resistance (R) vs. temperature (T) measurements.

2.2 Device Fabrication

2.2.1 Substrate Processing

The first step for the fabrication of good tunnel junctions is to select an appropriate substrate. The substrate must be smooth and nonconductive but also, due to the number of samples being made, must be cost effective. For this reason, Si wafers

with 500nm of SiO₂ were obtained from Silicon Valley Microelectronics. The silicon wafers were spin-coated with 1818 acetone soluble photo-resist at 500rpm for 10 seconds and then 5000rpm for 5 minutes. The wafers were then dried at 100°C for 2 minutes. After that the wafers were then cut to 10mm by 10mm squares. Once cut, the individual pieces were cleaned by sonicating for 30 minutes in acetone at a temperature of 45°C. After that the samples were placed in isopropanol and sonicated for 20 minutes at 45°C. The wafers were then dried with nitrogen gas.

2.2.2 Film Deposition

Once all contaminants were removed from substrate cleaning, a shadow mask (1 mm x 10 mm cutouts) was placed over the samples. This mask was used to pattern bottom electrodes. Then the samples were loaded into a high vacuum chamber. High vacuum ($\sim 2 \times 10^{-7}$ Torr) was achieved with a diffusion pump with a liquid nitrogen trap backed up by a rough pump. The basic setup is shown in Figure 2.1.

Physical vapor deposition (PVD) was used to deposit all metals used in this work.⁶² The list of metals deposited includes: Pb, Ag, Au, Co, Ni, and NiFe. Each metal obtained had a purity of >99.9%. Metals were loaded into tungsten boats and the chamber was pumped down. Once the base pressure of the deposition chamber was approximately 2×10^{-7} Torr, a high

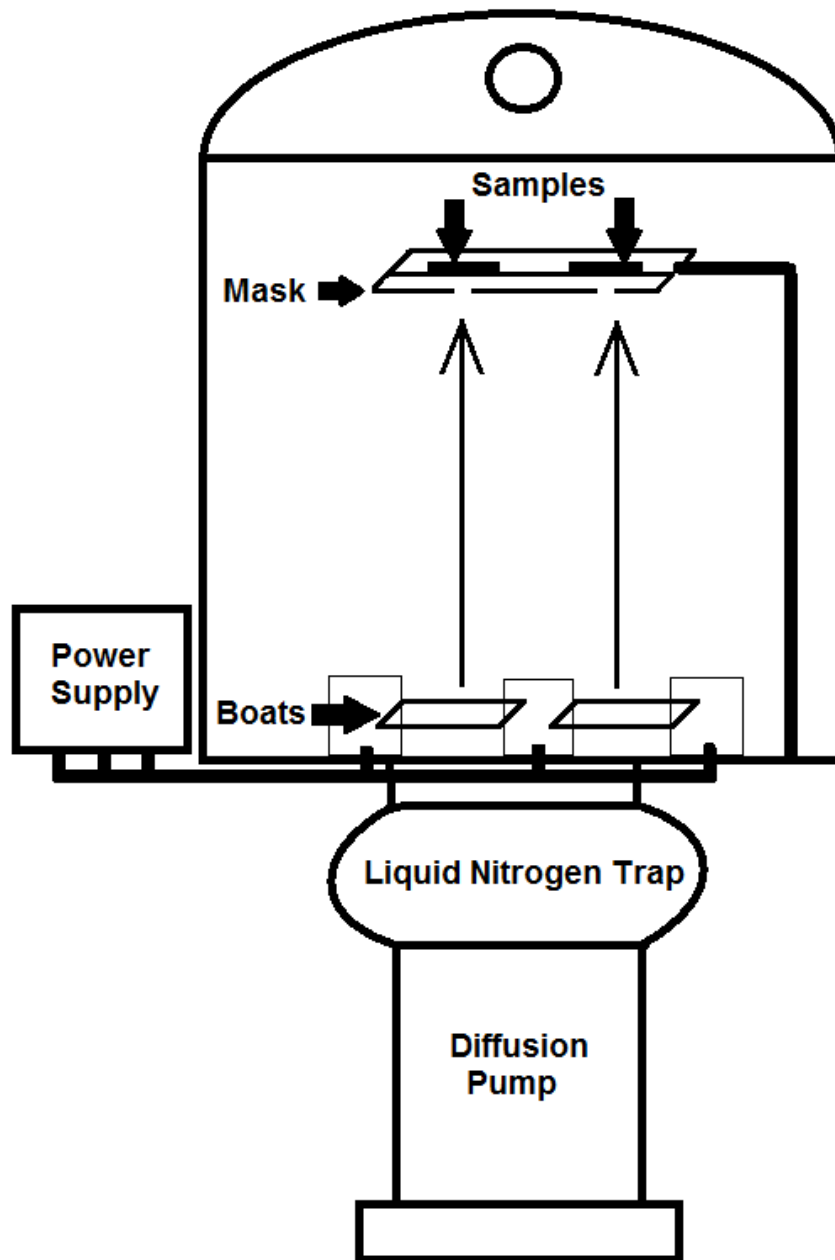


Figure 2.1. A schematic diagram of the vapor deposition system.

amount of current (100-150 amps) was applied to the tungsten boat containing the metal. The metal was subsequently heated until it melted and vapor deposited. To avoid cracking of the tungsten boats, the applied current to the tungsten boats was slowly brought up to the desired power setting. A quartz crystal microbalance (QCM) was used to monitor the deposition rate and total thickness of the deposited film. At first, the metal was deposited at a low rate ($\sim 0.2 \text{ \AA/s}$) until approximately 100 \AA was deposited. After that, the rate was ramped up to approximately 1 \AA/s . Once the deposition was completed, a shutter was used to block any additional metal from depositing on the substrate. The sample was then allowed to cool for approximately 20 minutes before the chamber was vented and the sample taken out.

Bottom aluminum electrodes were then oxidized in air for 10 minutes. The resulting AlO_x layer reached a self limiting thickness of approximately 23 \AA .^{63,64} Organic molecules were then adsorbed to the AlO_x in a method described in section 2.2.3.

2.2.3 Addition of Organic Molecules into Tunnel Junctions

Two methods were used to adsorb organic molecules on the surface of the AlO_x bottom electrodes. Various solutions contained the solute molecule (aryl and alkyl carboxylic acids) dissolved in a variety of solvents (benzene, acetonitrile, ethanol, or water). The molecules were placed in a jar containing the solvent and sonicated with heat at 45°C . This

assisted in dissolving the molecules more quickly. The concentrations of these solutions ranged from 10^{-3} M to 10^{-6} M. For most experiments, the 10^{-3} M concentration was used.

2.2.3.1 Spin-Coating of Organic Molecules on AlOx

The first method employed was a spin-coating procedure used by previous groups.^{19,65} In this method the sample was placed on a spin coater [CHEMAT TECHNOLOGY KW-4A] and vacuum sealed in place. Then 100 μ L of 10^{-3} M solutions of varying benzoic acids were drop-casted on top of a blanket 40 nm Al film with native oxide. The solution was spun off at 500 rpm for 8 seconds and then spun at 3000 rpm for 2 minutes. Contact angles of these samples were then taken immediately using the procedure described in section 2.3.1.

2.2.3.2 Self-Assembled Monolayers (SAMs) on AlOx

The second method used to dope organic molecules on AlOx surfaces was self-assembly. Carboxylic acids are known to self-assemble and chemisorb in a bidentate fashion to amorphous Al_2O_3 via a carboxylate bond.^{18,19} This occurs via reaction with native surface hydroxyl groups in an acid-base reaction. Benzoic acid (BA) molecules adsorb with the plane of the aromatic ring perpendicular to the surface regardless of surface coverage.¹⁹

The self assembly process is rather straightforward. A sample containing a 40 nm Al film with native oxide is placed into a solution described in Section 2.2.3. The molecules self-

assemble to the surface over time. Molecular surface coverage is dependent upon the concentration of the solution and the exposure time in solution.⁶³ Once taken out of the solution, the sample is then rinsed with solvent to remove any physisorbed molecules. The sample is then dried with pure nitrogen gas.

Once the SAMs were adsorbed on the AlOx, a second mask (3 stripes of 1 mm x 10 mm) was placed over the sample to obtain a cross-bar geometry and then loaded into a high vacuum chamber. A top metal (Ag, Au, Co, Ni, NiFe, or Pb) electrode was then deposited using the procedure described in Section 2.2.2. Sample geometries are shown in Figure 2.2.

Section 2.3 Characterization of SAMs on AlOx

Section 2.3.1 Contact Angle Measurements

Measuring contact angles allows one to determine whether a surface is relatively hydrophobic or hydrophilic in nature.⁶⁶ Contact angle measurements were performed using a Ramé-Hart system shown in Figure 2.3. A ~2 μ L drop of H₂O was placed on a sample containing molecules chemisorbed on AlOx. The contact angle of the water drop with respect to the surface was measured using a microscope. The larger the contact angle, the more hydrophobic the surface. This method was used as a quantitative way to determine relative molecular coverage via the Cassie equation.⁶⁶

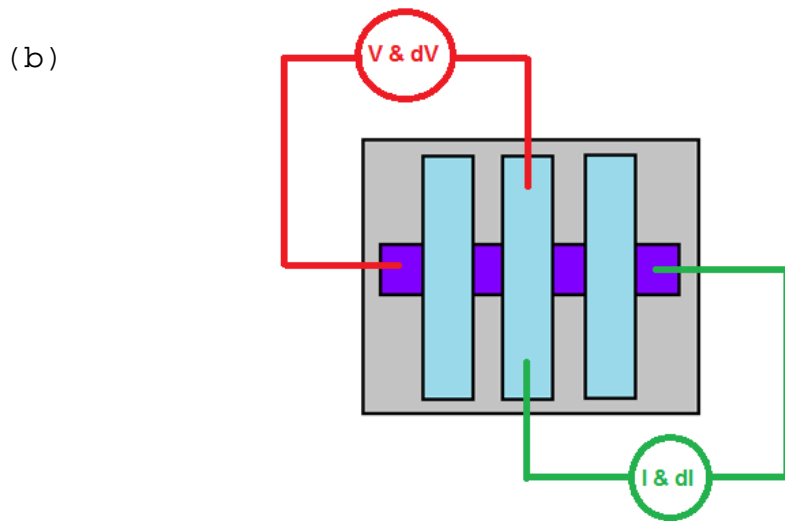
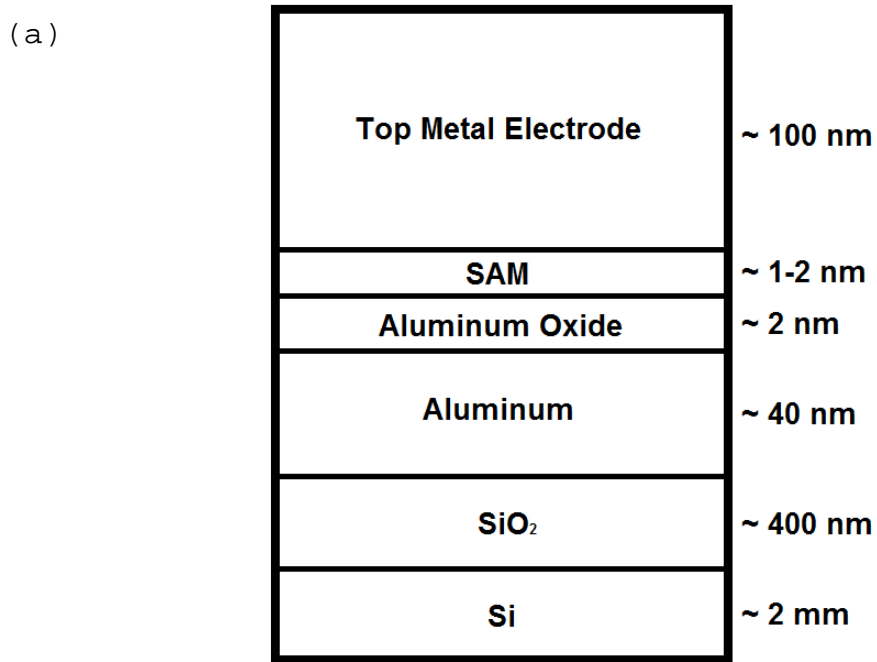


Figure 2.2. (a). Cross sectional diagram of tunnel junctions. (b) Top down view of samples made with wiring for electrical characterization.

Section 2.3.2 X-ray Photoelectron Spectroscopy

X-ray photoelectron spectroscopy (XPS) was used to characterize each SAM. XPS is a versatile surface sensitive technique.⁶⁷ We used this technique to determine the binding energies of the core levels for each element (except for hydrogen) in all of molecular monolayers.

XPS utilizes a monochromatic beam of x-rays to bombard surface species. The x-ray beam ionizes atoms on the surface and causes photoemission from both the core and valence level bands,⁶⁷ as shown in Figure 2.4. The kinetic energy (KE) of these photoelectrons depends upon the incident energy of the x-rays bombarding the sample ($h\nu$), the work function of the instrument (Φ), and the binding energy of the photoelectrons.

$$KE = h\nu - (BE + \Phi) \quad (2.1)$$

The binding energy (BE) is the amount of energy required to remove an electron from a core level and to the Fermi level. The binding energy is intrinsic to the specific atomic orbital from where the originated. Therefore, this energy will vary from element to element. The nature of the chemical environment will also influence the energy of the emitted photoelectron. Since some charge transfer occurs between bonded atoms, the binding energy of core level electrons depends upon what the atom is bonded to. Due to Coulombic attraction between core electrons

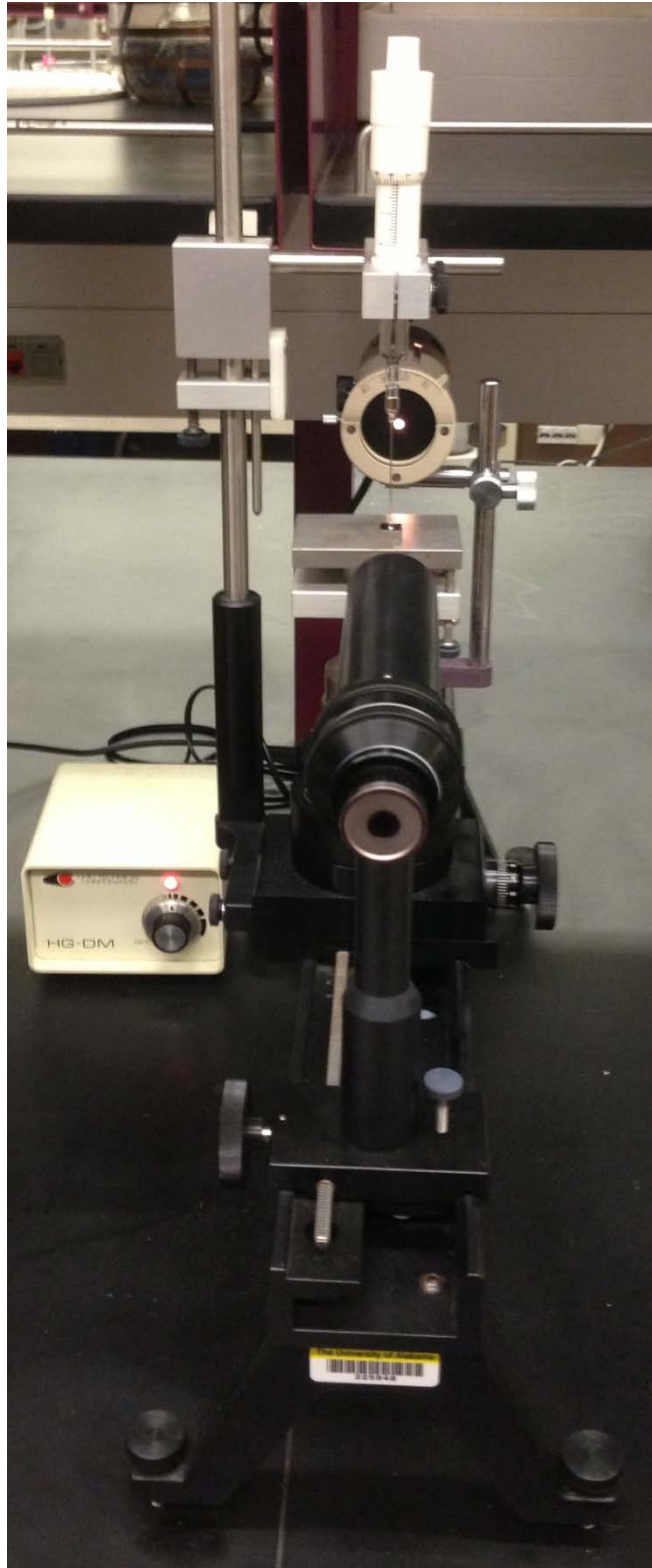


Figure 2.3. Photograph of Ramé-Hart system.

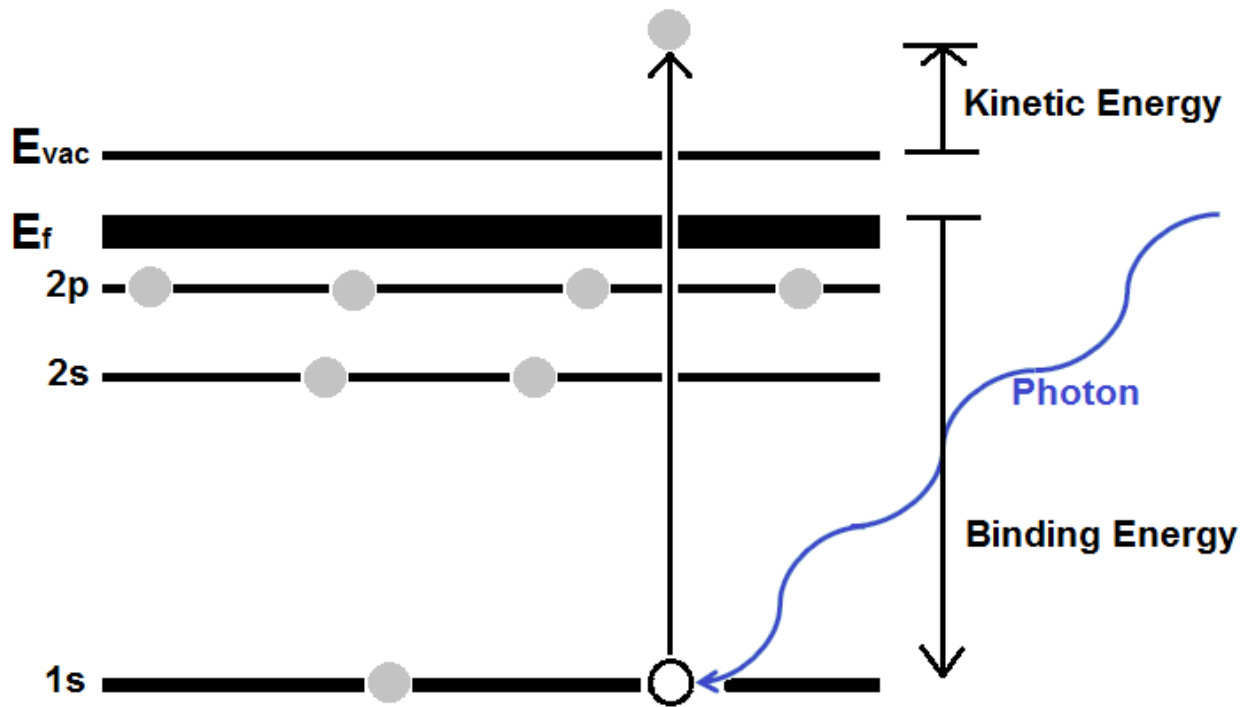


Figure 2.4. Schematic diagram of the X-ray photoelectron generation. The difference between E_{vac} and E_f is due to the spectrometer work function.

and the nucleus, the binding energy depends on whether the atom being analyzed is left with a partial negative or positive charge. Atoms with partial positive charges have larger Coulombic attraction between the core electrons and nucleus. Therefore, atoms with higher oxidative states have higher binding energies than those with lower oxidative states.⁶⁷

The kinetic energy of electrons emitted from a sample is measured with an electrostatic hemispherical analyzer. A potential difference is applied to create an electrostatic field. This electrostatic field is set to allow electrons of specific energies (the pass energy) to either pass through the hemisphere or be guided into the walls of the hemisphere (if their energy is too high or too small).⁶⁷

XPS measurements were made using a Kratos Axis 165 spectrometer using monochromatic Aluminum K_{α} x-rays. Survey spectra were taken for each SAM to check for contamination. Instrument settings for each survey scan included: 1050-0 eV BE range with a 0.5 eV step size, a dwell time of 300 ms, and a 160 eV pass energy. High-resolution spectra were obtained with a 0.1 eV step size, a 1500 ms dwell time, and 40 eV pass energy. All peaks were calibrated to the Al 10 ($2p_{3/2}$) peak at 72.8 eV.

Section 2.4 Electrical Characterization Methods

Section 2.4.1 Current (I) vs. Voltage (V) and dI/dV vs. V

Two methods were used to obtain I vs. V and dI/dV vs. V measurements on tunnel junctions. The first method was performed in the Greg Szulczewski lab. Samples were connected via a 4-point probe setup. Connecting a sample using the 4-point probe method negates any contact resistance due to wiring.⁶⁸ Here the bottom electrode was connected to the I^- and V^- leads while the top electrode was connected to the I^+ and V^+ leads. When a positive bias is applied, electrons tunnel from the bottom Al electrode towards the top metal electrode. A Keithley 2400 Sourcemeter was used to source a voltage across the sample while simultaneously measuring the current through the sample. A Labview program was developed to acquire the data and control the measurement process through a general-purpose interface bus (GPIB). The dI/dV was determined by taking numerical derivatives of I/V curves.

The second method used for electrical characterization of the tunnel junctions employed in Patrick LeClair's lab. A photograph of the setup is shown in Figure 2.5 and a schematic diagram of the setup is shown in Figure 2.6. This system included a Keithley 263 Source (K263) supplying the DC voltage (V_b). A Stanford 830 lock-in amplifier (SR830) was used to supply

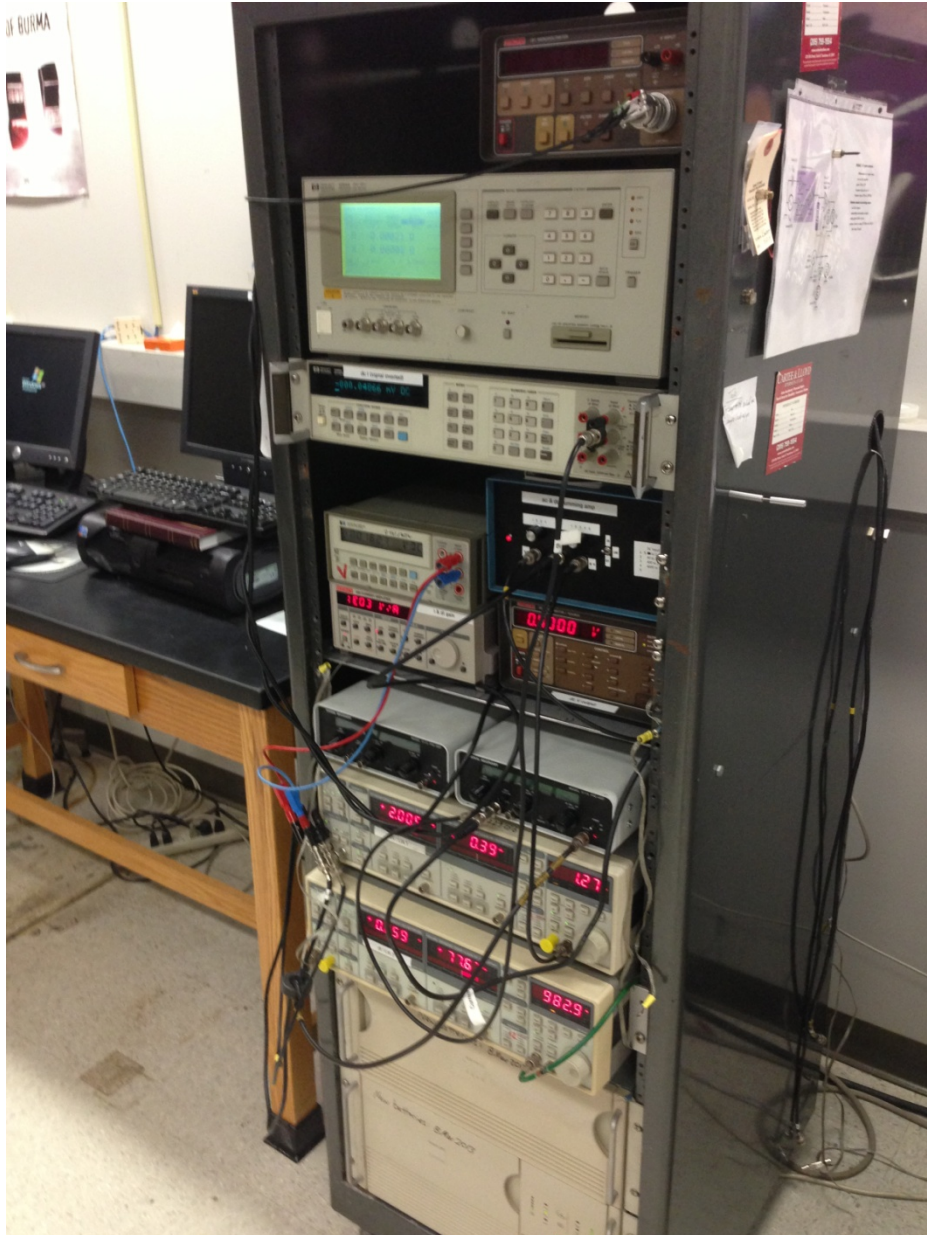


Figure 2.5. Experimental setup for electrical measurements in Patrick LeClair's lab.

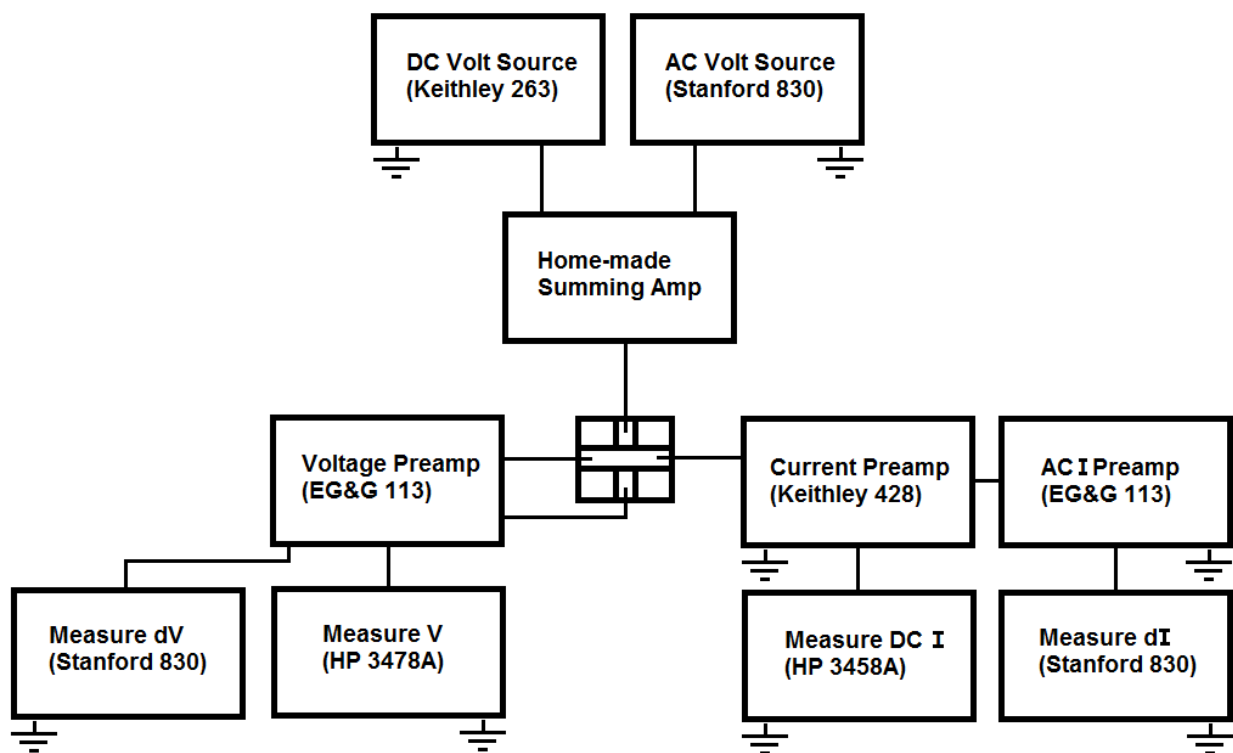


Figure 2.6. Schematic of IETS setup in the LeClair laboratory.

an AC modulation voltage, $V_m \cos (\omega_r t + \theta)$ (where ω is the modulation frequency), as a reference signal to the lock-in amplifiers. The two voltages were then added together via a summing amplifier and applied to the sample. Because the signal coming from the sample was extremely small, preamplifiers (EG&G PARC 113) were used to increase the signal intensity from the sample. The dc voltage portion of the signal was measured by a HP 3478A digital voltmeter, while the first harmonic of the ac voltage on the sample (dV part of dI/dV) was measured by a Stanford 830 lock-in amplifier (SR830). The dc current was measured by a HP 3458A digital voltmeter and the first harmonic of the ac current signal (the dI part of dI/dV) was measured by a Stanford Research 830 lock-in amplifier (SR830).

Section 2.4.2 Inelastic Tunneling Spectroscopy

Inelastic tunneling spectroscopy (IETS) is a method employed to measure vibrational spectra of molecules in tunnel junctions.⁶⁹⁻⁷² Most electrons tunnel through a barrier elastically (without losing any energy). Less than 1% of electrons tunnel through inelastically. These electrons lose some energy by exciting vibrational modes of molecules present inside the junction.⁶⁹⁻⁷² When the applied bias (V) is greater than or equal to the vibrational energy of the molecule ($h\nu/e$), additional inelastic tunnel channels open up. As these inelastic channels open, the total tunneling current increases slightly.

Figure 2.7 shows plots of I/V , first derivative (dI/dV), and second derivative (d^2I/dV^2), respectively. There are no selection rules for IETS. Typically vibrational modes from both Raman and Infrared (IR) will be observed.

In theory, a differential mathematical approach may be used to calculate d^2I/dV^2 . Unfortunately this is not feasible because the small current changes due to inelastic channels are on the same order of the noise of the measurements. Therefore, an AC modulation technique similar to the method used in Section 2.4.1 is used. Since IETS relies on measuring the second derivative of I/V , the LIA is set to measure the second harmonic ($\omega_r = 2\omega$) and $\theta_r = 90^\circ$ of the AC modulation reference signal $[V_m \cos(\omega_r t + \theta_r)]$.

Section 2.4.3 Resistance vs. Temperature Measurements

A physical property measurement system (Quantum Design PPMS Model 6000) was used for resistance vs. temperature measurements. In this system, the sample is cooled to temperatures as low as 3K using a liquid helium source. Resistance was recorded by the PPMS bridge at specific temperature intervals as the sample was cooled down. The current and power applied to the sample were limited to a maximum of 1 mA and 10 mW.

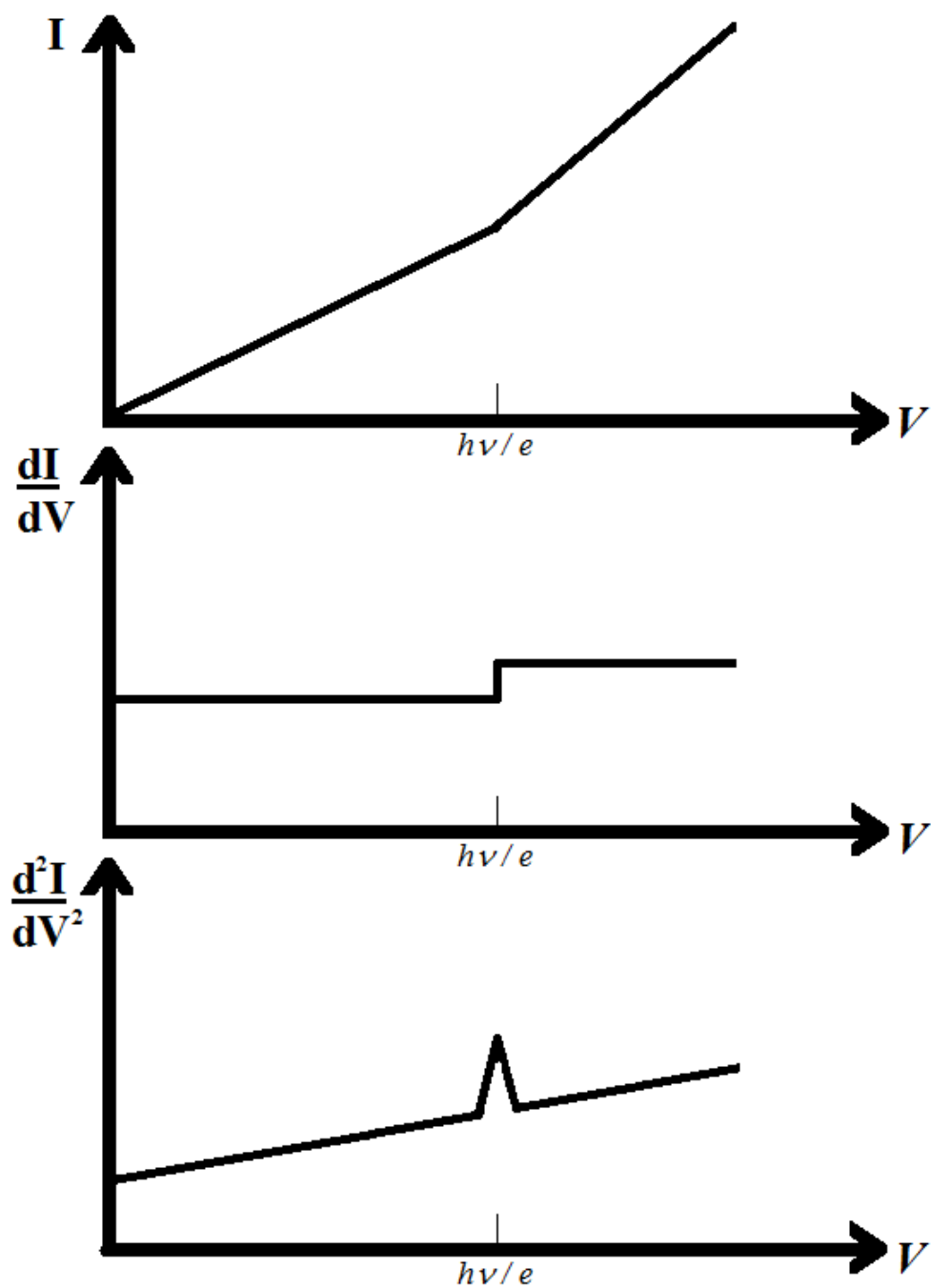


Figure 2.7. Schematic drawing of current vs. voltage, dI/dV , and d^2I/dV^2 . The second derivative corresponds to molecular vibrations in tunnel junctions.

CHAPTER 3 - SURFACE CHARACTERIZATION OF CARBOXYLIC ACID DERIVATIVES ON AMORPHOUS ALUMINUM OXIDE FILMS

3.1 Introduction

The goals of this chapter are to correlate contact angles and XPS to determine relative surface coverage and investigate Pb-SAM interfaces by XPS to determine if interfacial reactions occur. This information is critical in order to gain an understanding on the role of SAMs in molecular tunnel junctions. This chapter will be divided up into multiple sections. In section 3.2, contact angle measurements for all SAMs studied will be presented. In section 3.3, XPS results of benzoic acid derivatives on amorphous aluminum oxide will be shown. Then Pb or Au will be vapor deposited on top of the benzoic acids and the XPS results will be shown in Section 3.4. Section 3.5 will give XPS results for various alkanolic acid derivatives including SAMs with carboxylic acid and phosphonic acid anchoring groups. Finally, section 3.6 will conclude with a summary.

3.2 Contact Angle Measurements of SAMs on AlO_x

Sessile drop water contact angle measurements were used to help establish relative surface coverage of the molecules

selected for study. Aluminum films approximately 40 nm thick were deposited as described in section 2.2.2. These films were then oxidized for 10 minutes to allow a thin layer of AlOx to grow. At 10 minutes, contamination from lab air has been shown to be minimal.⁷⁴ As the oxidation of AlOx occurs, hydroxyl groups chemisorb onto the surface creating a very hydrophilic surface.⁷⁵⁻⁸² Contact angle measurements were made using the procedure described in section 2.3.1. The measured contact angle for a hydroxylated AlOx surface was found to be $13 \pm 1^\circ$. All molecules were chemisorbed to AlOx via the procedures described in sections 2.2.3.1 and 2.2.3.2.

The choice of solvent is critical in the formation of SAMs. To understand which solvent gave the highest coverage of molecules on AlOx surfaces, we varied the solvent (with a 1000 s exposure time) and measured the contact angle. For 4-CN benzoic acid, the contact angles were 20, 22, 27 and 51° as the solvent varied from H₂O, ethanol, acetonitrile, and benzene, respectively. For 4-I benzoic acid, the contact angles were 33, 46, 41, and 60° , respectively. Consequently, it seems polar protic solvents interact with surface hydroxyl groups and inhibit the chemisorption of the benzoic acids. This result is similar to another study in which a group studied the self-assembly of organophosphonic acids. They found that solvents with lower dielectric constants resulted in more dense and

stable SAMs. This was because solvents with high dielectrics coordinate with the surface preventing SAM formation.⁸³ As a consequence of these results, we chose to use benzene as the solvent for the self-assembly process.

Next, we wanted to determine the best method for chemisorbing the SAMs on the surface. We decided to use two techniques to chemisorb the molecules on the surface: self-assembly and spin-coating. A modified spin coating procedure from previous groups was used.⁶⁵ The concentration of solution for spin coating was 10^{-3} M. We directly compared this process to self assembly by making samples with the same bottom Al film (from the same deposition) to negate roughness, temperature, and humidity effects between various days. Then they were exposed to the same 10^{-3} M solution for 10000 seconds. The data is shown in Table 3.1. It is clear that the surface coverage from self-assembly is much higher when compared to the spin-coating process.

Next, we wanted to gain an understanding into the kinetics of the adsorption process for the benzoic acids. We decided to measure the surface coverage of molecules vs. time. Here the contact angle was measured for samples (with an Al film deposited at the same time) exposed to solution for 1, 10, 100, 1000, and 10000 seconds. This experiment was done for halogen

Spin Coating		Self Assembly	
Benzoic Acid	Contact Angle (°)	Benzoic Acid	Contact Angle (°)
4-CN	38	4-CN	51
4-I	65	4-I	75
4-Cl	70	4-Cl	80
4-Br	65	4-Br	77
4-F	62	4-F	70

Table 3.1 Contact angle measurements obtained for spin coating and self assembly of benzoic acids on AlO_x.

substituted benzoic acid derivatives with a solution concentration of 10^{-6} M and the data is shown in Table 3.2. As can be seen, the contact angle increases dramatically at 1 second and slowly increases until it reaches a plateau between 1000 and 10000 s. This is indicative of a Langmuir type isotherm where (at low solution concentration) the rate of adsorption is much greater when surface sites are vacant and once most surface sites are filled, the rate of adsorption becomes less and equilibrates with the rate of desorption. At 10000 s, a saturation surface coverage is reached. Contact angles for many more benzoic acid derivatives were also taken in solutions with concentrations of 10^{-3} M. Table 3.3 shows the results of these experiments. As can be seen, surface coverage is also dependent on the concentration of solution. Even though the coverage is at saturation, the absolute value of the contact angle is dependent upon the size and the polarizability of the para-substituent in contact with the water drop.

The contact angle measurements are consistent with similar monolayers on hydrophilic surfaces studied by others. For example, one group measured a contact angle of 82° for benzenethiol adsorbed to an Au surface.⁸⁴ At saturation coverage, contact angles of 60° and 63° were obtained for 4-Br benzoic acid on GaAs and phenyltrichlorosilane on SiO_2 .^{85,86} Additionally, contact angle measurements of 69° , 67.7° , and 66.9° were

Benzoic Acid	1 s	10 s	100 s	1 000 s	10 000 s	Spin Coating
4-F	59	58	59	68	71	58
4-Cl	60	58	61	71	72	62
4-Br	60	60	62	68	72	59
4-I	59	59	62	68	71	62

Table 3.2 Contact angle measurements for various para-substituted halogenated benzoic acid derivatives. Solution concentration was 10^{-6} M.

Benzoic Acid	Contact Angle (°)
4-SH	51
4-CN	53
2-I	67
4-H	71
2-SH	72
4-F	74
3-I	75
4-Cl	77
4-Br	80
4-I	80

Table 3.3 Contact angle measurements for various benzoic acid derivatives on AlO_x. Each measurement was taken after a 10⁴ s exposure to a 10⁻³ M solution.

obtained for 4-F, 4-Cl, and 4-Br on ITO.⁶⁶ The higher contact angles that we obtained for the benzoic acids suggest that they pack better on AlOx than on ITO and supports Kelvin probe measurements of previous groups.^{26,27}

Additionally, various long alkyl chain SAMs were studied for a comparison to the benzoic acids. Mercaptohexadecanoic and heptadecanoic acids were dissolved in ethanol and the substrates were immersed into 10^{-3} M solution for 10^4 s. The contact angles obtained were 82° and 102° , respectively, suggesting much higher surface coverage for the alkanolic acid SAMs vs. benzoic acids. These contact angles measurements are consistent with results from many others between 97° - 115° , and are indicative of high packing density for alkanolic acid SAMs.^{8-10,23} Finally, we studied octadecylphosphonic acid SAMs that were made using the same conditions as the alkanolic acid samples. We observed contact angles between 110° - 113° for SAMs exposed to solution for 10^4 s and is consistent with other studies in which the measured values ranged from 110° - 117° .^{34,73} This result confirms that coverage is highest with phosphonic acid SAMs due to better packing.

The Cassie equation⁶⁶ was used to estimate the surface coverage of the benzoic acids and compared to densely packed alkanolic acids on AlOx. The Cassie equation is written as:

$$\cos \theta = f_1 \cos \theta_1 + f_2 \cos \theta_2 \quad (3.1)$$

Here, θ is measured contact angle for the benzoic acid monolayer, f_1 is fractional coverage for a saturated monolayer, and f_2 is the fractional coverage $(1-f_1)$ for a bare surface without a monolayer. We used the average contact angle of $\theta = 78^\circ$ for the benzoic acids at saturation coverage, a contact angle of $\theta_1 = 119^\circ$ for a fully packed alkanolic acid monolayer,⁷⁴ and $\theta_2 = 13^\circ$ for a bare AlOx film. We calculate the saturation coverage for benzoic acids on AlOx at $f_1 = 0.53$, or approximately half of one monolayer.

3.3 XPS Study of Benzoic Acid Derivatives

XPS was used to determine binding energies and surface coverage of the benzoic acids chemisorbed to AlOx. Experimental details about the XPS experiments are described in Section 2.3.2. The survey spectra for each benzoic acid derivative are shown in Figures 3.1 and 3.2. The major peaks with binding energies (BE) common to all SAMs and substrates are identified as: O(1s) at 532 eV, C(1s) at 286 eV, Al(2s) at 120 eV, and Al(2p_{3/2}) at 79 eV. Any other peaks present are due to the halogen substituent's photoelectrons. Most importantly, XPS confirms that there is no major contamination present in the SAMs after saturation coverage, except a small amount of Na at ~500 eV. Once the SAMs are chemisorbed onto the surface, they attenuate photoelectrons that come from substrate. This can be

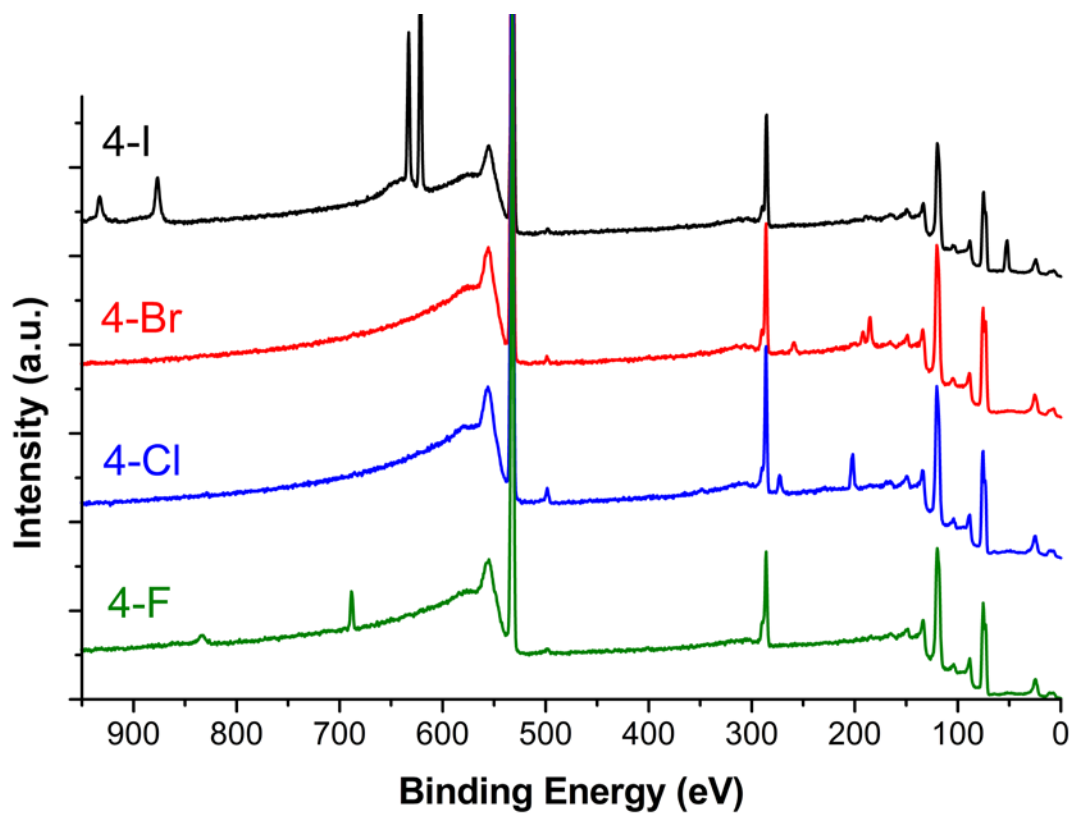


Figure 3.1. Survey spectra of para-substituted halogenated benzoic acid SAMs on AlOx.

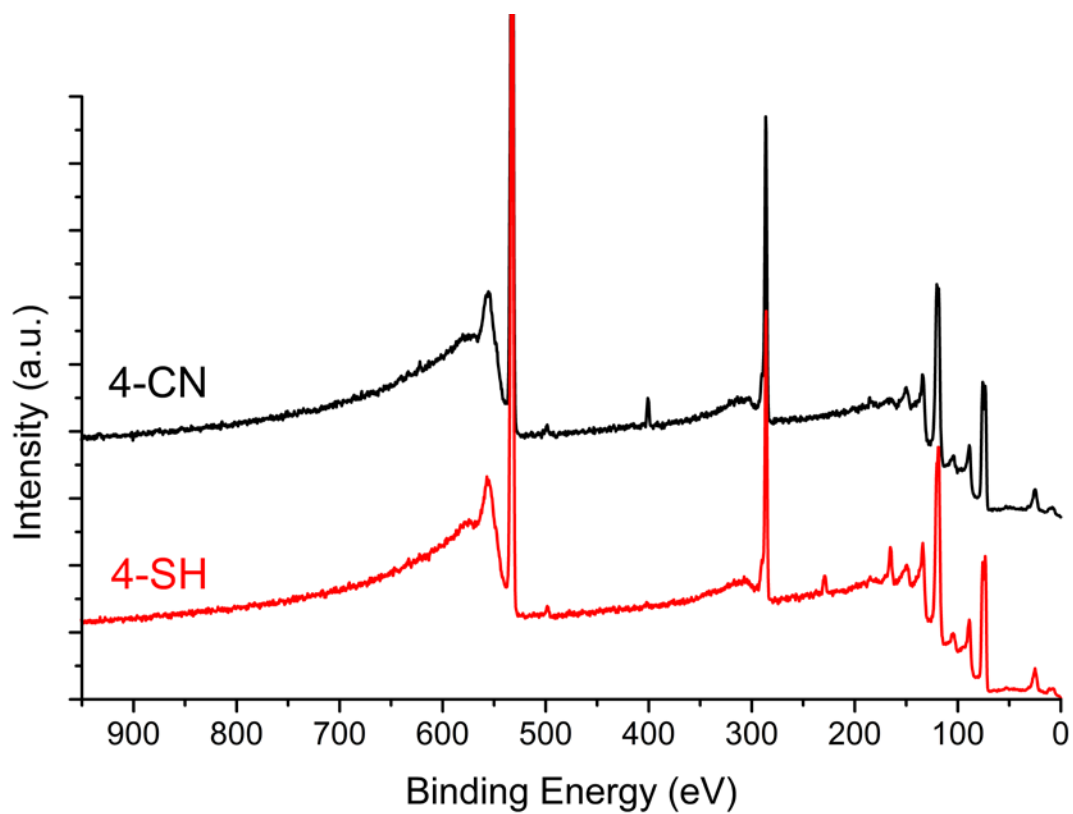


Figure 3.2. Survey spectra for 4-CN and 4-SH benzoic acid on AlO_x substrates.

seen in high-resolution spectra of the Al (2p) region as shown in Figure 3.3. Figure 3.3b shows the Al (2p) for the AlOx film with no SAM and Figure 3.3a shows the same region for an AlOx film with a 4-Cl SAM. The Al (2p) peak at 75.4 eV is due to Al³⁺ and the metallic Al peak is observed at 72.8 eV. Clearly, as the 4-Cl SAM is adsorbed on the AlOx surface, the Al⁰(2p) photoelectrons are attenuated by the SAM. The intensity decreases with respect to the Al³⁺(2p) peaks which are closer to the surface and attenuated less. At saturation coverage the integrated areas for the Al⁰ and Al³⁺ peaks were determined using the Kratos processing software. The ratio (R) of the Al³⁺ to Al⁰ integrated peak areas were used to calculate the thickness of AlOx using the following equation⁸⁸:

$$d = \lambda_{Al} \ln(R + 1) \quad (3.2)$$

Here λ_{Al} is the inelastic mean free path of Al photoelectrons. A value of 32.57 Å was used for the inelastic mean free path of the electrons with a kinetic energy of 1416 eV.⁷⁹ The average thickness of the AlOx was found to be 24 Å. This value is close to AlOx thicknesses found by others at 23 (± 1) Å.⁶⁴

High-resolution spectra were obtained for the various halogen core level regions. Figure 3.4 shows the binding energies for the F(1s) peak at 688.2 eV, the Cl(2p_{3/2}) peak at 201.9 eV, the Br(3p_{3/2}) peak at 185.2 eV, and the I(3d_{5/2}) peak at

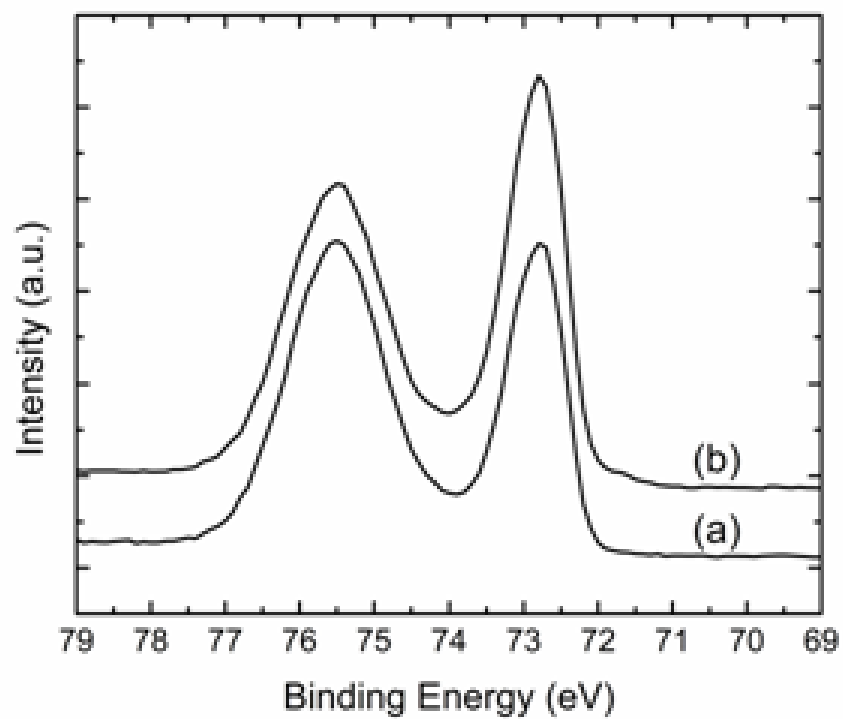


Figure 3.3. High resolution spectra of the Al (2p) region for an Al surface with 4-Cl benzoic acid (a) and for an Al surface with no SAM (b). The peak at 75.4 eV is from the Al^{3+} (2p) and the peak at 72.8 eV is the Al^0 (2p) peak.

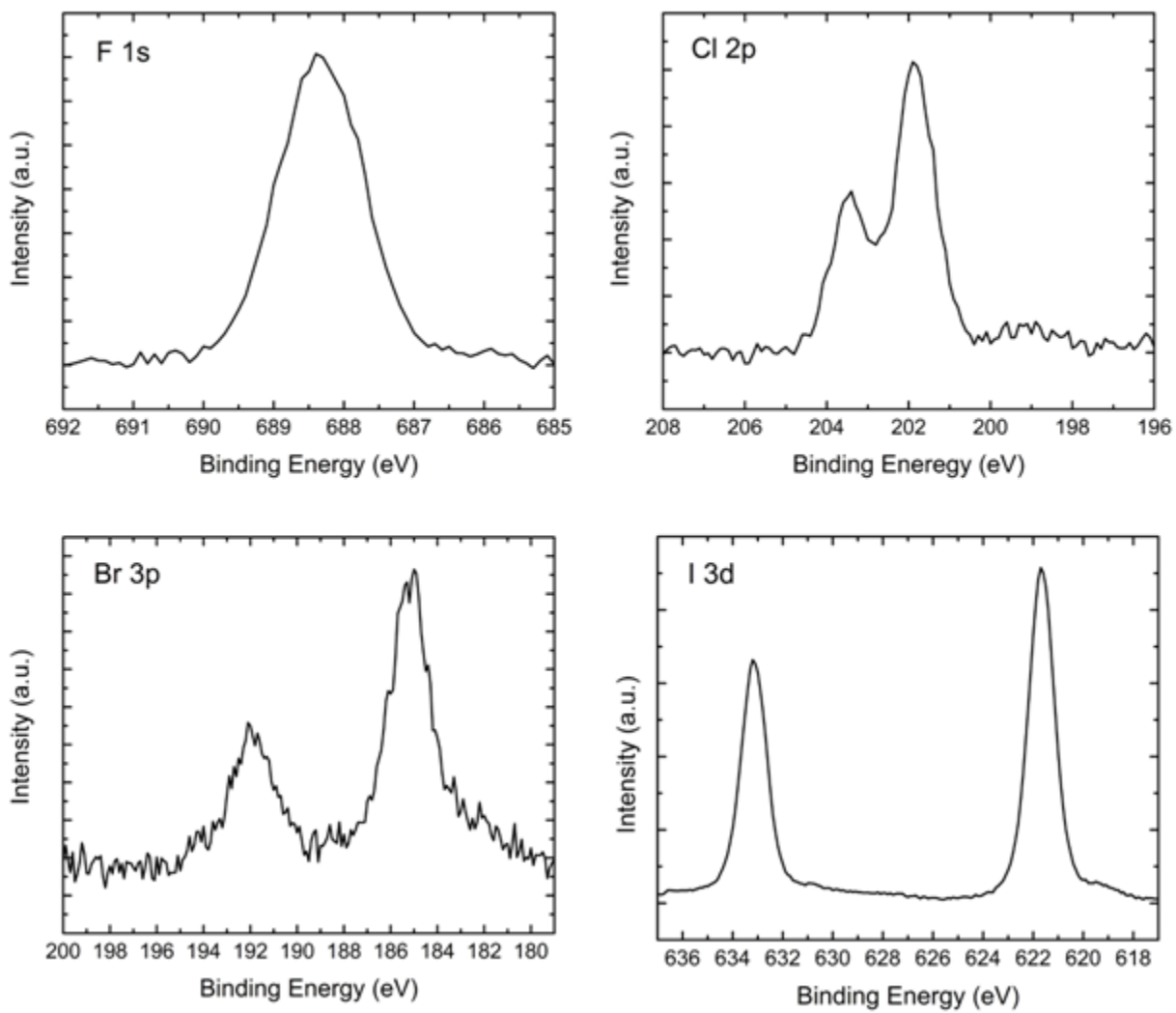


Figure 3.4. High-resolution spectra of halogen regions for halogenated SAMs on AlO_x.

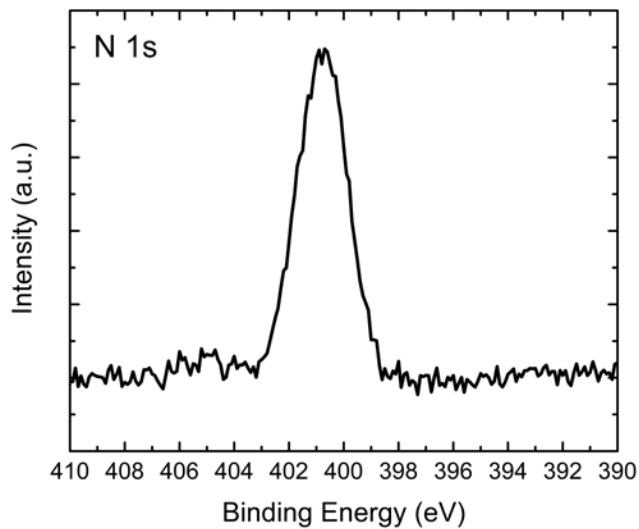
621.7 eV for 4-F, 4-Cl, 4-Br, and 4-I SAMs respectively. All halogen binding energies agree well with previous reports on similar molecules.⁸⁹⁻⁹² High-resolution XPS spectra were also obtained for 4-CN and 4-SH and are shown in Figure 3.5. The N(1s) had a BE of 400.5 eV and the S(2p_{3/2}) had a BE of 165 eV. These values agree well with reported binding energies of 400 eV for N(1s) and 163.3 eV¹ for S(2p_{3/2}) for cyano terminated SAMs on SiO₂ and mercaptohexadecanoic acid chemisorbed to Fe₂O₃, respectively.^{93,94}

The thickness of the halogenated SAMs were calculated using equation 3.2.⁷⁹ The calculated thickness were 6.0 Å, 6.5 Å, 5.6 Å, and 7.1 Å for 4-F, 4-Cl, 4-Br, and 4-I respectively. The 5.6 Å thickness calculated for the 4-Br SAM is low due to the difficulty in deconvoluting the Br(3s) peak that overlaps the Al⁰(2p) peak. This data suggests that the planes of the aromatic rings of the benzoic acid monolayers are perpendicular to the surface. These values agree well with the molecular dimensions determined by x-ray crystallography. Specifically the molecular chain length for 4-F, 4-Cl, 4-Br, and 4-I is 6.2 Å,⁹⁵ 6.6 Å,⁹⁶ 6.8 Å,⁹⁷ and 6.9 Å,⁹⁸ respectively.

Figure 3.6 shows high-resolution C(1s) XPS spectra for the halogenated benzoic acids. The spectra were fit to three peaks: the lowest BE peak is due to the aromatic carbons, the middle BE

¹ Their C-C aliphatic C (1s) BE was 284.6 eV. To get a true comparison add ~1.6 eV to their S (2p) BE.

(a)



(b)

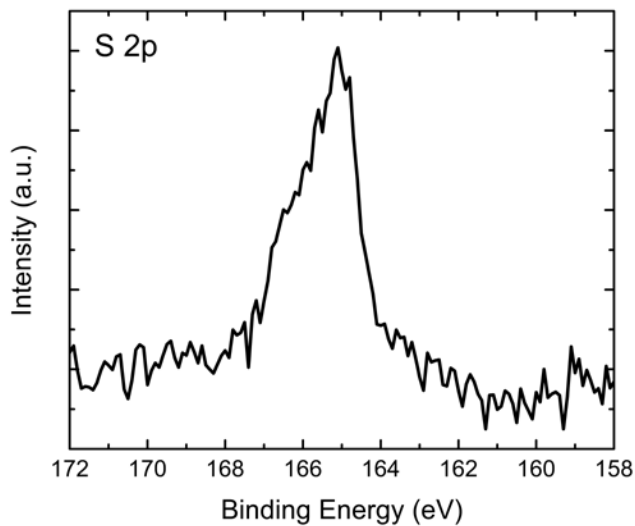


Figure 3.5. High-resolution spectra for the N (1s) region for 4-CN benzoic acid (a) and the S (2p) region for 4-SH benzoic acid (b).

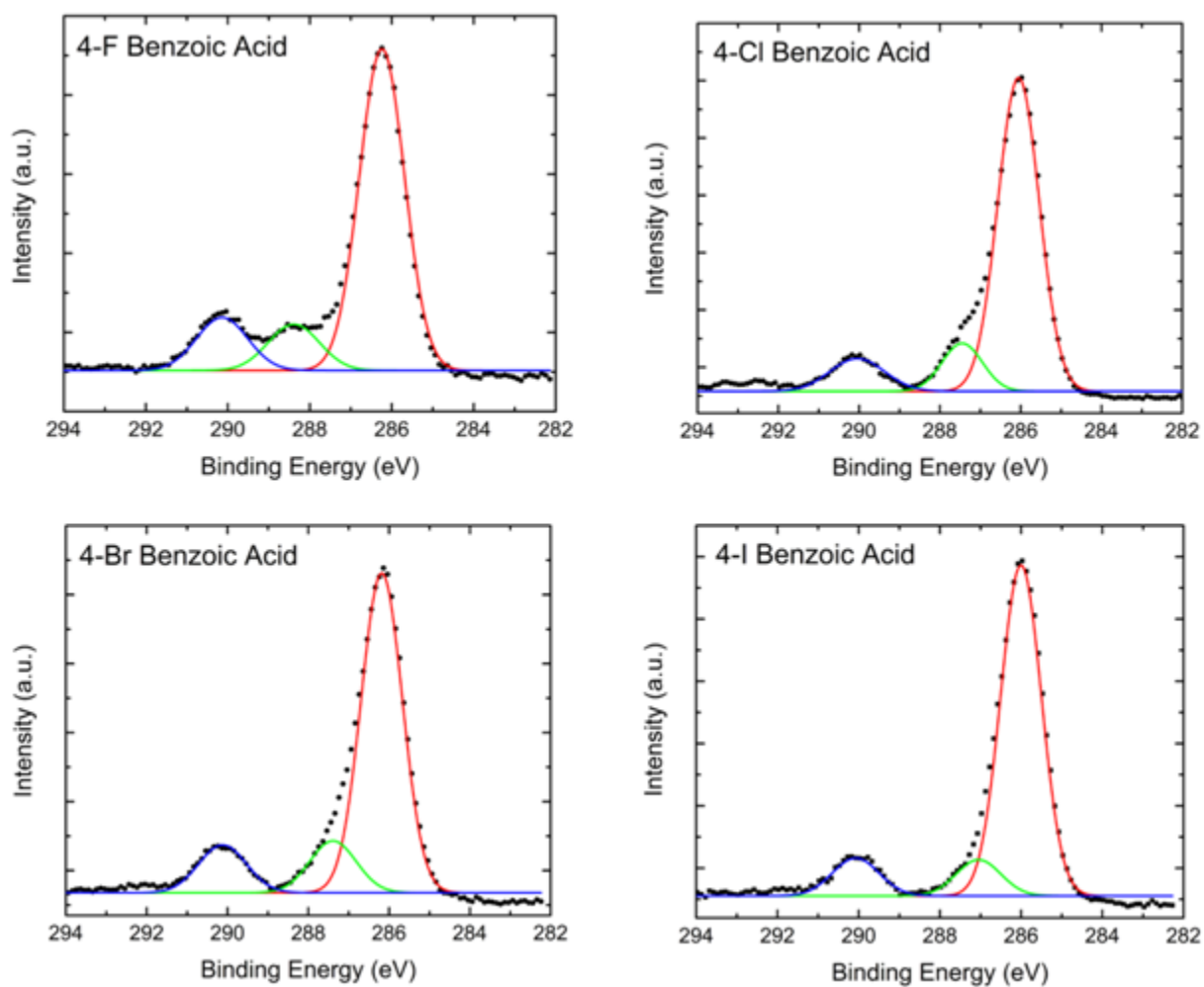


Figure 3.6. High-resolution spectra of the C (1s) region for para-substituted halogenated benzoic acid SAMs. Raw data is shown in black dots. Fit data for the varying C(1s) species are shown as: C-O at highest binding energy, C-X middle binding energy, and C-H at lowest binding energy.

peak is due to the para-carbon, and the highest BE peak is due to the carboxylate carbon. The relative intensities of these peaks were in a 5:1:1 ratio. Table 3.4 summarizes the BEs for the various carbon species present in each SAM. Here the average BE of the carboxylate C(1s) was 290.1 eV and the aromatic C(1s) was 286.1 eV, with a difference (Δ) of 4 eV. Previous XPS studies of carboxylic acids chemisorbed to AlOx agree very well with these values and had a Δ of 4.02 eV for identical carbon species.⁷⁶ The BE of the para-carbon atoms increased with the electronegativity of the halogen atoms, as shown in Table 3.4. The binding energy difference between the para-carbon C(1s) and the aromatic C(1s) peak was 2.15, 1.40, 1.21, and 1.05 eV for 4-F, 4-Cl, 4-Br, and 4-I, respectively. This trend agrees very well with a theoretical prediction that the separation should be 2.2, 1.0, and 0.9 eV for 4-F, 4-Cl, and 4-Br, respectively.⁹⁹ The BE for 4-I was not calculated due to relativistic effects.

To estimate relative coverage of the SAMs the X (X = core level photoelectrons from the halogen substituent) to Al³⁺ (2p) was determined from the integrated peak areas. The values are shown in Table 3.4. Here the ratios were all approximately 0.1. This is significant evidence indicating that, at saturation coverage, the relative coverage between SAMs is approximately the same. In Figure 3.7, a schematic diagram showing the geometry of the benzoic acids chemisorbed to AlOx is shown.

	Normalized Binding Energy Position (eV)			
SAM	C (1s) C-H	C (1s) C-O	C (1s) C-X	X to Al ³⁺ Ratio
4-I	285.7	289.8	286.9	0.099
4-Br	285.9	289.9	287.2	0.093
4-Cl	286.1	290.1	287.5	0.098
4-F	286.1	290.0	288.3	0.097
4-CN	286.3	290.3	287.8	0.101
4-SH	285.6	289.6	286.9	0.094

Table 3.4 Table of XPS C (1s) binding energies for various carbon species and the halogen to Al³⁺ ratio for the various para-substituted benzoic acid SAMs.

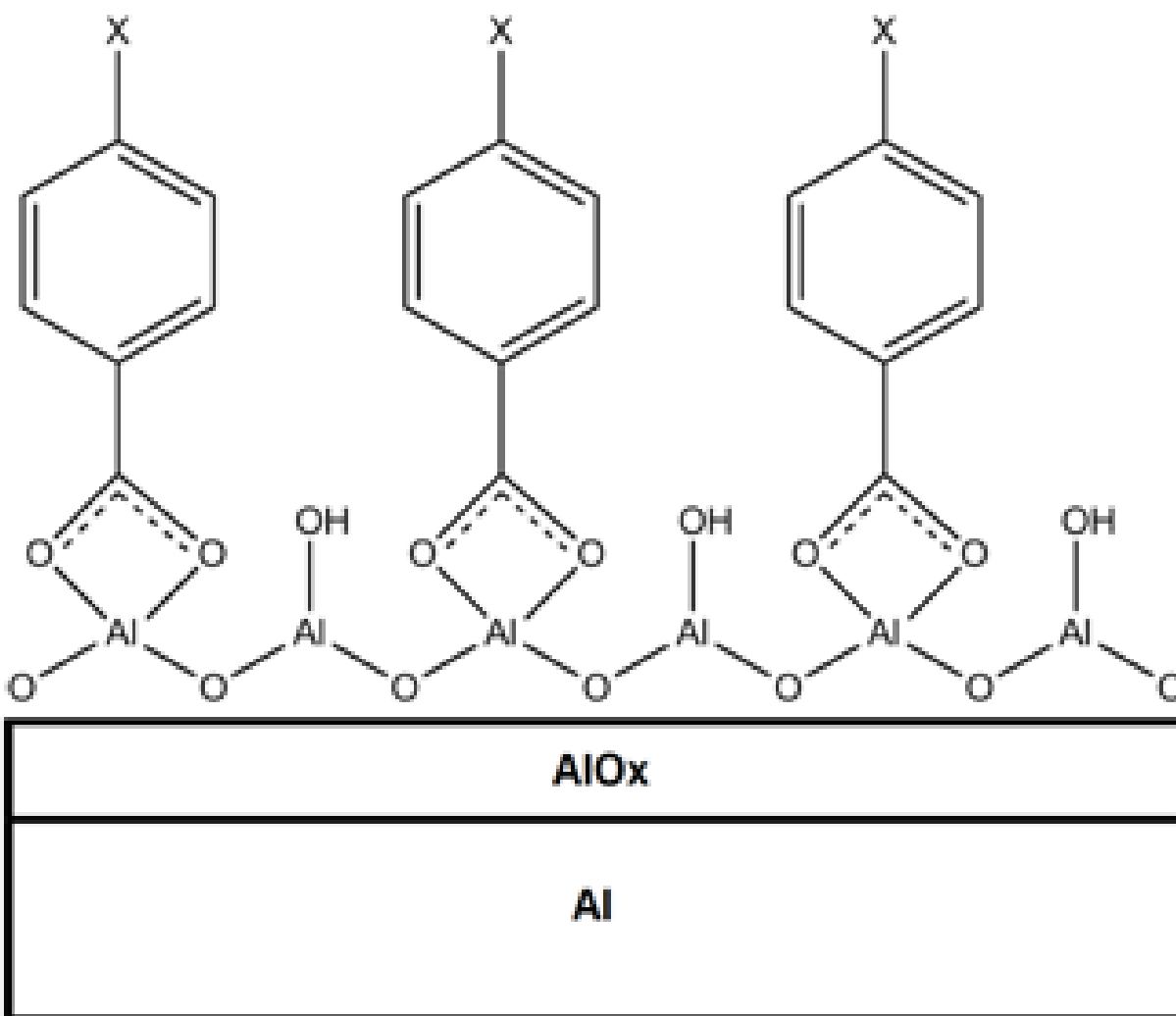


Figure 3.7. Schematic diagram for benzoic acid derivatives chemisorbed to an AlOx surface at saturation coverage.

Using the combination of the contact angle and XPS results, we can estimate the surface coverage of the benzoic acid monolayers. The saturation coverage of hydroxyl groups on an Al_2O_3 (0001) single crystal has been shown to be $5 \times 10^{14} \text{ cm}^{-2}$.³⁰ If this is defined as the saturation monolayer coverage ($\theta = 1$), then using the Cassie equation (Equation 3.1) we calculate a coverage of $2.7 \times 10^{14} \text{ molecules cm}^{-2}$. This is in excellent agreement with a previous study that used neutron activation analysis and determined a coverage of 2.3×10^{14} 4-Br molecules cm^{-2} .¹⁸ These observations suggest there is a one to one ratio of benzoic acid molecules and hydroxyl groups at the saturation coverage, as shown in Figure 3.7.

Section 3.4 XPS of Benzoic Acids with Pb or Au Vapor Deposited

To gain a better picture of the metal-molecule interface, x-ray photoelectron spectra were recorded after Pb was vapor deposited on top of the monolayers. Figure 3.8 shows the Pb(4f) region for 1Å of Pb on the various benzoic acid SAMs. The intensity of the Pb peaks increases as the SAM varies from 4-Br, 4-F, 4-Cl, 4-I, to 2-SH. The much higher intensity for 2-SH indicates that there is a much higher sticking coefficient for Pb on 2-SH SAMs.

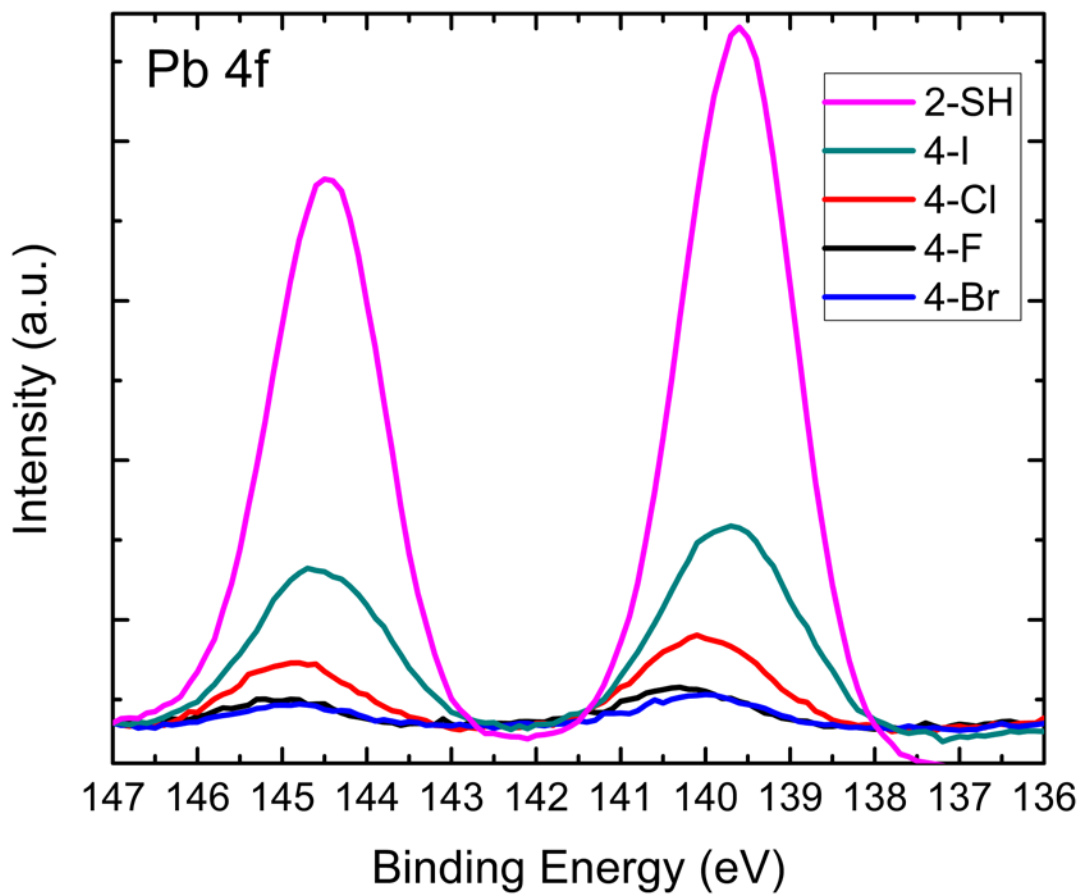


Figure 3.8. High-resolution XPS spectra of Pb(4f) region for SAMs with 1 Å of Pb deposited.

High-resolution spectra of the halogen regions before and after a deposition of 1 Å of Pb and are shown for 4-F, 4-Cl, 4-Br, and 4-I in Figure 3.9. The spectra shown in solid and dashed lines are the halogen regions without and with 1Å of Pb deposited. There are no BE shifts for the halogen peaks after Pb deposition except for a small shift of 0.17 eV to lower BE for 4-I. This shift is not indicative of an iodide-metal bond formation. A chemical reaction between I and Pb is not expected as it is not thermodynamically favorable. The bond energy for C-I is 213 kJ/mol, while Pb-I has a bond energy of 193 kJ/mol.¹⁰⁰

A high-resolution XPS spectrum of the S(2p) region of 4-SH benzoic acid as Pb was deposited from 0 to 4 Å is shown in Figure 3.10. The bottom spectrum is a 4-SH SAM without Pb and the plots above that are 4-SH samples with 1, 2, and 3Å of Pb deposited. The un-reacted sulfur is seen in the main S(2p_{3/2}) peak at 164.8eV. A small amount of the sulfur oxidizes when exposed to air and can be seen in the S(2p_{3/2}) peak with a BE around 168.5 eV. The most significant result is a peak that grows in at 162.7 eV. This peaks is due to the S(2p_{3/2}) photoelectrons from a Pb-S bond and is consistent with another study in which the binding energy for freshly sublimed Pb-S S(2p_{3/2}) was 161.4 eV.¹⁰¹ Numerous other XPS studies have placed the S(2p_{3/2}) binding energy in Pb-S between 161 - 163 eV.¹⁰²⁻¹⁰³ A reaction Pb-S reaction is thermodynamically favorable, as the

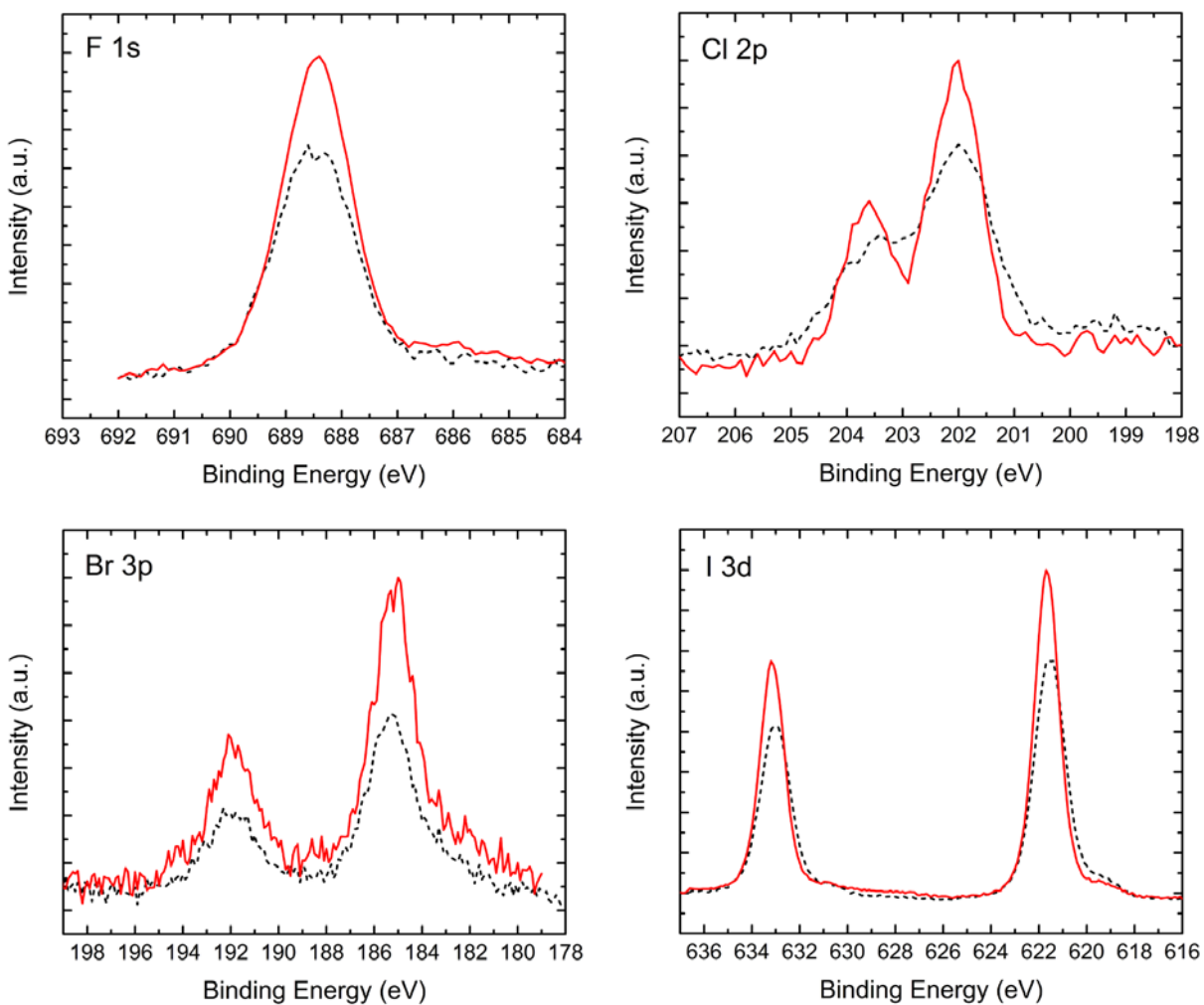


Figure 3.9. High-resolution XPS spectra of various halogen regions of benzoic acid SAMs with (dash) and without (solid) 1 Å of Pb deposited. A pass energy of 80 eV was used for the 4-Cl SAM with 1 Å of Pb. All other spectra were recorded with pass energies set to 40 eV.

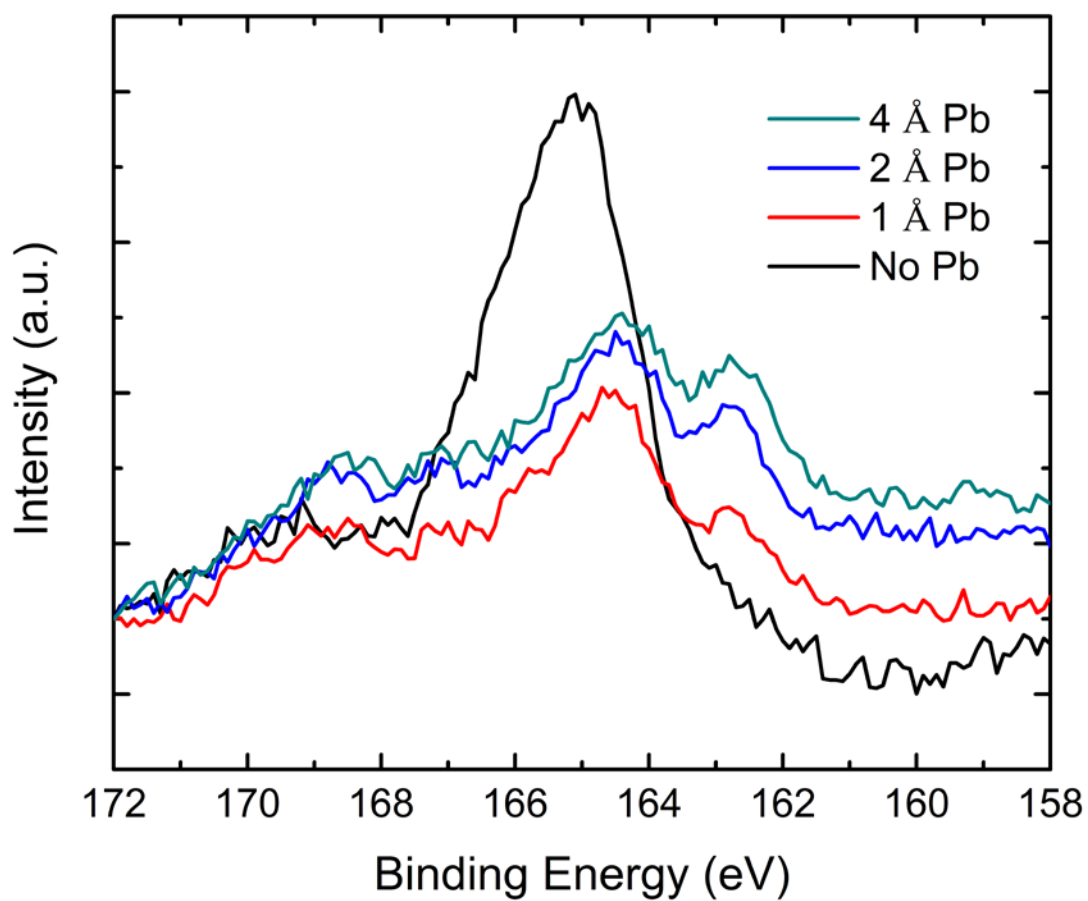


Figure 3.10. High-resolution XPS of the S (2p) region for 4-SH benzoic acid (black) and after Pb deposition: 1Å (red), 2Å (blue), and 3Å (green).

energy required to break the S-H bond is 344 kJ/mol while the energy released from a S-Pb bond formation is 346 kJ/mol.¹⁰⁰ Clearly as Pb is deposited onto the 4-SH monolayer, much of the sulfur reacts to form a Pb-S bond as is clearly shown with a shift to lower BE consistent with increased electron density on the sulfur.

This sulfide bond formation is also evident when Au is deposited on top of 4-SH SAMs. Figure 3.11 shows an XPS spectra of the S (2s) region for 4-SH SAMs without (black) and with 6 Å of Au deposited (red). As can be seen, the BE of the S (2s) without Au is 229.1 eV. After 6 Å of Au is deposited, the BE shifts to 227.9 eV. Again, a lower BE is consistent with a sulfur-Au bond formation.

3.5 XPS of Alkanoic and Phosphonic Acid Derivatives

The final type of SAMs studied were long alkyl (C₁₆₊) chain SAMs: Heptadecanoic, mercaptohexadecanoic, and octadecylphosphonic acids. Survey spectra were obtained and are shown in Figure 3.12. The major peaks are identified as: O(1s) at 532 eV, C(1s) at 286 eV, Al(2s) at 120 eV, and Al(2p_{3/2}) at 79 eV. XPS confirms that there is no contamination present in the SAMs at saturation coverage. High-resolution XPS spectra of the C(1s) regions for the SAMs are shown in Figure 3.13.

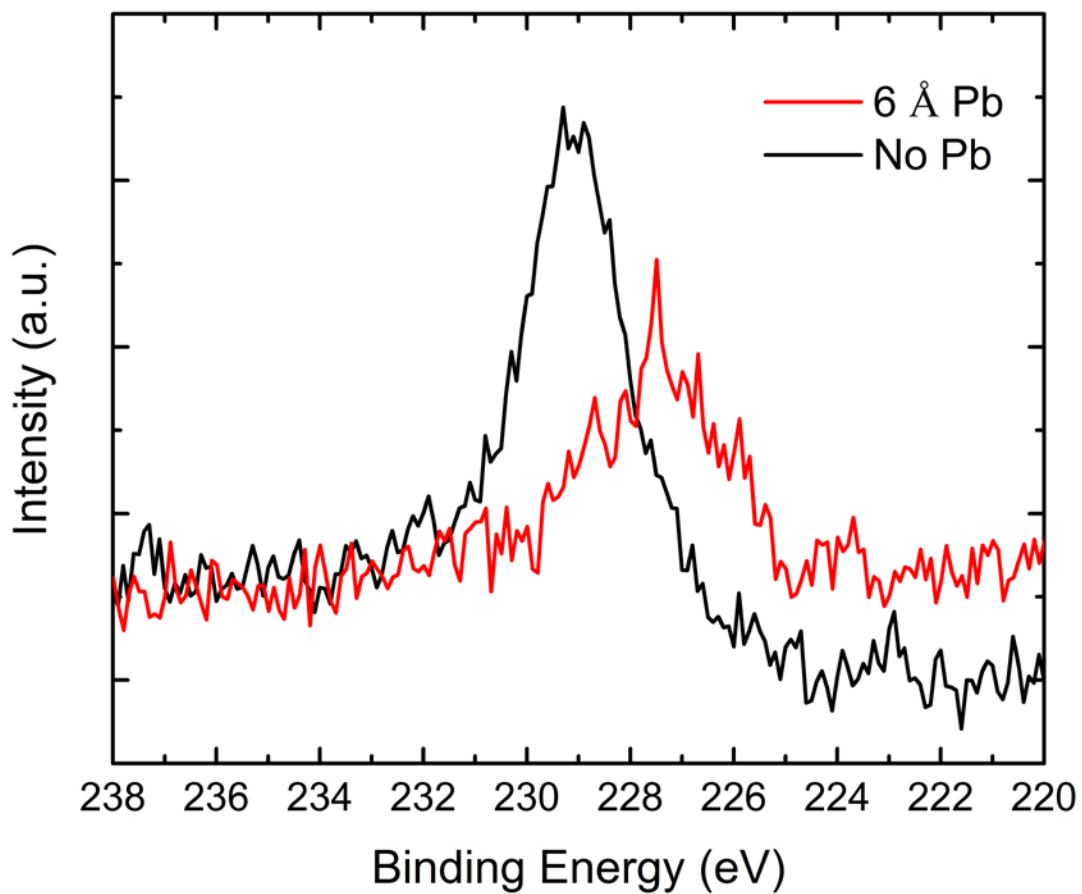


Figure 3.11. XPS of the S(2s) region for 4-SH SAM (black) without and with 6 Å Au (red) vapor deposited.

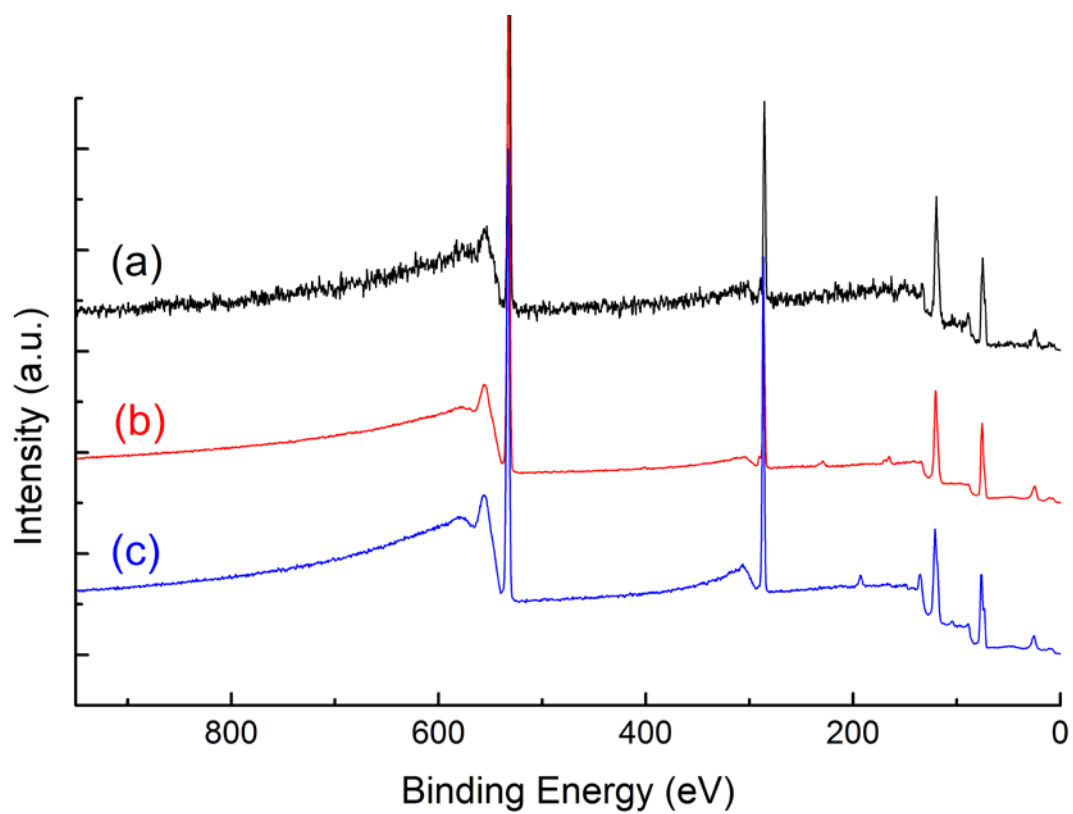


Figure 3.12. Survey spectra of (a) heptadecanoic acid, (b) mercaptohexadecanoic acid, and (c) octadecylphosphonic acid.

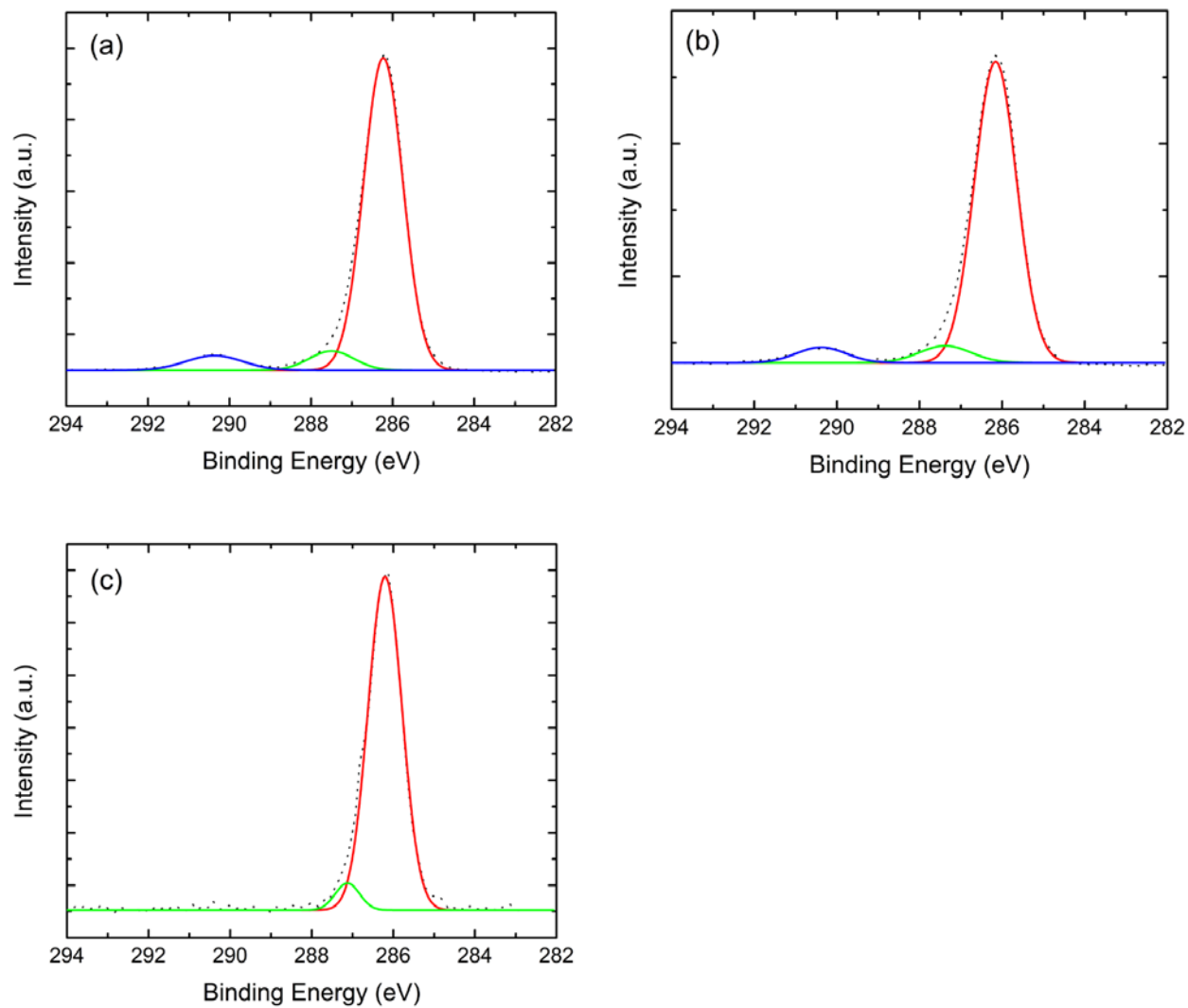


Figure 3.13. High-resolution XPS of the C (1s) region for heptadecanoic acid (a), mercaptohexadecanoic acid (b), and octadecylphosphonic acid (c). Raw data is shown as dots. Fitting for C-H (red), C-O (blue), and C-X (green), where X = (3.13a) C-contamination, (3.13b) C-S, (3.13c) C-P.

High-resolution spectra of the C(1s) region for heptadecanoic acid is shown in Figure 3.13a. The raw data is shown as dots and the C(1s) species that were fit are shown in solid. Heptadecanoic acid has three C(1s) species: C-C, C-contamination, and CO₂⁻. The BE of each were 286.2, 287.5, and 290.4 eV, respectively. The difference in BE between the aliphatic C-C species and the C-contamination or CO₂⁻ C(1s) peaks were 1.3 and 4.2 eV. This agrees very well with another study in which similar Δ's were 1.67 and 4.02 eV for the same carbon species.⁷⁶ The ratio of the integrated area between the C-C C(1s) and the CO₂⁻ C(1s) peak was 15:1 and agrees very well with the theoretical ratio of 16:1.

The XPS spectrum for mercaptohexadecanoic acid (Figure 3.13b) also has three C(1s) species: C-C, C-S, and CO₂⁻. The raw data is shown as dots and the fit is shown as solid lines. The BE of each were 286.2, 287.4, and 290.4 eV. The C-C and CO₂⁻ species are identical to the heptadecanoic acid and agree well with literature reported values.⁷⁶ The Δ in BE between the C-C and C-S was 1.2 eV. This agrees well with a reported Δ of 1.3 eV from a previous study of thiol-terminated monolayers on a silicon surface.¹⁰⁴ The ratio of the integrated area between the C-C C(1s) and the CO₂⁻ C(1s) peak was 15:1 and matches the theoretical ratio of 15:1.

High-resolution XPS for octadecylphosphonic acid was also obtained. The C(1s) region for is shown in Figure 3.13c. The raw data is shown as dots and the C(1s) species that were fit are shown as solid lines. There are two C(1s) species present on the surface. The large peak at a BE of 286.2 eV is due to the C-C carbons. This is similar to a literature report of 286.4 eV for octadecylphosphonic acid on AlOx by another group.³⁶ The smaller peak with a BE of 287.1 eV is attributed to the C-P C(1s) peak. The ratio of the integrated area between the C-C C(1s) and the C-P C(1s) peak was 17:1 and matches the theoretical ratio of 17:1. Finally, a high-resolution spectrum of the P(2p) region is shown in Figure 3.14. The P(2p_{3/2}) region had a BE of 135.1 eV. Another study of octadecylphosphonic acid chemisorbed to AlOx reported a BE for the P(2p_{3/2}) at 134.8 eV.³⁶

3.6 Conclusions

The contact angle and XPS results given in this chapter reveal insight into the adsorption kinetics and adsorption geometry for the benzoic acid derivatives on AlOx substrates, respectively. Benzoic acids chemisorb as a carboxylate with the aromatic plane perpendicular to the surface. Using the water contact angles and XPS results, we determine a saturation surface coverage of 2.7×10^{14} molecules cm⁻². At saturation coverage, the benzoic acids and hydroxyls are present in an

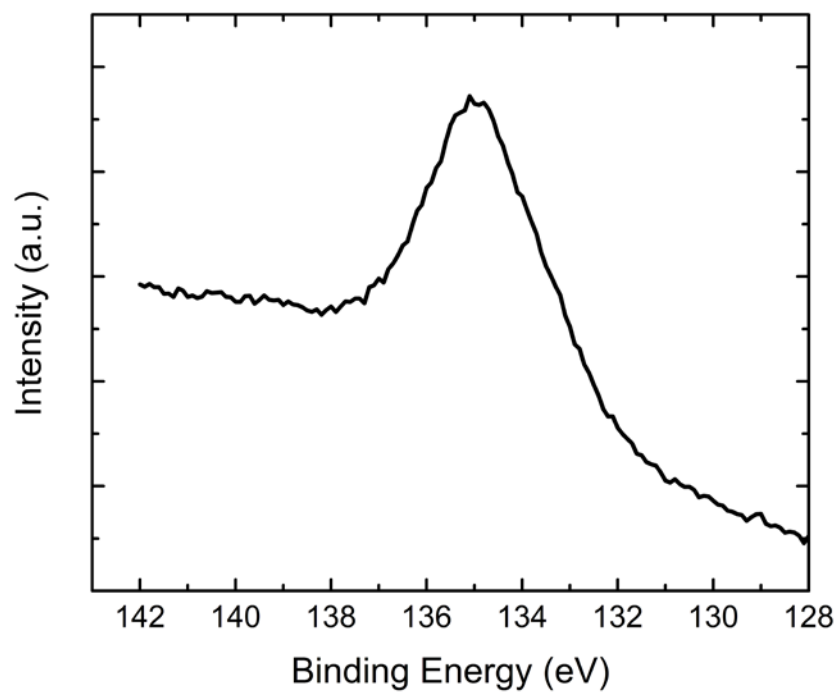


Figure 3.14. High-resolution XPS spectrum for the P (2p) region for octadecylphosphonic acid.

approximate ratio of 1:1. When Pb was vapor deposited on top of the benzoic acid derivatives and XPS measurements were obtained, only 4-SH showed a chemical reaction in the form of S-Pb. Au also showed a complete chemical reaction with 4-SH with a shift in the S(2s) peak 1.2 eV in lower energy indicative of a S-Au bond formation.

Contact angle and XPS results of the long alkyl chain SAM derivatives reveal a higher surface coverage of molecules present on the AlO_x surface when compared to the benzoic acids. The relative ratios between carbon species prove the molecules remain intact with relatively no contamination present.

CHAPTER 4 - TUNNELING SPECTROSCOPY OF BENZOIC ACID DERIVATIVES

Section 4.1 Introduction

This chapter will describe the results of a tunneling spectroscopy study a series of para-substituted benzoic acid monolayers in tunnel junctions with different top metal electrodes. The broad goal of this chapter is to understand how changing the para-substituent affects tunnel conductance. Specifically, we would like to understand how the metal-molecule interface affects the properties of the tunnel barrier. This chapter will be divided into multiple sections. Section 4.2 will describe a basic understanding of aluminum-oxide based tunnel junctions without SAMs and the effects of hydroxyl groups on the barrier properties. Section 4.3 will present and discuss tunneling spectroscopy results from various benzoic acid monolayers with Pb top electrodes. Section 4.4 will present tunneling spectroscopy results for tunnel junctions with para-substituted halogenated benzoic acids and Ag top electrodes. Section 4.5 will present tunneling spectroscopy data obtained with Au top electrodes with 4-I and 4-SH benzoic acid monolayers. Finally, Section 4.6 will conclude with a summary.

Section 4.2 Hydroxylated Aluminum Oxide Surfaces and Tunnel Junctions

Aluminum oxides (AlO_x) as tunnel barriers have been studied for many years.^{18-22,105-106} Giaever won the Nobel Prize in Physics for his study of Al/AlO_x/Pb tunnel junctions.⁴ Since his study in 1960, Al/AlO_x/metal tunnel junctions have been studied extensively over the years and are still studied today.^{4-6,20,106} Aluminum oxide provides a tunnel barrier thin enough for electrons to pass through. Typically, AlO_x tunnel junctions have barrier heights of a few electronvolts (eV).¹⁰⁶

When oxidized, Al forms a self terminating AlO_x layer that can range from 6 to 24 Å in thickness depending on method of oxidation and the thickness of the underlying Al film.^{63,64,106} When an Al film is oxidized in air, hydroxyl groups chemisorb onto the surface.^{75-82,107,108} These hydroxyl groups produce a high energy surface, which is evident in the low contact angles as reported in Chapter 2. In addition many groups have observed vibrational peaks associated with OH stretching and bending modes at 3600 cm^{-1} and 1650 cm^{-1} , respectively.^{22,107-109} When aluminum films are oxidized via an oxygen plasma under vacuum, these hydroxyl groups are not present.¹⁰⁸ Hydroxyl groups chemisorbed to AlO_x are very polar and introduce a strong surface dipole which has a large effect on the work function of AlO_x. Under vacuum using ultraviolet photoelectron spectroscopy

(UPS), the measured work function of an AlOx surface has been reported to be 3.6 eV.¹⁰⁹ Another study calculated that the work function of an AlOx surface to be 3.8 eV.¹¹⁰ After hydroxyl groups were introduced on the surface, the work function of the AlOx increased to 5.35 eV.¹¹⁰ Clearly the polar hydroxyl groups induce a surface dipole increasing the work function of the AlOx.

These polar hydroxyl groups have been shown to have a large effect on electrical measurements (conductance and IETS) of tunnel junctions. Numerous groups have measured the conductance [dI/dV or $G(V)$] of Al/AlOx-OH/Pb junctions. The $G(V)_{\min}$ shifts away from zero bias to 150 mV or greater (when electrons tunnel from the bottom Al electrode to the top Pb electrode).^{6,105} This is because the overall shape of the tunnel barrier is highly asymmetric with the barrier height largest on the AlOx/Pb interface. When an Al bottom electrode is oxidized via plasma oxidation under vacuum, the $G(V)$ curves show no significant asymmetry.¹⁰⁶ Figure 4.1 shows a $G(V)$ spectrum for a representative Al/AlOx/Pb tunnel junction that was oxidized in air and the $G(V)_{\min}$ is observed near $290 \text{ mV} \pm 10 \text{ mV}$. The $G(V)_{\min}$ shift is extremely large when compared to tunnel junctions with SAMs on AlOx, as will be shown later in Section 4.3. Therefore, the shift in the conductance is largely a function of the hydroxyl groups on the aluminum oxide surface.

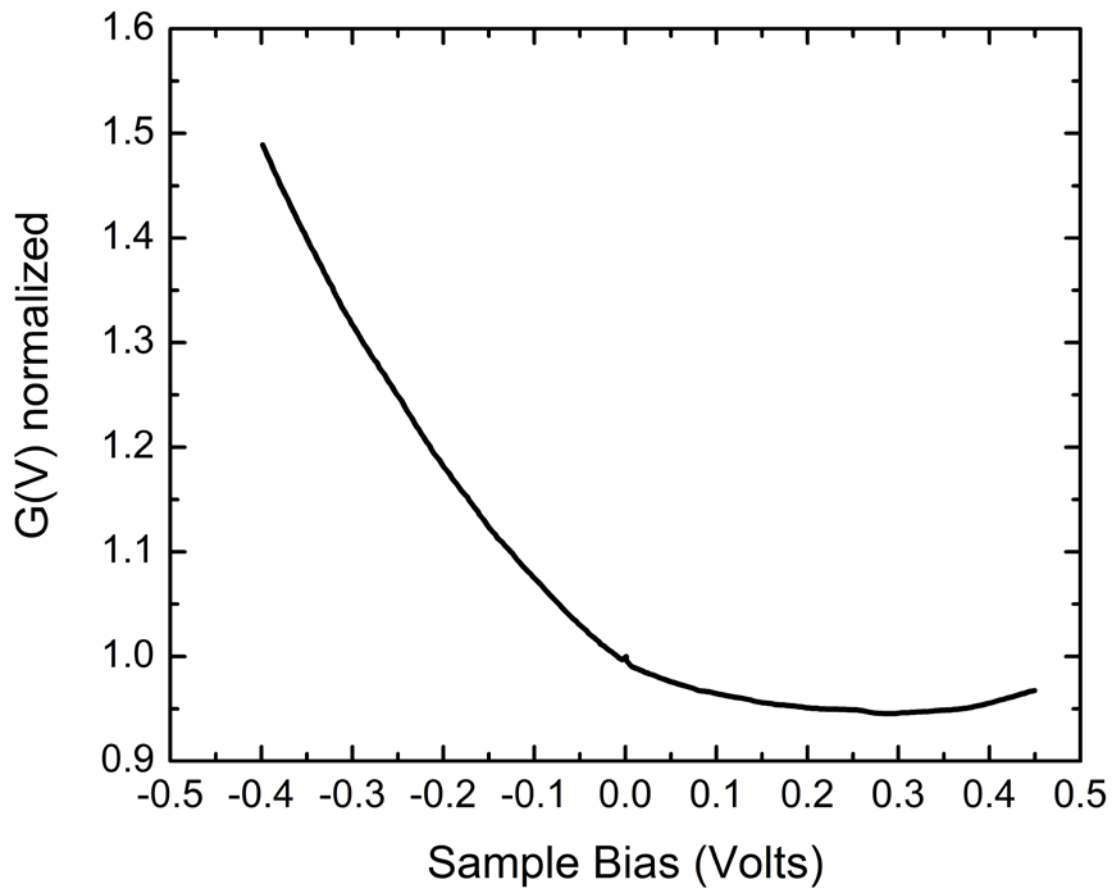


Figure 4.1. $G(V)$ spectrum for a representative air oxidized Al/AlO_x/Pb tunnel junction.

Ag has been shown to be reactive with AlOx. Ag/Al₂O₃ has been studied as a catalyst for oxidation of NO to NO₂ by many groups.¹¹¹⁻¹¹³ In x-ray diffraction (XRD) studies of these films, Ag has been shown to be in both metallic and oxidized forms.^{111,112} Another study used UV-Vis diffuse reflective spectroscopy (DRS) and XPS to show that it forms an ionic bond with Al to form an Ag-O-Al species.¹¹³

4.3 Benzoic Acid SAMs with Pb Top Electrodes

Tunnel junctions were made with benzoic acids as described in Chapter 2. Benzoic acid derivatives have been studied in tunnel junctions in the past in some of the first IETS experiments.¹⁹⁻²² Unfortunately, there were no systematic studies relating the coverage and identity of the para-substituent with the nature of the metal-molecule interface. This section will focus on varying the coverage and identity of para-substituted benzoic acids while using Pb top electrodes to better understand how these properties affect the tunneling conductance.

IETS has previously shown that the halogen para-substituted benzoic acids remain intact after deposition of Ag and Pb top electrodes.¹⁹⁻²² Figure 4.2 shows an IETS spectrum of 4-F benzoic acid that is similar to published results.¹⁹ Table 4.1 summarizes the peak positions and vibrational modes, including a comparison to a previous study. The most intense peaks at 1560 and 3040 cm⁻¹

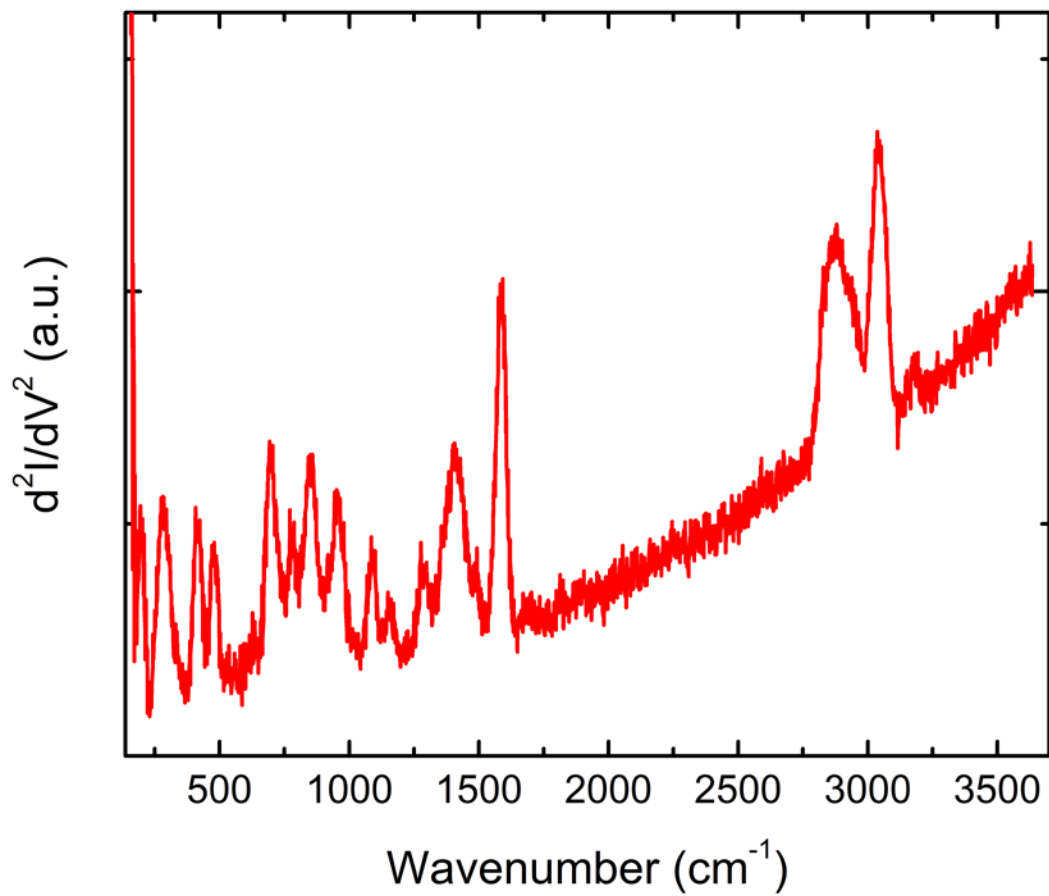


Figure 4.2. IETS of 4-F benzoic acid with Pb top electrodes taken at 4K with a 5 mV ac modulation.

Position (cm ⁻¹)	Vibrational Assignment	Reference (cm ⁻¹)
281	NA	300
414	β(CF)	423
478	α(CCC)	504
697	ν(CF)	698
780	γ(CH)	801
852	γ(CF)	853
953	α(CCC)	994
1090	β(CH)	1072
1155	β(CH)	1161
1287	ν(CC)	1319
1408	SYM CO ₂ ⁻	1437
1491	ν(CC)	1500
1560	ASYM CO ₂ ⁻	1559
1588	ν(CC)	1611
2871	ν(CH)	2880
3040	ν(CH)	3040

Table 4.1 Table of peak positions and their respective vibrational assignments for 4-F benzoic acid. The reference positions are obtained from reference 18.

correspond to the asymmetric CO_2^- and aromatic CH vibrational modes. All other peaks can be assigned to the various vibrational C-C or C-H modes, except for the two vibrational modes of the C-F at 697 and 852 cm^{-1} . Although there is a small shift in the absolute peak positions, there is an overall satisfactory agreement between both studies.¹⁸ This spectrum clearly demonstrates that the benzoic acid SAMs remain completely intact inside the tunnel junctions after the top Pb electrode is deposited.⁶³

Since IETS results have established that the para-substituted halogenated benzoic acid molecules remained undamaged in the tunnel junction, a systematic study was designed to understand the role of surface coverage on tunneling conductance. Figure 4.3 shows $G(V)$ spectra for 4-I samples at different coverages (see below) that were made with the same bottom Al electrode to eliminate any variation in surface roughness or daily environmental conditions. The exposure time was varied from 10 to 10^2 to 10^3 to 10^4 seconds in a 10^{-4} M solution. Clearly there is a systematic change in the overall shape of the $G(V)$ spectra as the exposure time is increased. The $G(V)_{\text{min}}$ shifts from 182 to 146 to 76 to 40 mV for 10, 10^2 , 10^3 , and 10^4 second exposure times, respectively. Figure 4.4 shows how the water contact angle varies with the $G(V)_{\text{min}}$ shift. As the contact angle increases, the $G(V)_{\text{min}}$ shift decreases. Since

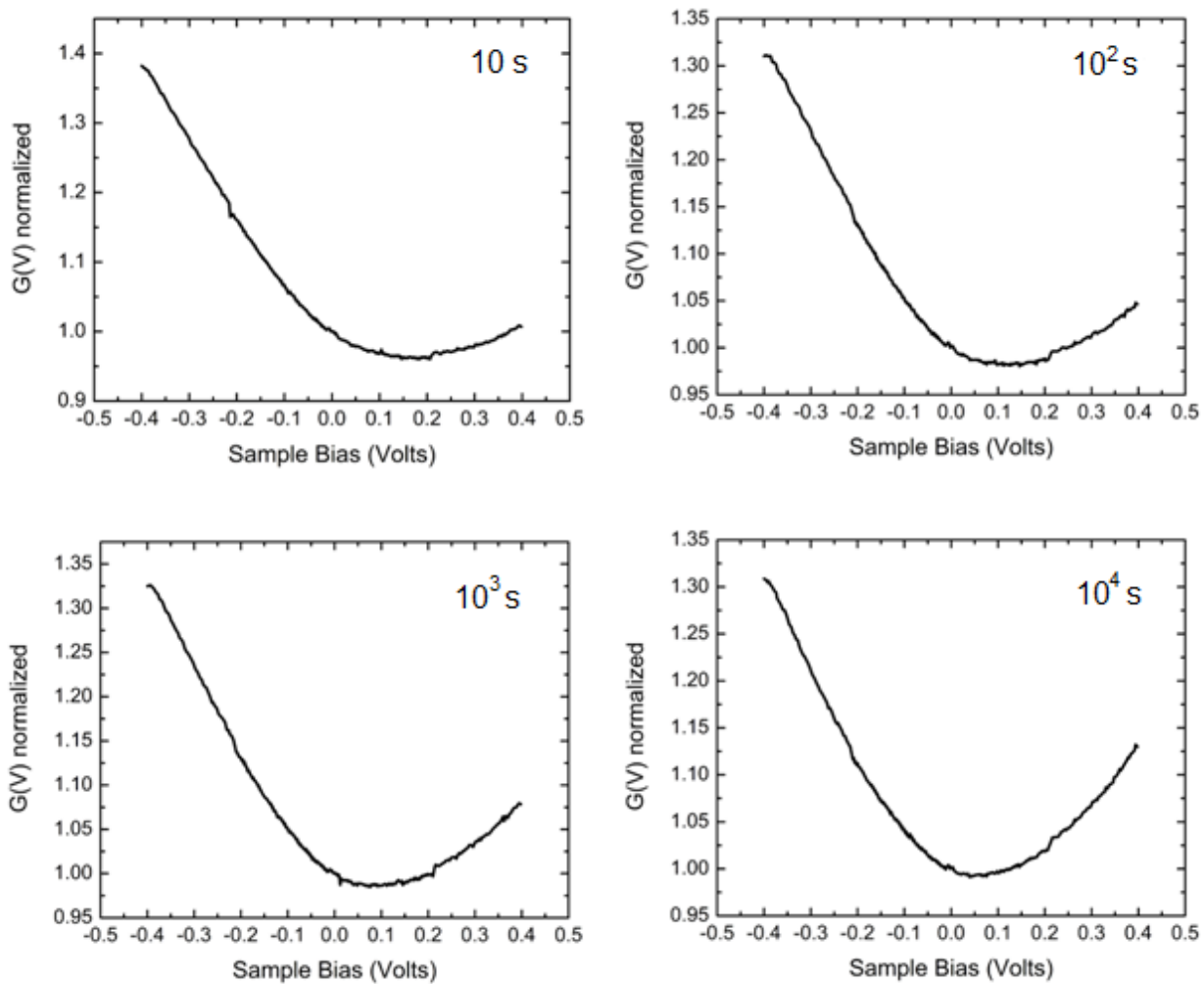


Figure 4.3. $G(V)$ for tunnel junctions containing 4-I SAMs after exposure to a 10^{-4} M 4-I solution for 10, 100, 1,000, and 10,000 seconds.

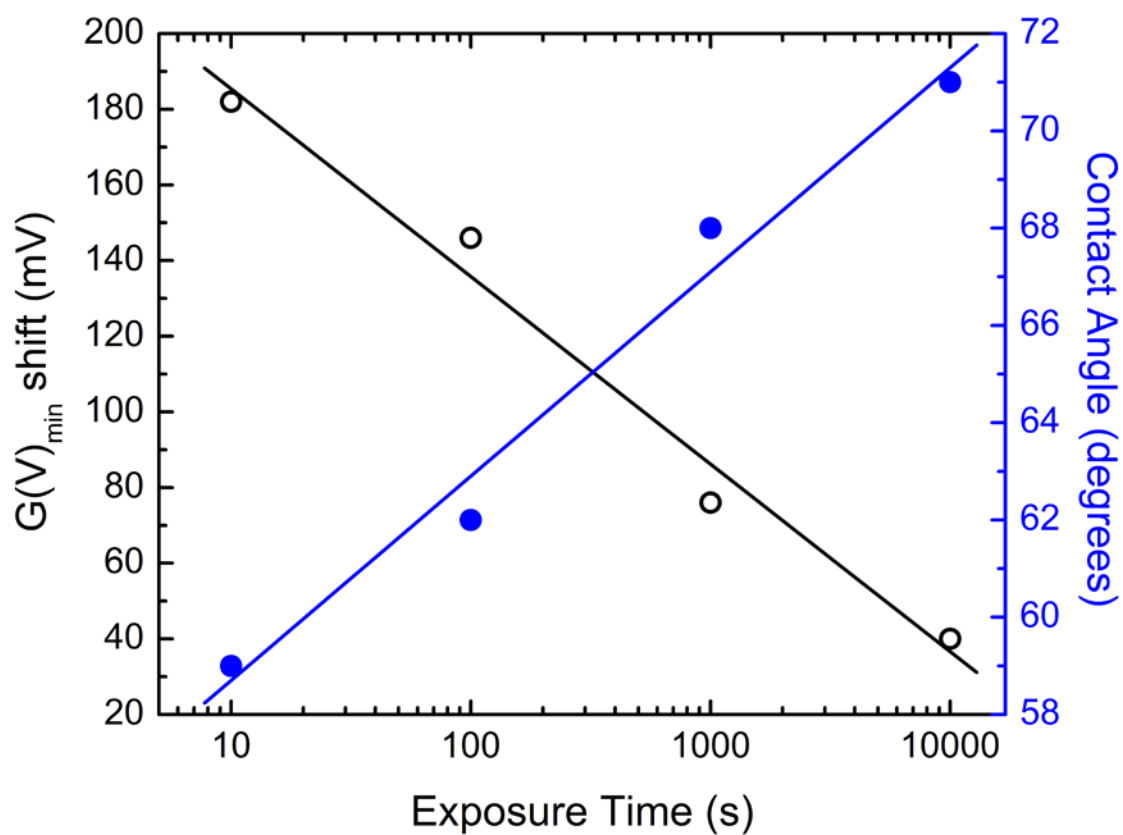


Figure 4.4. $G(V)_{\min}$ shift (open circles) and contact angle (dots) vs. exposure time to a 10^{-4} M solution for 4-I benzoic acid.

contact angle is related to surface coverage, it can be concluded that as the coverage of molecules increases the $G(V)_{\min}$ shift decreases. As a result, fewer Pb atoms are deposited on the polar hydroxyls as the coverage of 4-I increases.

We also wanted to study how the identity of the para-substituent affected the tunneling conductance. Figure 4.5 shows $G(V)$ spectra for tunnel junctions with various halogenated benzoic acids. Again, the same Al electrode was deposited to minimize variation in the tunneling spectra due to environmental conditions and Al surface roughness. Each AlO_x film was exposed to a 10^{-3} M solution for 10^4 seconds to obtain a saturation coverage before a Pb top electrode was vapor deposited to complete the junction. Again, there is a systematic change in the shape of the $G(V)$ curves as the para-substituent is varied from F to Cl to Br to I. Figure 4.6 shows the relationship between the $G(V)_{\min}$ shift and the van der Waals radius of the halogen atom. The van der Waals radii of F, Cl, Br, and I are 1.47, 1.75, 1.83, and 1.98 Å, respectively.¹¹⁴ The $G(V)_{\min}$ shifts for F, Cl, Br, and I SAMs were 120, 75, 40, and 20 mV, respectively. So as the size of the para-halogen increases, the $G(V)_{\min}$ shift decreases. It appears less Pb can penetrate through the 4-I SAM and adsorb on the polar hydroxyl groups. Figure 4.7 shows a schematic diagram of Pb penetration through 4-F and 4-I SAMs. We previously established that at saturation coverage,

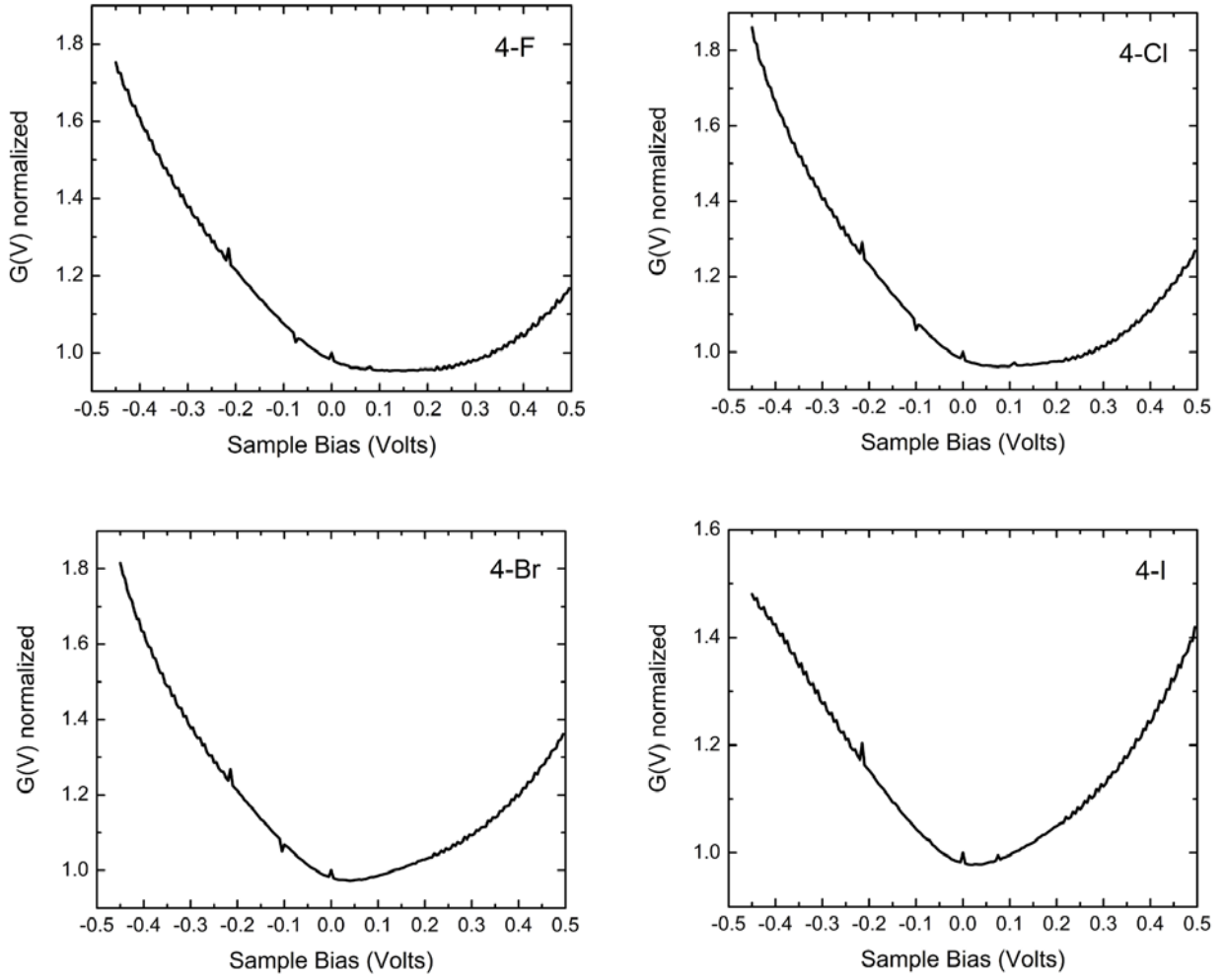


Figure 4.5. $G(V)$ for 4-F, 4-Cl, 4-Br, and 4-I respectively.

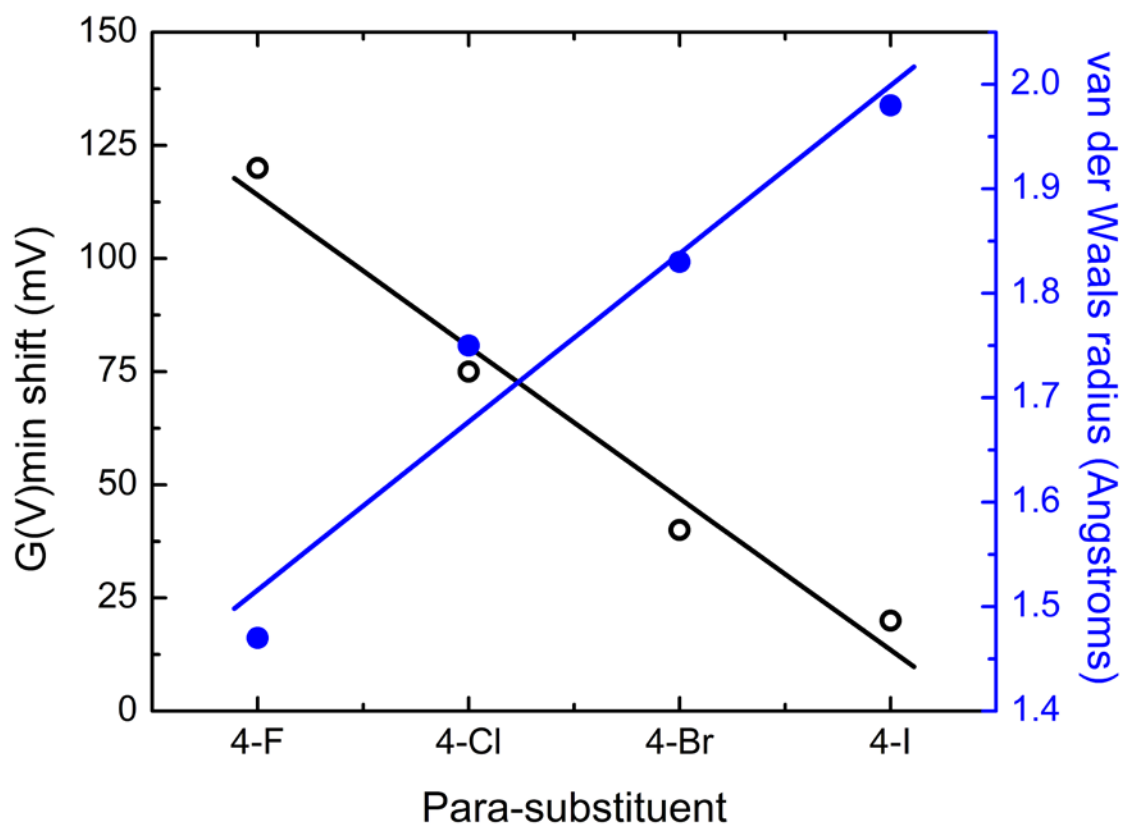
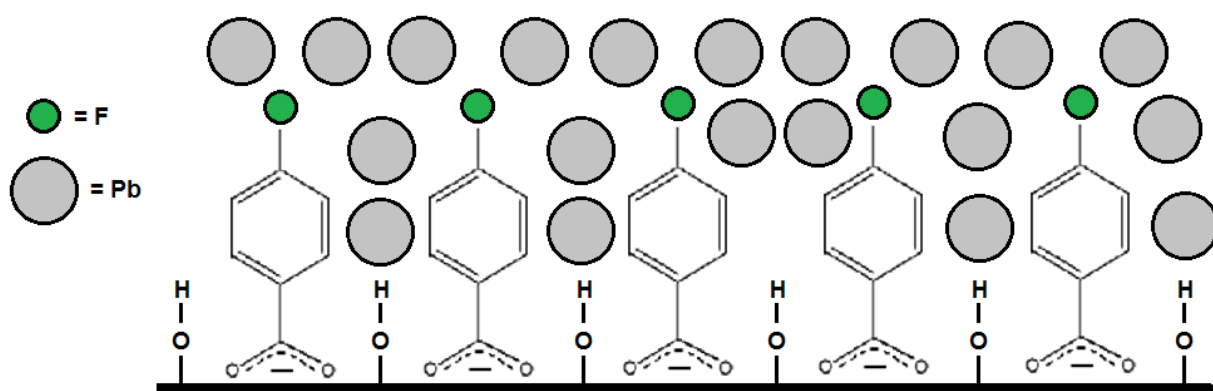


Figure 4.6. $G(V)_{\min}$ shift (open circles) and van der Waals radius (dots) for the various halogenated benzoic acid derivatives with Pb top electrodes.

(a)



(b)

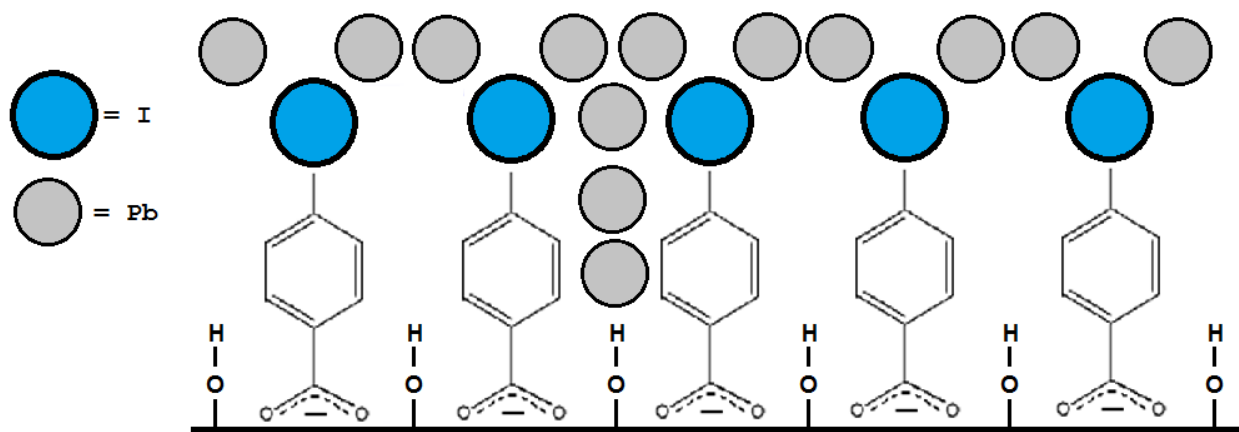


Figure 4.7. Schematic diagram of Pb penetration after vapor deposition for 4-F (a) and 4-I (b) SAMs. Much of the Pb penetrates through a 4-F SAM and adsorbs on the polar hydroxyl groups while very little Pb penetrates the 4-I SAM.

there is a one to one relationship between benzoic acid molecules and hydroxyl groups⁶³ and the schematic shows that relationship. The larger iodine provided a steric barrier to incident Pb atoms and blocks penetration to the hydroxyl groups. Since more Pb atoms adsorb on hydroxyl groups when 4-F is used, the $G(V)_{\min}$ shift is much larger because the barrier height is dominated by the asymmetry at the interface.

Other para-substituents were also studied, specifically cyano and mercapto functional groups. Tunnel junctions were made with a 10^4 second exposure of 4-CN to an AlOx film. As described in Chapter 3, at 10^4 seconds the 4-CN reaches saturation coverage. Figure 4.8 shows a $G(V)$ spectrum for 4-CN with a Pb top electrode. Here the $G(V)_{\min}$ shift is only 5 mV. Clearly the shift is the smallest from zero because the CN group is larger than I atom, providing further evidence that the size of the para-substituent determines the amount of penetration into the SAM. The result also suggests that the electronegativity of the para-substituent is not responsible for the $G(V)_{\min}$ shift from zero because the 4-CN SAM would have the largest offset from zero bias. Therefore, the extent of Pb penetration is likely the source of the $G(V)_{\min}$ shift.

The final benzoic acid derivative that was studied was 4-SH. As described in Chapter 3, after a 10^4 second exposure of an

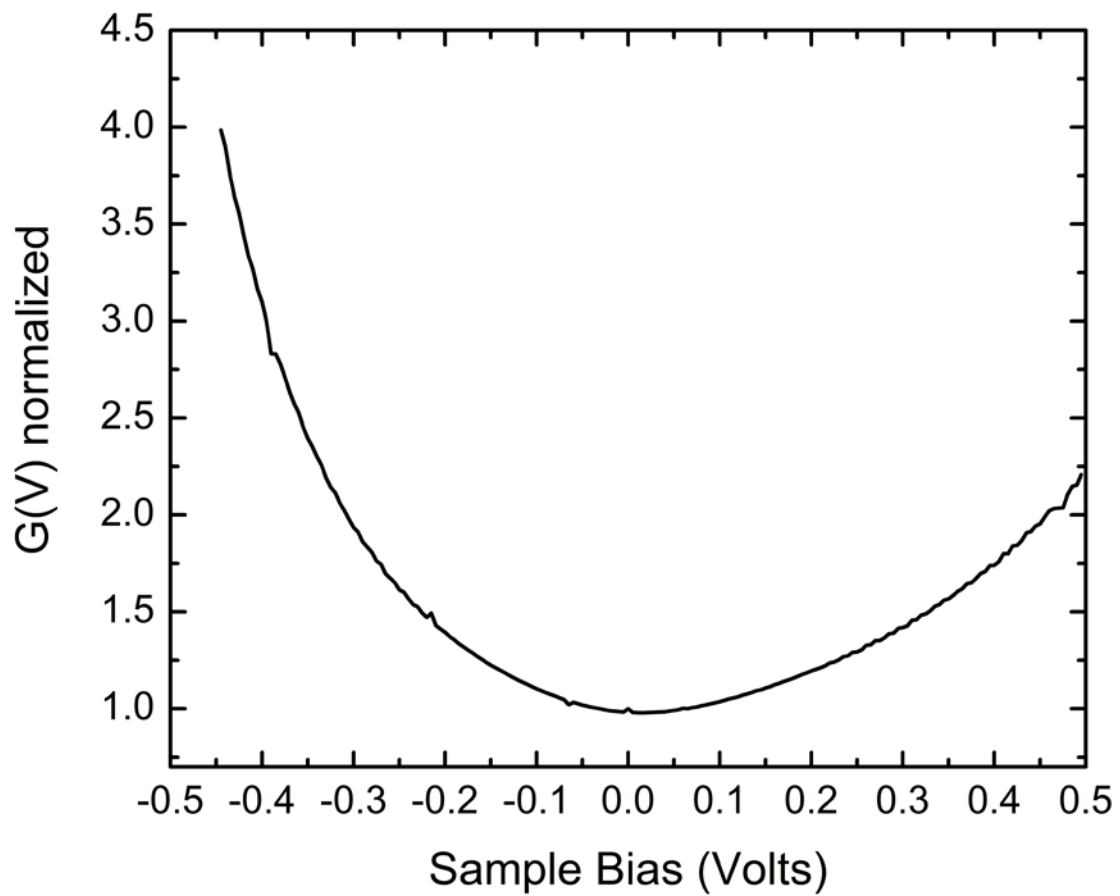


Figure 4.8. G(V) for 4-CN benzoic acid with Pb top electrodes.

AlOx film the 4-SH benzoic acid SAMs result in a saturation coverage. Figure 4.9 shows a representative $G(V)$ spectrum for a tunnel junction with 4-SH at saturation coverage with a Pb top electrode. Interestingly, the $G(V)_{\min}$ shift is toward negative bias at -15 mV. Of all the molecules studied, the 4-SH benzoic acid SAM was the only example to show a negative shift in the $G(V)_{\min}$. This negative shift means that there is a complete reversal in the barrier height at the molecule-Pb interface. In fact, in the Brinkman model the reversal means the barrier height at the 4-SH/Pb interface is smaller than the Al-AlOx interface.⁶

To further understand the origin of the reversal in the barrier asymmetry, IETS measurements were obtained for tunnel junctions containing 4-SH with Pb top electrodes. The ac modulation was set to 10 mV to obtain the highest peak intensities while sacrificing some signal resolution. The results are shown in Figure 4.10. We compared these results to those reported by Monjushiro *et al.* for tunnel junctions containing 2-SH benzoic acid and Pb top electrodes. In the later case the thiol substituent is facing toward the surface and not in contact with the top Pb atoms. Table 4.2 summarizes IETS assignments and a comparison with the Monjushiro *et al.* study.¹¹⁵ Comparing the two studies, many things become apparent. First, there are two peaks missing in the 4-SH spectrum that are

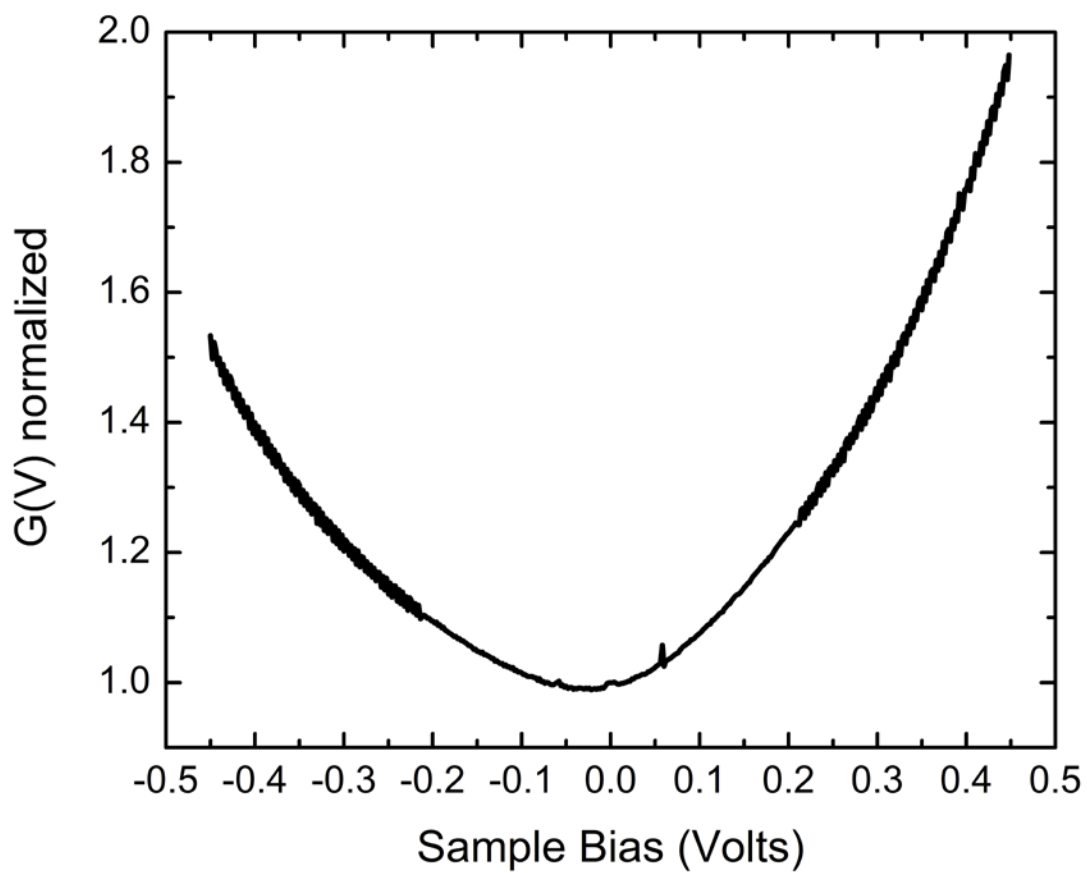


Figure 4.9. $G(V)$ for 4-SH benzoic acid with Pb top electrodes.

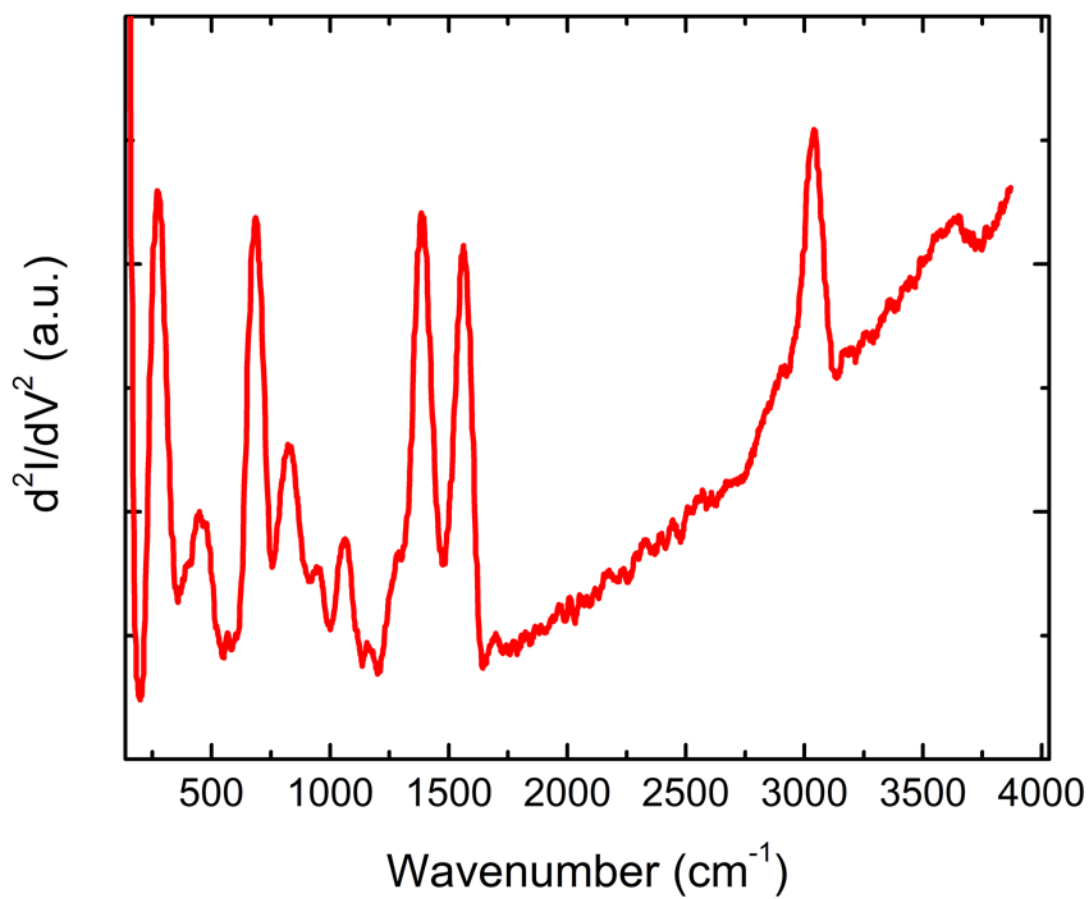


Figure 4.10. IETS of 4-SH with Pb top electrodes taken at 3K with a 10 mV ac modulation.

Position (cm ⁻¹)	Vibrational Assignment	Reference (cm ⁻¹)
264	NA	238
385	NA	364
447	Φ(CC)	494
681	Φ(CC)	695
824	γ(COO)	812
946	γ(CH)	961
1058	β(CH)	1041
1160	β(CH)	1159
1282	Kekule	1287
1385	v _s (COO)	1400
1561	v _a (COO)	1560
Absent	v(SH)	2540
2905	v(CH)	3009
3039	v(CH)	3038
3642	H ₂ O	3620

Table 4.2 Table of peak positions and their respective vibrational assignments for 4-SH. The reference positions are obtained from reference 115.

present in the 2-SH, one at 911 cm^{-1} and another more intense peak at 2540 cm^{-1} . These peaks were assigned to be the $\delta(\text{CSH})$ and the $\nu(\text{SH})$ vibrational modes.¹¹⁵ Second, the peak at $\sim 264\text{ cm}^{-1}$ for 4-SH is much more intense than the same peak with 2-SH. In another IETS study with gold electrodes and a benzenedithiol SAM, the peak intensity of a peak at $\sim 280\text{ cm}^{-1}$ corresponding to $\nu(\text{S-Au})$ varied in intensity depending on slight changes in the orientation of the molecule chemisorbed to the Au electrode.¹¹⁶ In Raman spectroscopy studies, a vibrational mode associated with a S-Pb bond has been observed at $\sim 272\text{ cm}^{-1}$.^{117,118} Taken together, the IETS and the XPS results (from Chapter 3 Section 3.3.1) indicate S-Pb bond formation. Many factors can cause this complete reversal in the barrier asymmetry when S-Pb react. These include lower contact resistance at the S-Pb interface, little or no Pb chemisorbed to the AlOx, and the tunneling transmission probability increasing (with decreasing distance for electron tunneling) due to the S-Pb bond formation.

Figure 4.11 shows a schematic diagram of the three possibilities seen in the study of para-substituted benzoic acid SAMs with Pb electrodes. In Figure 4.11a the tunnel barrier is highly asymmetric with the barrier height of the hydroxyl-Pb interface much higher than the Al-AlOx interface, because of

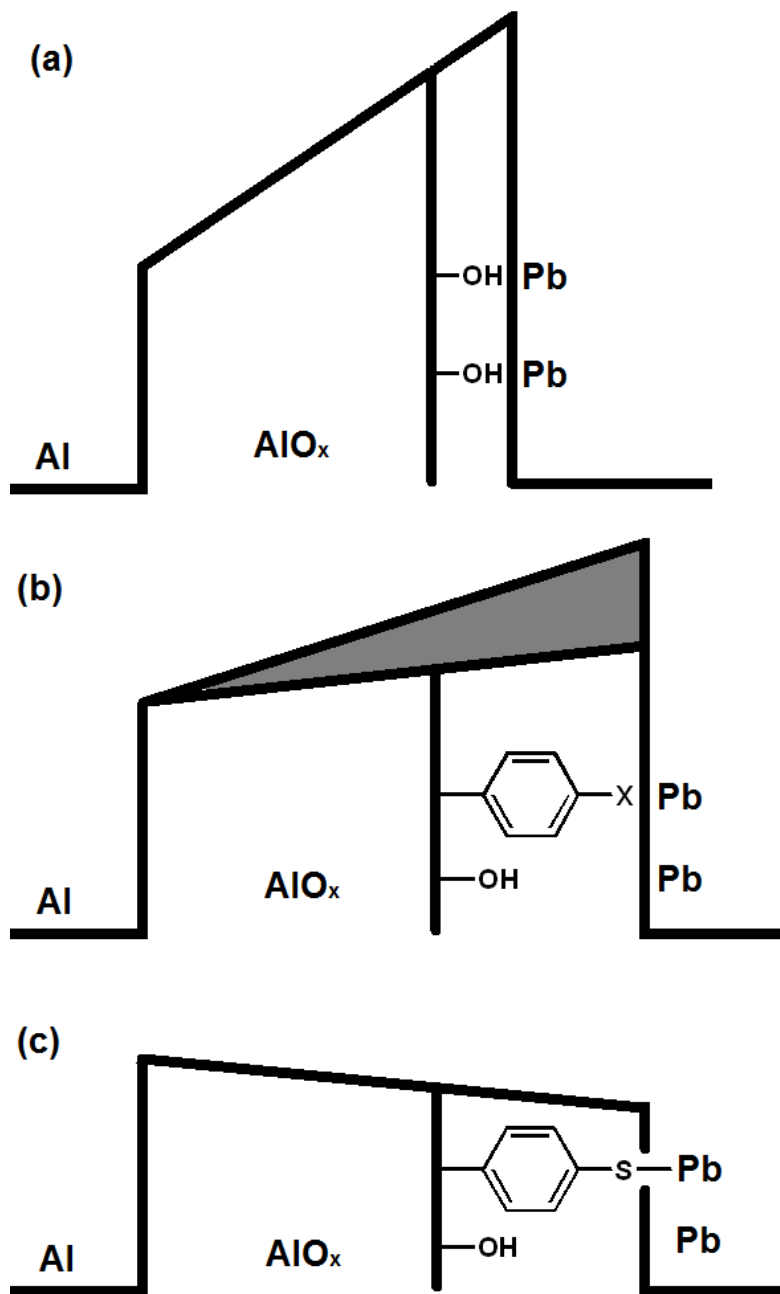


Figure 4.11. Schematic diagram of overall barrier shape for tunnel junctions with: no SAM (a), halogen-substituted benzoic acid SAMs (b), and 4-SH benzoic acid (c). The barrier asymmetry for (b) varies depending on how much of the Pb penetrates through the SAM and adsorbs on the polar hydroxyl groups.

polar hydroxyl groups. In Figure 4.11b, the tunnel barrier shape has the same asymmetry but much less in magnitude. This asymmetry depends on the size of the para-substituent. Larger para-halogens have much less barrier asymmetry because less Pb penetrates the SAM and adsorbs on hydroxyl groups. Whereas smaller para-halogens allow more Pb penetration to the hydroxyl groups leading to the increased the barrier asymmetry. The final case is shown in Figure 4.11c. Here the para-substituent (S-H) bonds with Pb top atoms and completely reverses the barrier asymmetry, since the barrier height of the S-Pb interface is lower than the Al-AlO_x interface (because all contact resistance is lost when the S-Pb bond is formed).

Section 4.4 Benzoic Acids with Ag top electrodes

Tunnel junctions containing benzoic acid derivatives were also made with Ag top electrodes as described in Section 4.3. Previous IETS studies have shown that when Ag is used as the top electrodes, the molecules also remain intact and not degraded.²² A systematic study was made to determine the para-substituent's effect on the tunneling spectroscopy and tunnel barrier properties. Hundreds of junctions were made containing benzoic acids with Ag top electrodes. Approximately 40% of the junctions were non-shortened while 60% of the junctions shorted, which is much lower than Pb with a rate of approximately 70% of non-

shorted junctions. This is not a surprise; since the melting point of Ag at 1235 K is much higher than Pb at 601 K.¹¹⁴ Thus Ag has more kinetic energy when it hits the surface of the monolayer and can penetrate through the SAM to the AlOx. Figure 4.12 shows representative $G(V)$ spectra for the various halogen-substituted benzoic acids. As it can be seen, all $G(V)$ curves are very symmetric. The $G(V)_{\min}$ offsets are all near zero bias, indicating very little asymmetry in the tunnel barrier. This is in contrast to the results from Section 4.3 in which the size of the para-substituent determined the asymmetry of the tunnel barrier. SAMs made from 4-CN were also used with Ag, to determine if a larger para-substituent could inhibit penetration of the Ag to the AlOx. The results are shown in Figure 4.13. The $G(V)$ spectrum appears similar to the halogen-substituted tunnel junctions shown in Figure 4.12. Clearly, using a larger cyano para-substituent does not block Ag penetration to the AlOx surface.

Since the tunnel junctions with Ag showed minimal shift from zero bias, the results were fit to the BDR model to extract the barrier height, width, and asymmetry.⁶ The results are shown in Table 4.3. There is little variation in the asymmetry and the barrier heights were all close to 1 eV with the widths near 20 Å. Altogether, these results are further evidence that Ag completely penetrates the SAMs and adsorbs directly on top of

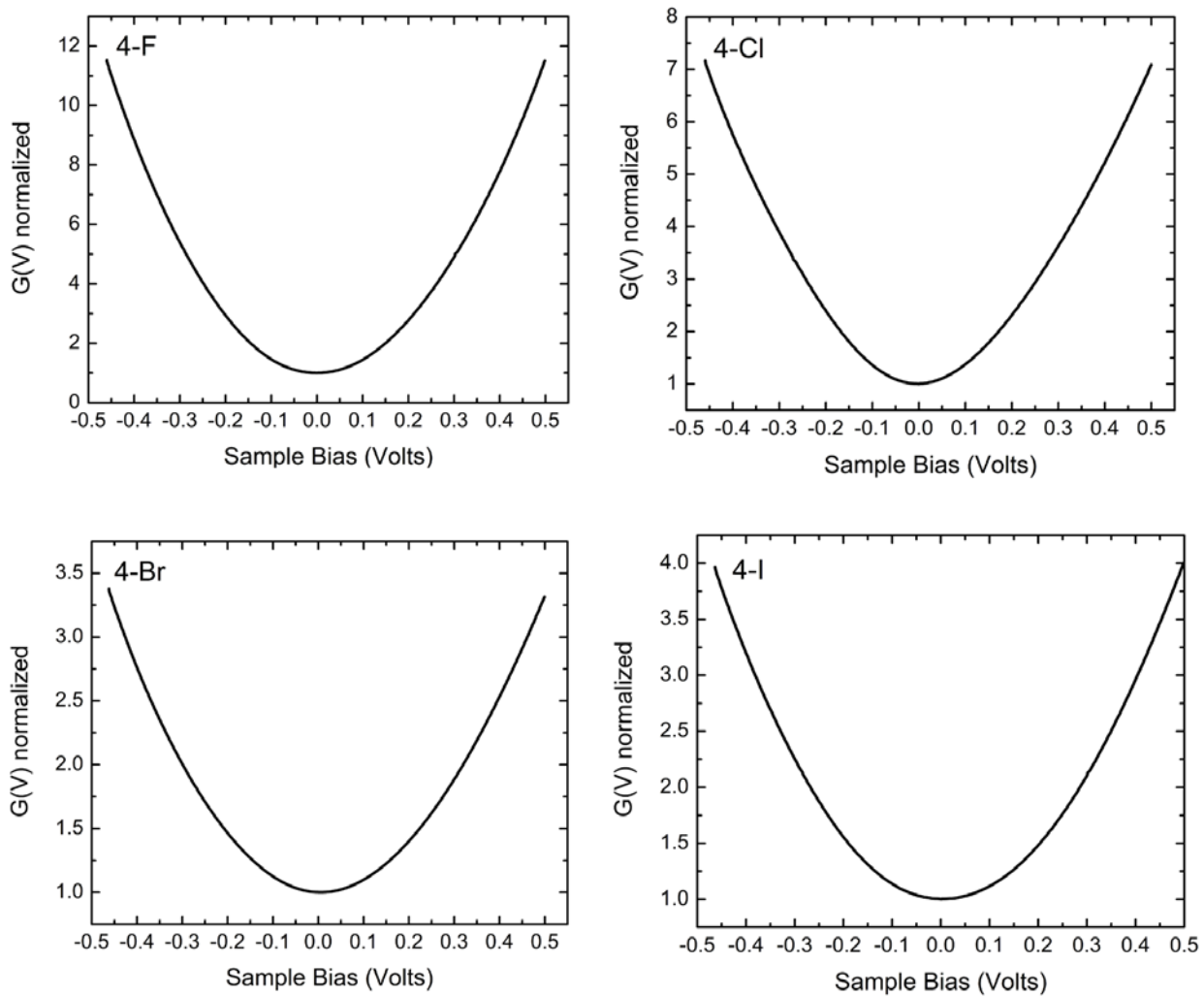


Figure 4.12. $G(V)$ for 4-F, 4-Cl, 4-Br, and 4-I with Ag top electrodes. All have $G(V)_{\min}$ near zero bias.

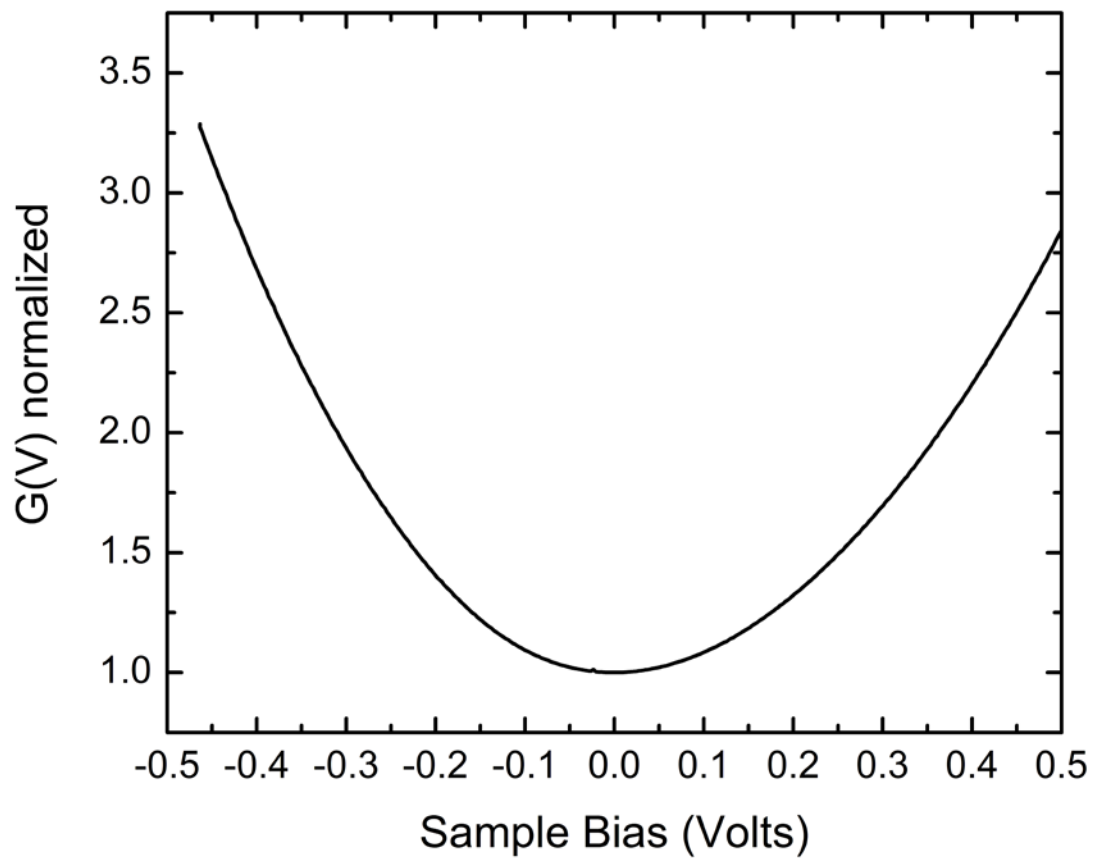


Figure 4.13. $G(V)$ for 4-CN benzoic acid with Ag top electrodes.

<u>SAM</u>	d (Å)	ϕ (eV)	$\Delta\phi$ (eV)
4-F	23.0	0.9	-0.05
4-Cl	20.0	1.2	-0.10
4-Br	18.4	1.3	0.18
4-I	20.8	1.0	0.14
4-CN	19.5	1.2	0.08

Table 4.3 Summary of the values obtained from the Brinkman model for tunneling through benzoic acid SAMs.

the AlO_x surface regardless of the identity SAM present in the monolayer. The barrier asymmetry due to the hydroxyl groups is not present when Ag is used. This is likely due to a chemical reaction between Ag and the hydroxyl groups. Evidence supporting this was revealed by a group performing an XPS study of Ag (111) films.¹¹⁹ They exposed the Ag to NaOH and found it reacted with the hydroxyl groups to form Ag₂O.¹¹⁹

Section 4.5 Benzoic Acids with Au top electrodes

Tunnel junctions containing benzoic acid derivatives were also made with Au top electrodes in a similar fashion as those tunnel junctions made in Section 4.4. Gold has been used as the bottom electrode in numerous tunneling studies with various alkanethiol based SAMs and has been shown to form a gold-thiolate bond.⁴⁷⁻⁵⁰ The yield of nonshorted junctions Au was similar to Ag with a rate of only approximately 33%. Again, this is not surprising as Au has a high melting point at 1337 K and thus higher kinetic energy than Pb.¹¹⁴

A study of the effect of coverage on the tunneling properties of 4-I SAMs and Au top electrodes was conducted. Aluminum oxide films were exposed to a 10⁻⁴ M solution containing 4-I for 10, 100, and 1000 seconds. Au was then vapor deposited and G(V) measurements were obtained. The results are shown in Figure 4.14. The G(V)_{min} shifts closer to zero bias as the

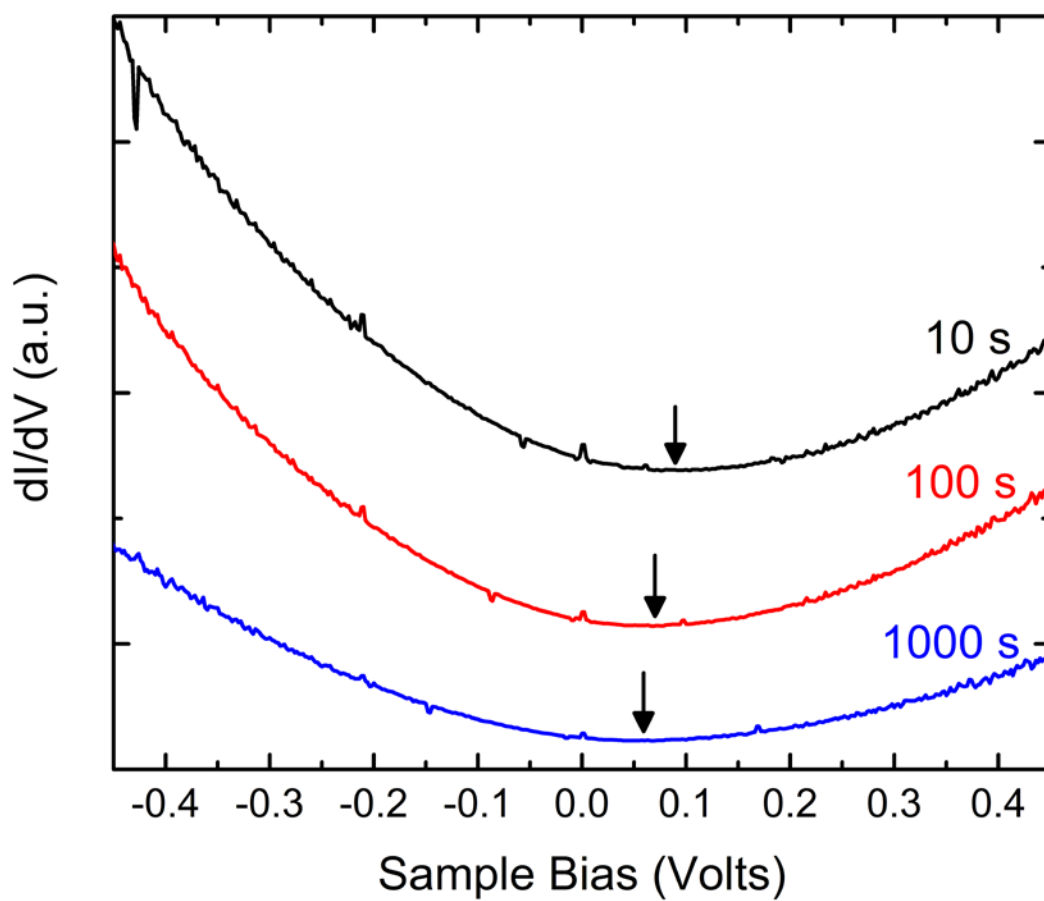


Figure 4.14. $G(V)$ for tunnel junctions of 4-I benzoic acid with Au top electrodes. Exposure to a 10^{-4} M solution of 4-I was varied from 10, 100, and 1000s. Arrow indicates $G(V)_{\min}$.

coverage increases and the $G(V)_{\min}$ for 10, 100, and 1000 seconds were 115, 77, and 66 mV, respectively. This seems to indicate that a higher coverage 4-I molecules on the surface inhibits the Au from penetrating. The more it inhibits the penetration, the less the asymmetry in the tunnel barrier. When these $G(V)$ results are compared with those with samples made with Pb top electrodes (in Section 4.3), it is evident that the $G(V)_{\min}$ have a more positive shift with Au for all exposure times. This indicates that Au penetrates the SAMs and adsorb on hydroxyls more than Pb for a given exposure time.

Tunnel junctions made from 4-SH benzoic acid and Au top electrodes were fabricated and the $G(V)$ results are shown in Figure 4.15. The conductance curve is highly asymmetric and the $G(V)_{\min}$ is at positive bias, which is opposite to the case with Pb top electrodes (see Figure 4.9). To gain a better understanding, an IETS spectrum was recorded. Figure 4.16 shows the region between 1000 and 3500 cm^{-1} . The peaks shown at 1379, 1568, and 3037 cm^{-1} correspond to the $\nu_s(\text{COO})$, $\nu_{as}(\text{COO})$, and $\nu(\text{CH})$ vibrational modes, respectively.¹¹⁵ Most important, the vibrational mode at 2540 cm^{-1} corresponding to the $\nu(\text{SH})$ mode is absent. The results from these two experiments indicate that while some Au bonds with S, much of it also penetrates the SAM and adsorbs on the polar hydroxyl groups causing a shift in the barrier asymmetry to positive bias.

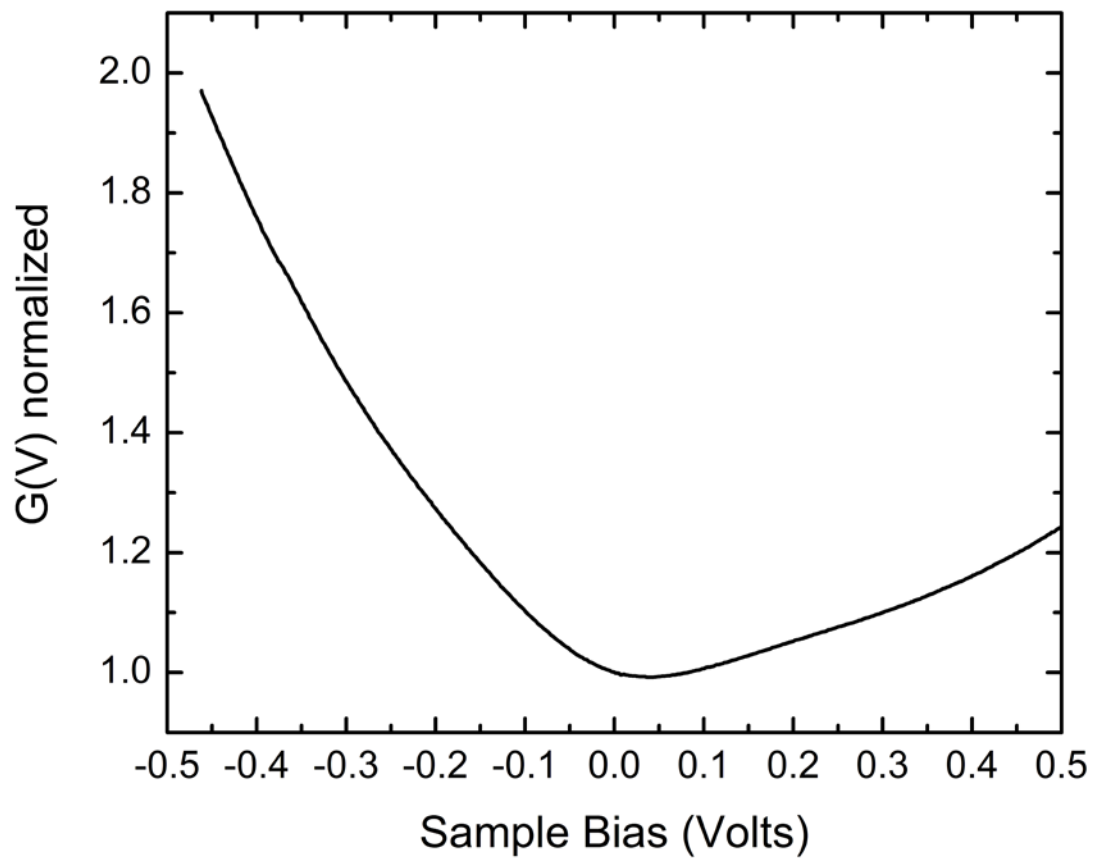


Figure 4.15. $G(V)$ for 4-SH benzoic acid with Au top electrodes.

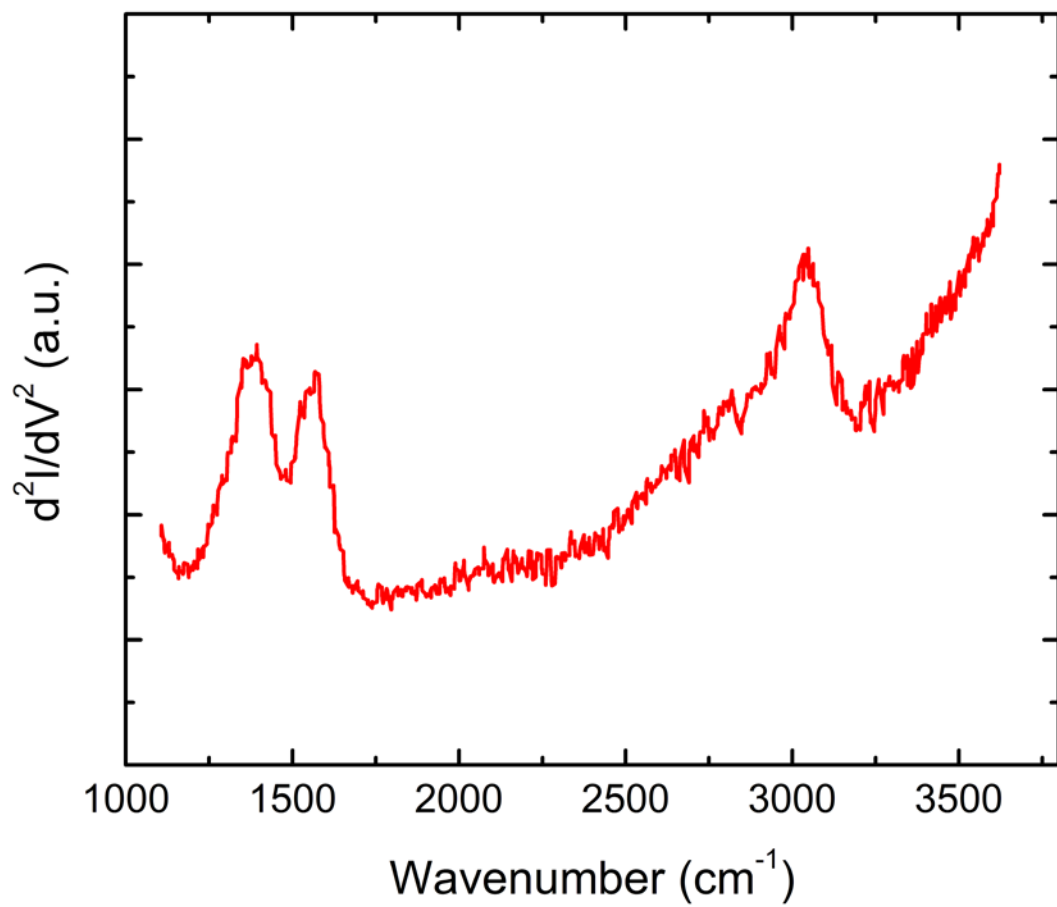


Figure 4.16. IETS of 4-SH benzoic acid with Au top electrodes taken at 4K with an 8 mV ac modulation.

Section 4.6 Conclusions

The tunneling spectroscopy results from this chapter indicate that the nature of the metal molecule interface is sensitive to the identity of both the para-substituent and the top metal electrode. When Pb is used directly on top of an air oxidized aluminum surface, polar hydroxyl groups induce a large barrier asymmetry causing a shift in the $G(V)_{\min}$ to high positive bias. Once a para-substituted benzoic acid monolayer is placed in the tunnel junction, the size of the para-substituent determines the amount of penetration of Pb through the SAM. Larger para-substituents like iodo or cyano inhibit penetration of the Pb, while smaller substituents like fluoro or chloro do not. Some para-substituents are reactive, namely thiol groups. When Pb is deposited onto 4-SH benzoic acid, S-Pb bonds form and the barrier asymmetry is completely reversed shifting the $G(V)_{\min}$ to negative bias.

When hot metals such as Ag or Au are used as the top electrode, the metals completely penetrate the SAMs regardless of the identity of the para-substituent. Even in the case with 4-SH and Au where Au-S bonds form, much of the Au penetrates the monolayer and adsorbs on top of hydroxyl groups. This causes a shift to the positive bias for the $G(V)_{\min}$, indicating that the overall barrier asymmetry has the barrier height of the

monolayer-top metal interface higher in energy than the Al-AlO_x interface.

CHAPTER 5 - TUNNELING SPECTROSCOPY OF ALKANOIC ACID MONOLAYERS

5.1 Introduction

This chapter presents the results from a tunneling spectroscopy study of alkanolic acid SAMs in tunnel junctions with Co, Ni, and Ag top metal electrodes. The general goal of this chapter is to understand how changing the terminal substituent affects tunnel junctions. In particular, we would like to understand how the well-packed alkyl chains inhibit metal penetration compared to the benzoic acid monolayers described in Chapter 4. This chapter is composed of multiple sections. In Section 5.2 a brief summary of prior tunneling studies with alkanolic and phosphonic acid SAMs is given. Section 5.3 presents the results obtained when alkanolic acids were used with Co top electrodes. Section 5.4 will show conductance curves for alkanolic acid SAMs with Ni and Ag top electrodes. Section 5.5 will reveal what happens when octadecylphosphonic acid is used with Co. Finally, Section 5.6 summarizes the important findings.

Section 5.2 Alkanoic and Phosphonic Acid SAMs in Tunnel Junctions

As discussed in Chapter 1, various alkanolic acid derivatives have been used in tunnel junctions for many decades. Kuhn was the first to demonstrate that the mode of transport through these long-alkyl chain monolayers was by tunneling.⁷ Since Kuhn's work, many others have studied various alkanolic acid derivatives in tunnel junctions. It was shown that alkanolic acids have a chain tilt approximately 15 to 25° from surface normal and as the chain length increases the crystalline packing increases.¹⁰ Another study looked at how the chain length affects the tilt of the SAM and how that affects the tunneling.⁴⁸ They learned that there was a difference in the tunneling between alkanolic acids with an even and those with an odd number of carbons in the backbone of the monolayer. Specifically, they found that alkanolic acids with even numbers had higher current densities than those with odd numbers of carbons in the backbone.⁴⁸ Some have studied how the terminal group, or atom facing the top metal electrode, affects molecular tunneling.^{59,60,120} For alkanethiols, in general when reactive terminal groups such as CO₂H, CO₂CH₃, OH, CN, and SH are used, the amount of penetration into the SAM is decreased. This is in contrast to non-reactive terminal groups such as CH₃ and OCH₃, where penetration has been seen with Ag, Cu, and various other

metals.^{59,60,120} Finally, it has been shown that using a soft top metal electrode, such as GaIn, decreases the amount of shorting in tunnel junctions by up to 90%.⁵³

Phosphonic acid derivatives have also been used in tunnel junctions.^{45,122-124} Early IETS work showed an absence of the bands associated with the phosphoryl group, indicating that the bonding was in the form of a tri-dentate resonance structure. Another study showed that phosphonic acid SAMs have a higher surface affinity and displace similar SAMs with carboxylic acid anchoring groups.⁷⁶ Phosphonic acid derivatives have been shown to pack better than all alkanolic acid derivatives and have a chain tilt of approximately 40° from surface normal.^{35,36,125}

The goal of this chapter is to gain an understanding into the nature of the metal-molecule interface using alkanolic acid derivatives with metals that have not been studied in detail (Co or Ni) and compare the results with similar studies with Ag top electrodes. We will also compare those results with octadecylphosphonic acid monolayers with Co top metal electrodes.

Section 5.3 Alkanolic Acid Tunnel Junctions with Co Top Electrodes

Tunnel junctions were fabricated using the methods described in Chapter 2. AlOx substrates were placed in 10⁻³ M

solutions containing heptadecanoic acid or mercaptohexadecanoic acid in ethanol for approximately 24 hours to obtain saturation coverage. After monolayer formation, 10-20 nm of Co was vapor deposited at a rate of $\sim 0.2 \text{ \AA/s}$ and capped with 50 nm of Ag. Electrical measurements were made upon venting of the chamber. $G(V)$ measurements of a representative set of results are shown in Figure 5.1. As can be seen, the $G(V)_{\text{min}}$ for heptadecanoic acid (a) and mercaptohexadecanoic acid (b) are near zero bias and with little asymmetry. The $G(V)$ curve rises much faster for mercaptohexadecanoic acid than heptadecanoic acid. Within the BDR model, this indicates that the effective tunnel barrier thickness is larger for mercaptohexadecanoic acid.⁶ This is an indication that less penetration of Co occurs past the terminal SH group. This is consistent with literature reports in which SH, a more reactive terminal group, inhibits the penetration of metals into the SAMs.^{59,60,120} The $G(V)$ data was fit using the BDR model and the results are shown in Table 5.1. As can be seen, the barrier width (d), height (Φ), and asymmetry ($\Delta\Phi$) for mercaptohexadecanoic acid are 33.9 \AA , 0.34 eV , and 0.15 eV , respectively. This compares to 27.1 \AA , 0.52 eV , and 0.09 eV for heptadecanoic acid, respectively. Each and every time tunnel junctions containing Al electrodes made from the same deposition are made for both SAMs, the data shows the barrier width is

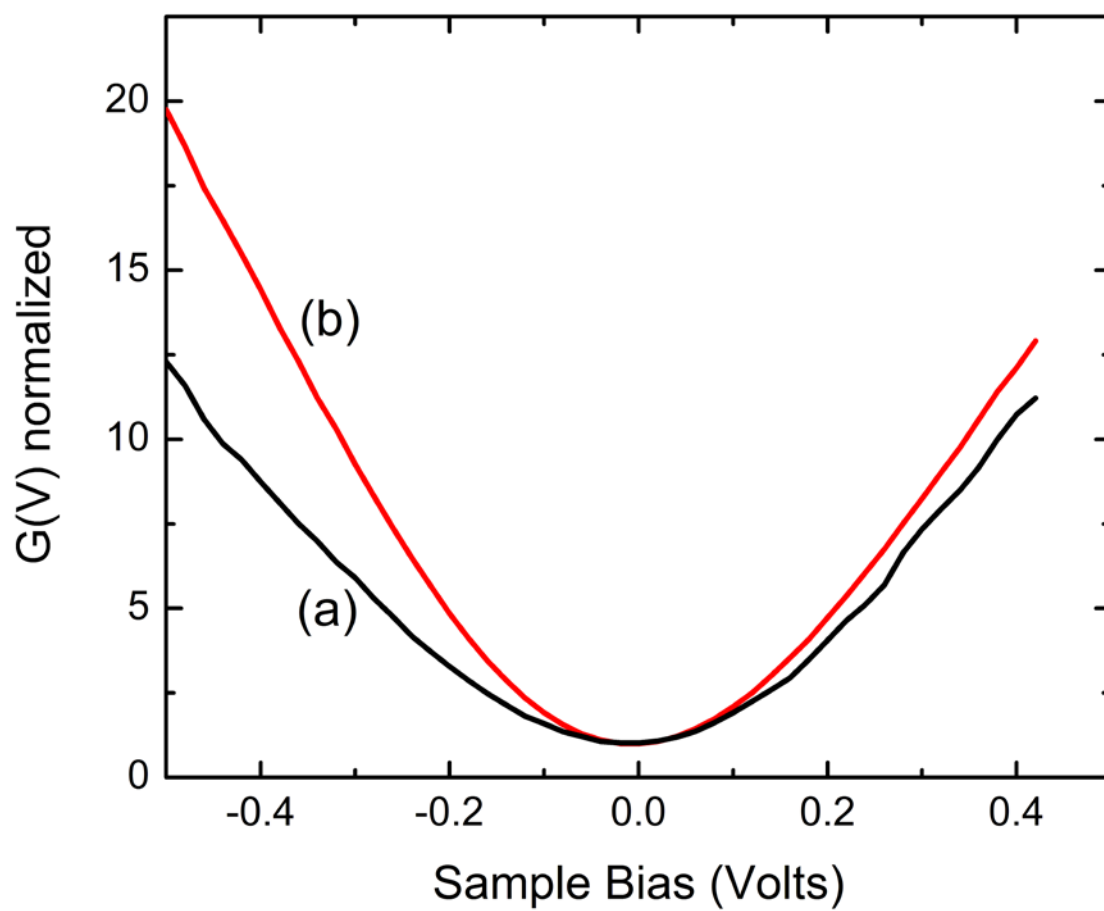


Figure 5.1. $G(V)$ for heptadecanoic acid (a) and mercaptohexadecanoic acid (b) with Co top electrodes.

Co		
	-CH₃	-SH
d (Å)	29	34
φ (eV)	0.47	0.35
Δφ (eV)	-0.05	-0.15
Ni		
	-CH₃	-SH
d (Å)	25	34
φ (eV)	0.63	0.34
Δφ (eV)	-0.41	-0.15
Ag		
	-CH₃	-SH
d (Å)	24	30
φ (eV)	0.74	0.42
Δφ (eV)	-0.09	0.22

Table 5.1 Summary of Brinkman model parameters for heptadecanoic acid and mercaptohexadecanoic acid SAMs with Co, Ni, and Ag top electrodes.

always thicker for mercaptohexadecanoic acid, which indicates less Co penetration. This is also evident when comparing the junction resistances. Figure 5.2 shows a histogram detailing the resistances of all samples made for both SAMs. The majority of the heptadecanoic acid samples made had resistances between 10^3 to 10^5 ohms while mercaptohexadecanoic acid mostly had resistances between 10^5 to 10^7 ohms. Since a 1 Å change in thickness of a tunnel barrier is equivalent to a 10 times change in the junction resistance,^{2,3} this is further evidence that on average more Co penetrates through the CH₃ group of the heptadecanoic acid than the SH group of mercaptohexadecanoic acid. Figure 5.3 shows a schematic diagram of the amount of Co penetration into the heptadecanoic acid and mercaptohexadecanoic acid based on fitting the results from Figure 5.1 to the BDR model for tunneling.⁶ As can be seen, the more reactive SH group inhibits penetration of the Co, while the less reactive CH₃ group allows it.

Section 5.4 Alkanoic Acids with Ni and Ag Top Electrodes

In a similar fashion to Section 5.3, tunnel junctions were made with Ni top electrodes. The results are shown in Figure 5.4. Both SAMs exhibit no barrier asymmetry with $G(V)_{\min}$ at zero bias. Similar to the results of Section 5.3, $G(V)$ rises much more quickly when mercaptohexadecanoic acid (b) is used

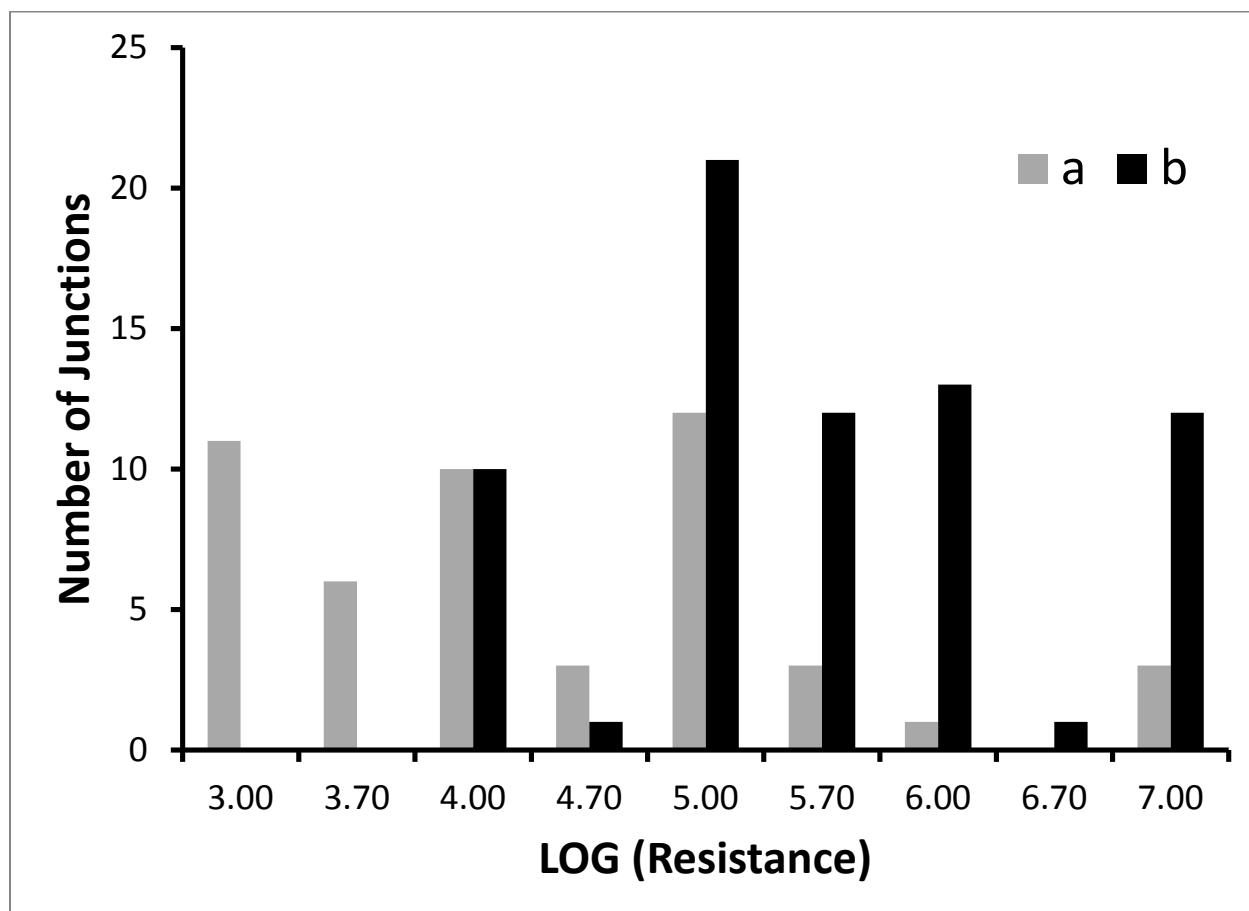
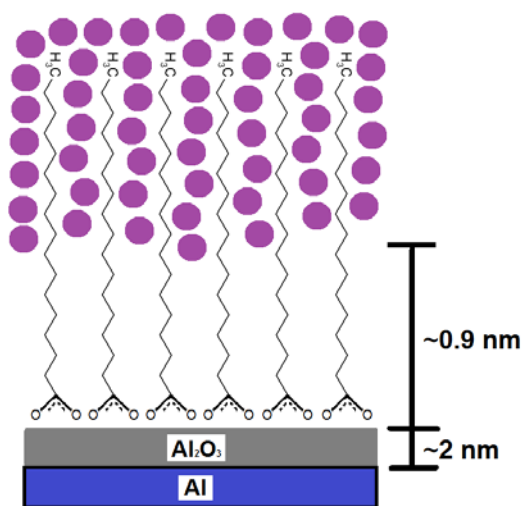


Figure 5.2. Log of resistance for all junctions with heptadecanoic acid (a) and mercaptohexadecanoic acid (b) made with Co top electrodes.

(a)



(b)

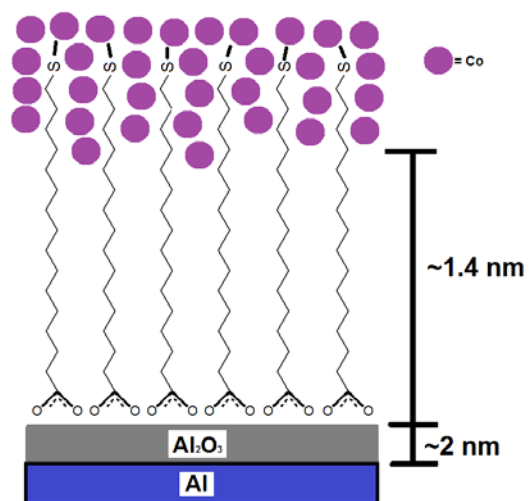


Figure 5.3. Schematic diagram of Co penetration into heptadecanoic acid SAMs (a) and mercaptohexadecanoic acid (b). Diagram is not to scale.

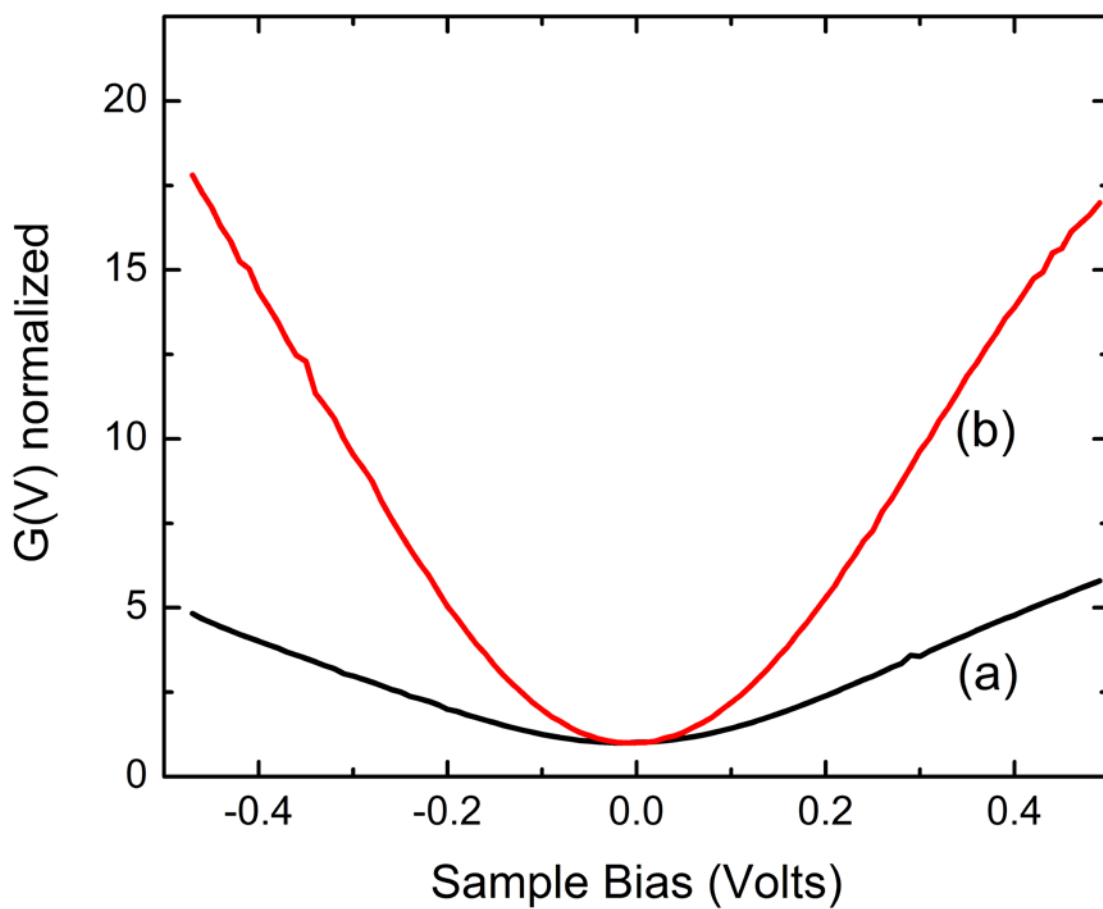


Figure 5.4. $G(V)$ for heptadecanoic acid (a) and mercaptohexadecanoic acid (b) SAMs made with Ni top electrodes.

demonstrating that the barrier width is much larger than heptadecanoic acid (a). Table 5.1 shows the BRD fits to the $G(V)$ data. Similar to the results with Co, the barrier width is much larger when mercaptohexadecanoic acid is used (34 Å for SH versus 25 Å for CH_3). Thus the SH group also inhibits penetration of the Ni into the SAM. This is consistent with results obtained by others in which SH inhibits penetration of various metals.

59,60,120

Additionally heptadecanoic acid and mercaptohexadecanoic acid SAMs were made with Ag top electrodes. The results are shown in Figure 5.5. Again the results are similar to Co and Ni in which mercaptohexadecanoic acid SAMs had a faster rise in $G(V)$ when compared with heptadecanoic acid. This data was also fit to the BDR model to extract the barrier properties and is shown in Table 5.1. Again, SH SAMs show a much larger barrier thickness than CH_3 with a thickness of 30 Å versus 24 Å. This is further evidence demonstrating that SH terminated SAMs do a better job at inhibiting the penetration of Ag into the monolayer when compared with CH_3 .

It is important to note that the data shown for tunnel junctions from this section is from one data set. The results with Ag and Ni top electrodes have do not have statistical relevance. What is most important to understand is that the data

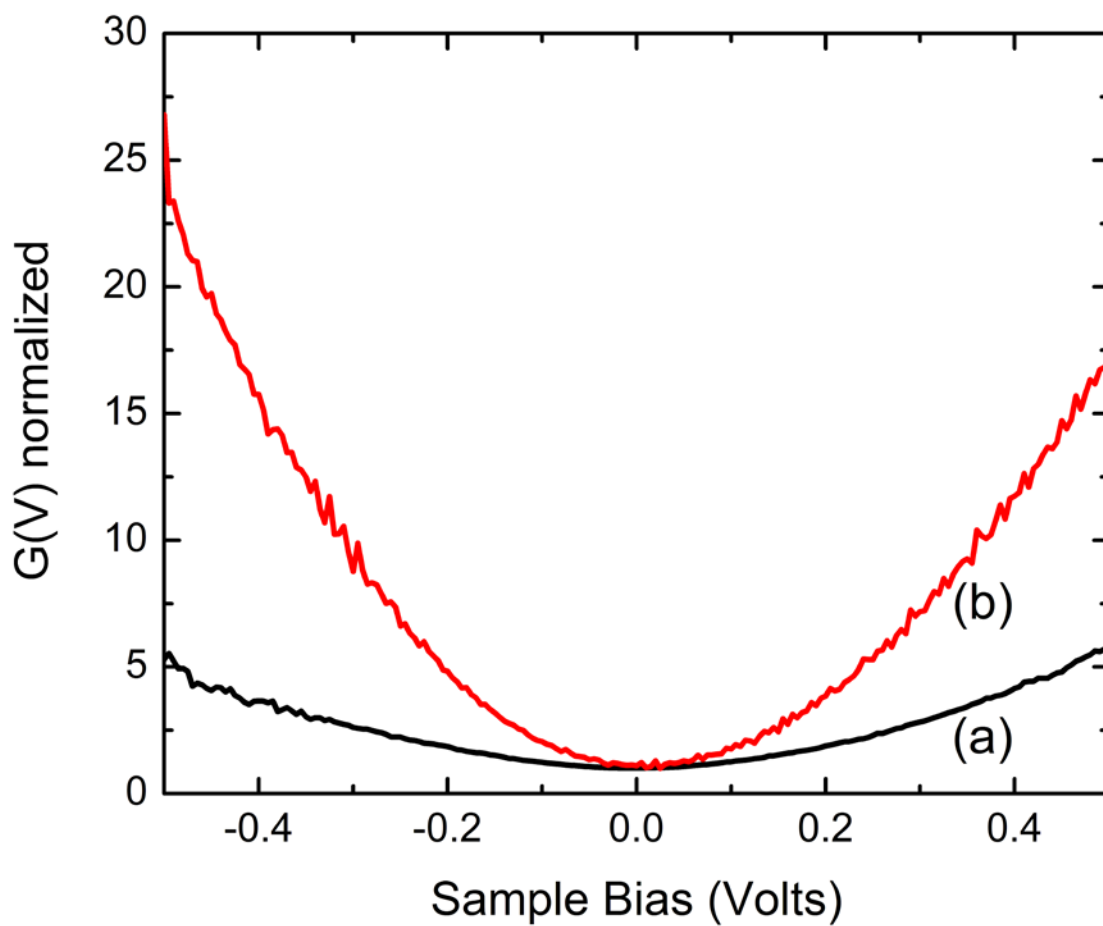


Figure 5.5. $G(V)$ for heptadecanoic acid (a) and mercaptohexadecanoic acid (b) with Ag top electrodes.

shown in this section follows the trend of the data shown with Co top electrodes in which the SH terminal group inhibits penetration of the top metal through the SAM more than the CH₃ terminal group.

Section 5.5 Tunnel Junctions Made with Octadecylphosphonic Acid

AlO_x substrates were also prepared with octadecylphosphonic acid monolayers in a similar method described in Chapter 2. Contact angles and XPS results given in Chapter 3 indicate that octadecylphosphonic acid forms dense monolayers completely displacing any surface contamination. Electrical measurements were made on samples made with Co top electrodes. The $G(V)$ results are shown in Figure 5.6. As can be seen, there is little asymmetry and a large parabolic rise in the conductance. When this data is fit using the BDR model, the barrier width, height, and asymmetry are 37 Å, 0.28 eV, and 0.22 eV respectively. Another group studying octadecylphosphonic acid SAMs measured a length of 18 Å on a mica surface.¹²⁵ Using the XPS data for the AlO_x thickness from Chapter 3 and a length of 18 Å for octadecylphosphonic acid, the composite barrier thickness should be approximately 42 Å. This shows that even when a SAM with very high packing density is used, there is still some penetration of the Co metal into the SAM.

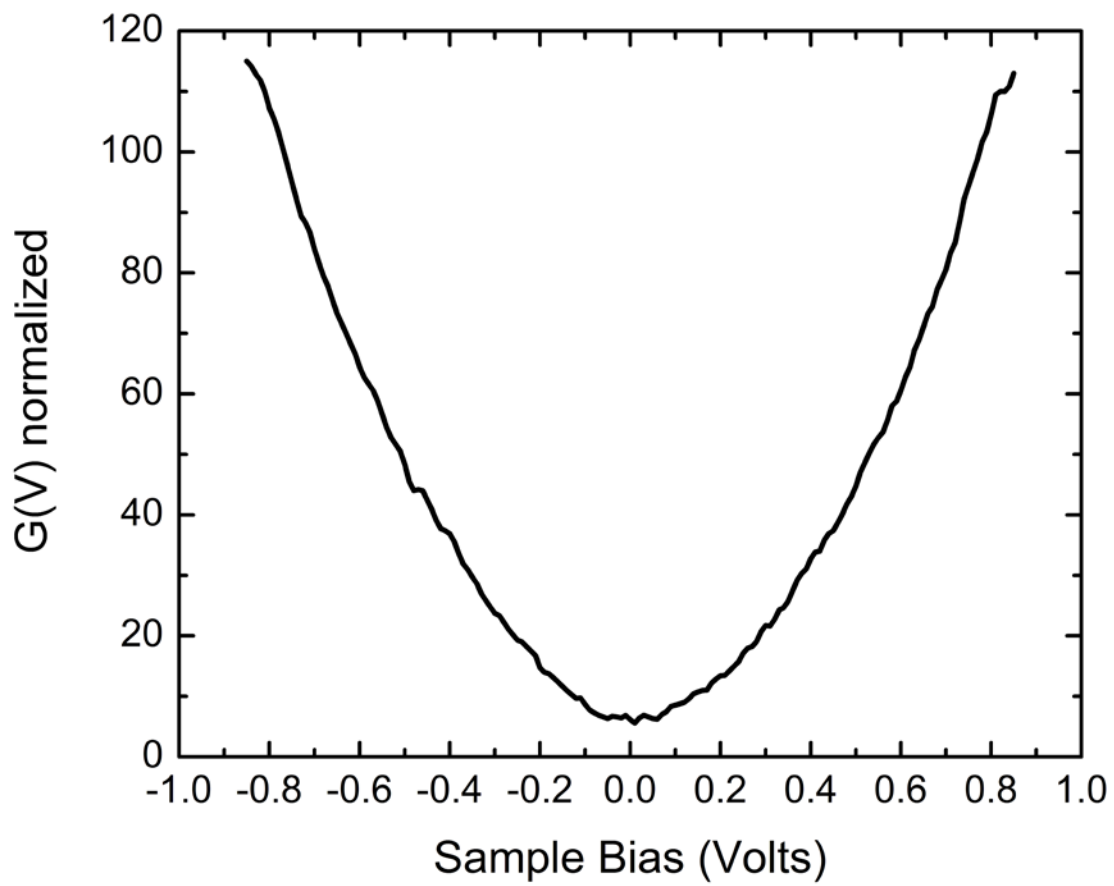


Figure 5.6. $G(V)$ for octadecylphosphonic acid with Co top electrodes.

Section 5.6 Conclusions

The work from this chapter has demonstrated that more a more reactive terminal group such as SH inhibits penetration of Co, Ni, and Ag through the alkanolic acid SAMs. The opposite is true with a CH₃ terminal group. This is evident when comparing G(V) results from both sets of samples made with the same bottom electrode.

When octadecylphosphonic acid SAMs are used in tunnel junctions, there is a much larger effective barrier width. This is evident when G(V) measurements were fit to the BDR model resulting in a barrier width of 37 Å. This is much larger than any other SAMs we studied but still shows that some penetration of Co still occurs.

CHAPTER 6 - CONCLUSIONS AND FUTURE WORK

Section 6.1 Conclusions

The main goal of this dissertation was to gain a better fundamental understanding of how the metal-molecule interface affects electron transport in tunnel junctions. This goal was achieved through surface characterization and tunneling spectroscopy studies on a range of carboxylic and phosphonic acids placed in tunnel devices and with a variety of top metal electrodes. The insight gained from this study is summarized below.

Contact angle and XPS results presented in Chapter 3 reveal a clear picture of the adsorption kinetics and adsorption geometry for benzoic acid derivatives on AlO_x substrates, respectively. Benzoic acids chemisorb to AlO_x surfaces as a carboxylate with the aromatic plane perpendicular to the surface. Using the water contact angle and XPS results, a saturation coverage of 2.7×10^{14} molecules cm⁻² was determined. This agrees well with another published report for 4-Br on AlO_x that calculated 2.3×10^{14} molecules cm⁻² using neutron activation analysis.¹⁸ At saturation coverage, benzoic acids and hydroxyls groups are present in an approximate ratio of 1:1. Contact angle

measurements of long alkyl chain SAM derivatives reveal a better packing density than benzoic acids. XPS results showed that the relative ratios between carbon species prove the molecules remain intact with relatively no contamination present.

Tunneling spectroscopy results from Chapter 4 indicate that the nature of the metal-molecule interface is sensitive to the identity of both the para-substituent and the top metal electrode. When Pb is deposited directly on top of an air oxidized aluminum surface, polar hydroxyl groups induce a large barrier asymmetry that leads to a shift in the $G(V)_{\min}$ to high positive bias. Once a para-substituted benzoic acid monolayer is placed in the tunnel junction, the size of the para-substituent determines the amount of Pb penetration through the SAM. Larger para-substituents such as iodo or cyano inhibit Pb penetration, while smaller substituents like fluoro or chloro do not. Some para-substituents can be reactive, namely thiol groups. When Pb is deposited onto 4-SH benzoic acid, S-Pb bonds form and the barrier asymmetry is completely reversed and shifts the $G(V)_{\min}$ to negative bias.

When hot metals such as Ag or Au are used as the top electrode, the metals completely penetrate benzoic acid SAMs regardless of the identity of the para-substituent. Even in the case with 4-SH and Au where a Au-S bond forms, much of the Au penetrates the monolayer and adsorbs on top of hydroxyl groups.

This causes a shift to positive bias for the $G(V)_{\min}$, indicating that the overall barrier asymmetry has a barrier height of the monolayer-top metal interface higher in energy than the Al-AlO_x interface.

Tunneling spectroscopy results on alkanolic acid derivatives from Chapter 5, support the information learned from Chapter 4. When reactive end groups such as thiol are used, penetration of hot top metals such as Co, Ni, or Ag can be decreased. When non-reactive end groups such as CH₃ are used, penetration of the top metal occurs much more.

Section 6.2 Future Work

There are many possible paths to take with this project going forward. Long chain alkanolic acids with terminal halogen substitutions can be studied in tunnel junctions with various top metal electrodes. Here the effect of atomic size on the amount of top metal penetration can be studied and compared with results from Chapters 4 and 5. It is very likely that larger terminal halogens like iodo prevent top metal penetration more than a smaller terminal halogen such as fluoro.

Additionally, the effect of carboxylic and benzoic acid derivatives on spin polarized tunneling can also be studied. These monolayers can be placed in tunnel junctions containing ferromagnetic electrodes. Once placed in these junctions, a

fundamental study to measure tunneling magnetoresistance (TMR) can be done. Effects such as top metal penetration or terminal group reactivity may play a role in TMR. One group has already demonstrated TMR possibilities with phosphonic acid SAMs on LSMO with Co top electrodes.⁴⁵ Various other SAMs could be used to gain a better understanding into this.

The Meservey-Tedrow experiment,¹²⁶ which require junctions with ultrathin (4 nm) Al bottom electrodes, could be done to measure the absolute sign and magnitude of the spin-polarization with these SAMs and ferromagnetic top electrodes. Unfortunately, this experiment must be done at < 1K and high magnetic fields, so it is very challenging.

REFERENCES

1. de Broglie, L. *Ann. De Physique* **1925**, 3, 22-128.
2. Engel, T.; Reid, P. *Physical Chemistry*; Pearson: San Francisco, 2006; pp 337-351.
3. Wolf, E. L. *Principles of Electron Tunneling Spectroscopy*; Oxford University Press: New York, 1985.
4. Giaever, I. *Phys. Rev. Lett.* **1960**, 5, 147-148.
5. Simmons, J.G. *J. Appl. Phys.* **1963**, 34, 1793-1803.
6. Brinkman, W.F.; Dynes, R.C.; Rowell, J.M. *J. Appl. Phys.* **1970**, 41, 1915-1921.
7. Mann, B.; Kuhn, H. *J. Appl. Phys.* **1971**, 42, 4398-4405.
8. Allara, D.L.; Nuzzo, R.G. *Langmuir* **1985**, 1, 52-66.
9. Chen, S.H.; Frank, C.W. *Langmuir* **1989**, 5, 978-987.
10. Tao, Y.T. *J. Am. Chem. Soc.* **1993**, 115, 4350-4358.
11. Thompson, W.R.; Pemberton, J.E. *Langmuir* **1995**, 11, 1720-1725.
12. Ulman, A. *Chem. Rev.* **1996**, 96, 1533-1554.
13. Oberg, K.; Persson, P.; Shchukarev, A.; Eliasson, B. *Thin Solid Films* **2001**, 397, 102-108.
14. Lim, M.; Feng, K.; Chen, X.; Wu, N.; Raman, A.; Nightingale, J.; Gawalt, E.; Korakakis, D.; Hornak, L.; Timperman, A. *Langmuir* **2007**, 23, 2444-2452.
15. Kummert, R.; Stumm, W.; *J. Colloid Interface Sci.* **1980**, 75, 373-385.
16. Groff, R.P. *J. Catal.* **1983**, 79, 259-263.

17. Koutstaal, C.A.; Ponec, V. *Appl. Surf. Sci.* **1993**, *70*, 206-210.
18. Sondag, A.H.; Raas, M.C. *Appl. Spectrosc.* **1989**, *43*, 107-113.
19. Korman, C.S.; Coleman, R.V. *Phys. Rev. B* **1977**, *15*, 1877-1893.
20. Muldoon, F.; Dragoset, R.A.; Coleman, R.V. *Phys. Rev. B* **1979**, *20*, 416-429.
21. Korman, S.; Lau, J.C.; Johnson, A.M.; Coleman, R.V. *Phys. Rev. B* **1979**, *19*, 994-1014.
22. Lau, C.; Coleman, R.V. *Phys. Rev. B* **1981**, *24*, 2985-2995.
23. Taylor, C.E.; Schwartz, D.K. *Langmuir* **2003**, *19*, 2665-2672.
24. Salomon, A.; Boecking, T.; Seitz, O.; Markus, T.; Amy, F.; Chan, C.; Zhao, W.; Cahen, D.; Kahn, A. *Adv. Mater.* **2007**, *19*, 445-450.
25. Sondag, A.H.; Raas, M.C.; Touwslager, F.J. *Appl. Surf. Sci.* **1991**, *47*, 205-223.
26. Carrara, M.; Nuesch, F.; Zuppiroli, L. *Syn. Metals* **2001**, *121*, 1633-1634.
27. Nuesch, F.; Carrara, M.; Zuppiroli, L. *Langmuir* **2003**, *19*, 4871-4875.
28. Vilan, A.; Shanzer, A.; Cahen, D. *Nature* **2000**, *404*, 166-167.
29. Hansma, P.K. *Surf. Sci.* **1975**, *52*, 211-216.
30. Elam, J.W.; Nelson, C.E.; Cameron, M.A.; Tolber, M.A.; George, S.M. *J. Phys. Chem. B* **1998**, *102*, 7008-7015.
31. Hotchkiss, P.; Jones, S.; Paniagua, S.; Sharma, A.; Kippelen, B.; Armstrong, N.; Marder, S. *Acc. Chem. Res.* **2012**, *45*, 337-346.
32. Ramsier, R.D.; Henriksen, P.N.; Gent, A.N. *Surf. Sci.* **1988**, *203*, 72-88.

33. Davies, P.R.; Newton, N.G. *Appl. Surf. Sci.* **2001**, *181*, 296-306.
34. Pellerite, M.J.; Dunbar, T.M.; Boardman, L.D.; Wood, E.J. *J. Phys. Chem. B* **2003**, *107*, 11726-11736.
35. Novak, M.; Jager, C.; Rumpel, A.; Kropp, H.; Peukert, W.; Clark, T.; Halik, M. *Org. Electron.* **2010**, *11*, 1476-1482.
36. Levine, I.; Weber, S.; Feldman, Y.; Bendikov, T.; Cohen, H.; Cahen, D.; Vilan, A. *Langmuir* **2012**, *28*, 404-415.
37. Boer, B.; Hadipour, A.; Mandoc, M.M.; Woudenbergh, T.; Blom, P.W. *Adv. Mater.* **2005**, *17*, 621-625.
38. Heimel, G.; Romaner, L.; Zojer, E.; Bredas, J. L. *Acct. Chem. Res.* **2008**, *41*, 721-729.
39. Bock, C.; Pham, D.; Kunze, U.; Kafer, D.; Witte, G.; Woll, C. *J. Appl. Phys.* **2006**, *100*, 114517.
40. Gooding, J. J.; Mearns, F.; Yang, W.; Liu, J. *Electroanalysis* **2003**, *15*, 81-96.
41. Petta, J.R.; Slater, S.K.; Ralph, D.C. *Phys. Rev. Lett.* **2004**, *93*, 136601.
42. Yamada, R.; Noguchi, M.; Tada, H. *Appl. Phys. Lett.* **2011**, *98*, 053110.
43. Dediu, V.A.; Hueso, L.E.; Bergenti, I.; Taliani, C. *Nature Mater.* **2009**, *8*, 707-716.
44. Tran, T.; Quyen Le, T.; Sanderink, J.; van der Wiel, W.; Jong, M. *Adv. Funct. Mater.* **2012**, *22*, 1180-1189.
45. Galibiati, M.; Barraud, C.; Tatay, S.; Bouzehouane, K.; Deranlot, C.; Jacquet, E.; Fert, A.; Seneor, P.; Mattana, R.; Petroff, F. *Adv. Mater.* **2012**, *24*, 6429-6432.
46. Vilan, A.; Cahen, D. *Trends Biotech.* **2002**, *20*, 22-29.
47. Folkers, J.P.; Laibinis, P.E.; Whitesides, G.M. *Langmuir* **1992**, *8*, 1330-1341.

48. Thuo, M.; Reus, W.; Nijhuis, C.; Barber, C.; Kim, C.; Schulz, M.; Whitesides, G. *J. Am. Chem. Soc.* **2011**, *133*, 2962-2975.
49. Wold, D.J. and Frisbie, C.D. *J. Am. Chem. Soc.* **2000**, *122*, 2970-2971.
50. Kim, T.; Wang, G.; Lee, H.; Lee, T. *Nanotech.* **2007**, *18*, 315204.
51. Reus, W.F.; Thuo, M.M.; Shapiro, N.D.; Nijhuis, C.A.; Whitesides, G.M. *ACS Nano* **2012**, *6*, 4806-4822.
52. Nijhuis, C.; Reus, W.; Barber, J.; Dickey, M.; Whitesides, G. *Nano Lett.* **2010**, *10*, 3611-3619.
53. Chiechi, R.; Weiss, E.; Dickey, M.; Whitesides, G. *Angew. Chem. Int. Ed.* **2008**, *47*, 142-144.
54. Cui, X.; Primak, A.; Zarate, X.; Tomofohr, J.; Sankey, O.; Moore, A.; Moore, T.; Gust, D.; Harris, G.; Lindsay, S. *Science* **2001**, *294*, 571-574.
55. Selzer, Y.; Salomon, A.; Cahen, D. *J. Phys. Chem. B* **2002**, *106*, 10432-10439.
56. Engelkes, V.B.; Beebe, J.M.; Frisbie, C.D. *J. Am. Chem. Soc.* **2004**, *126*, 14287-14296.
57. Xiao, X.; Xu, B.; Tao, N.J. *ACS Nano* **2004**, *4*, 267-271.
58. Chu, C.; Na, J.S.; Parsons, G.N. *J. Am. Chem. Soc.* **2007**, *129*, 2287-2296.
59. Jung, D.R.; Czanderna, A.W.; Herdt, G.C. *J. Vac. Sci. Technol. A* **1996**, *14*, 1779-1787.
60. Maitani, M. M.; Allara, D. L. *Top. Curr. Chem.* **2012**, *312*, 239-273.
61. Zhu, Z.; Daniel, T.A.; Maitani, M.; Cabarcos, O.M.; Allara, D.L.; Winograd, N. *J. Am. Chem. Soc.* **2006**, *128*, 13710-13719.
62. Smith, D. *Thin Film Deposition Principles and Practice*; McGraw-Hill: USA, 1995.

63. Kreil, J.; Ellingsworth, E.; Szulczewski, G. *J. Vac. Sci. Technol. A* **2013**, *31*, 06F107.
64. Olefjord, I.; Mathieu, H.; Marcus, P. *Surf. Interf. Anal.* **1990**, *15*, 681-692.
65. Hansma, P.; Coleman R. *Science* **1974**, *184*, 1369-1371.
66. Cassie, A.B.; Baxter, S. *Trans. Faraday Soc.* **1944**, *26*, 546-551.
67. Brown, J. *Molecular Spectroscopy*; Oxford: New York, 1998.
68. Lambe, J.; Jaklevic, R.C. *Phys. Rev* **1968**, *165*, 821-832.
69. Wang, Y.; Mallik, R.; Henriksen, P. *Rev. Sci. Instrum.* **1993**, *64*, 890-895.
70. Bell, A.; Hair, M. *Vibrational Spectroscopies for Adsorbed Species*; American Chemical Society: USA, 1980.
71. Yates, J.; Madey, T. *Vibrational Spectroscopy of Molecules on Surfaces*; Plenum Press: New York, 1987.
72. Schroder, D. *Semiconductor Material and Device Characterization*, 2nd Ed., John Wiley & Sons: New York, 1998.
73. Hoque, E.; DeRose, J.A.; Hoffmann, P.; Mathieu, H.J.; Bhushan, B.; Cichomski, M. *J. Chem. Phys.* **2006**, *124*, 174710.
74. Pertays, K.M.; Thompson, G.E.; Alexander, M.R. *Surf. Interface Anal.* **2004**, *36*, 1361-1366.
75. van den Brand, J.; Gils, S.V.; Snijders, P.C.; Terryn, H.; de Wit, J.H. *Surf. Sci.* **2004**, *235*, 465-474.
76. Liakos, I.L.; Newman, R.C.; McAlphine, E.; Alexander, M.R. *Surf. Interface Anal.* **2004**, *36*, 347-352.
77. Kebler, J.A. *Surf. Sci. Reports* **2007**, *62*, 271-303.
78. Fu, Q.; Wagner, T.; Ruhle, M. *Surf. Sci.* **2006**, *600*, 4870-4877.

79. Vinodh, M.S.; Jeurgens, L.P. *Surf. Interface Anal.* **2004**, *36*, 1629-1636.
80. van den Brand, J.; Snijders, P.C.; Sloof, W.G.; Terryn, H.; de Wit, J.H. *J. Phys. Chem. B* **2004**, *108*, 6017-6024.
81. Reiche, R.; Yubero, F. Espinos, J.P.; Gonzalez-Elipe, A.R. *Surf. Sci.* **2000**, *457*, 199-210.
82. McCafferty, E.; Wightman, J.P. *Surf. Interface Anal.* **1998**, *26*, 549-564.
83. Chen, X.; Luais, E.; Darwish, N.; Ciampi, S.; Thordarson, P.; Gooding, J. *Langmuir* **2012**, *28*, 9487-9495.
84. Barriet, D.; Yam, C.M.; Shmakova, O.E.; Jamison, A.C.; Lee, T.R. *Langmuir* **2007**, *23*, 8866-8875.
85. Martz, J.; Zuppiroli, L.; Nuesch, F. *Langmuir* **2004**, *20*, 11428-11432.
86. Dulcey, C.; Georger, J.; Chen, M.; McElvany, S.; O'Ferrall, C.; Benezra, V.; Calvert, J. *Langmuir* **1996**, *12*, 1638-1650.
87. Koh, S.; McDonald, K.; Holt, D.; Dulcey, C. *Langmuir* **2006**, *22*, 6249-6255.
88. Kim, J.K.; Jang, J.S.; Lee, J.H.; Jun, C.S. *Anal. Chem.* **2009**, *81*, 8519-8522.
89. Clark, D.T.; Kilcast, D.; Adams, D. B.; Musgrave, W.K. *J. Electron Spectrosc. Relat. Phenom.* **1972**, *1*, 227-250.
90. Bertinchamps, F.; Poleunis, C.; Grégoire, C.; Eloy, P.; Bertrand, P.; Gaigneaux, E. M. *Surf. Interface Anal.* **2008**, *40*, 231-236.
91. Petitto, S.C.; Marsh, E.M.; Langell, M.A. *J. Phys. Chem. B* **2006**, *110*, 1309-1318.
92. Sloan, D.; Sun, T.M.; Ihm, H.; White, J.M. *J. Phys. Chem. B* **1998**, *102*, 6825-6830.
93. Kong, Z.; Wang, Q.; Ding, L. *Appl. Surf. Science* **2009**, *256*, 1372-1376.
94. Liu, Q.; Xu, Z. *Langmuir* **1995**, *11*, 4617-4622.

95. Colapietro, M.; Domenicano, A.; Ceccarini, G.P. *Acta Cryst.* **1979**, *35*, 890-894.
96. Colapietro, M.; Domenicano, A. *Acta Cryst.* **1982**, 1953-1957.
97. Ohkura, K.; Kashino, S.; Haisa, M. *Bull. Chem. Soc. Japan* **1972**, *45*, 2651-2652.
98. Nygren, C.L.; Wilson, C.C.; Turner, J.F. *J. Phys. Chem A* **2005**, *109*, 2586-2593.
99. Baldea, I.; Schimmelpfennig, B.; Plaschke, M.; Rothe, J.; Schirmer, J.; Trofimov, A.; Fanghanel, T. *J. Electron Spec. Rel. Phenom.* **2007**, *154*, 109-118.
100. Lide, D. *CRC Handbook of Chemistry and Physics*; 81st ed. CRC Press: Boca Raton, FL, 2000.
101. Manocha, A.S.; Park, R.L. *Appl. Surf. Sci.* **1977**, *1*, 129-141.
102. Lichtman, D.; Craig, J.H.; Sailer, V.; Drinkwine, M. *Appl. Surf. Sci.* **1981**, *7*, 325-331.
103. Shalvoy, R.B.; Fisher, G.B.; Stiles, P.J. *Phys. Rev. B* **1977**, *15*, 1680-1697.
104. Bocking, T.; Salomon, A.; Cahen, D.; Gooding, J.J. *Langmuir* **2007**, *23*, 3236-3241.
105. Floyd, R.B.; Walmsley, D.G. *J. Phys. C: Solid State Phys.* **1978**, *11*, 4601-4614.
106. Gloos, K.; Koppinen, P.J.; Pekola, J.P. *J. Phys. Condens. Matt.* **2003**, *15*, 1733-1746.
107. Kirtley, J.R.; Hansma, P.K. *Phys. Rev. B* **1975**, *12*, 531-536.
108. Geiger, A.L.; Chandrasekhar, B.S.; Adler, J.G. *Phys. Rev.* **1969**, *188*, 1130-1138.
109. Vaynzof, Y.; Dennes, T.J.; Schwartz, J.; Kahn, A. *Appl. Phys. Lett.* **2008**, *93*, 103305.
110. Kim, E.G.; Brédas, J.L. *Org. Electron.* **2013**, *14*, 569-574.

111. Son, I.; Kim, M.; Koh, H.; Kim, K. *Catalysis Lett.* **2001**, *75*, 191-197.
112. Bogdanchikova, N.; Meunier, F.; Avalos-Borja, M.; Breen, J.; Pestryakov, A. *Appl. Catalysis B* **2002**, *36*, 287-297.
113. She, X. Flytzani-Stephanopoulos, M. *J. Catalysis* **2006**, *237*, 76-93.
114. Lide, D. *CRC Handbook of Chemistry and Physics*; 86th ed. CRC Press: Boca Raton, FL, 2005.
115. Monjushiro, H.; Murata, K. Ikeda, S. *Bull. Chem. Soc. Jpn.* **1984**, *57*, 2428-2434.
116. Lin, L.; Wang, C.K.; Luo, Y. *ACS Nano* **2011**, *5*, 2257-2263.
117. Krauss, T.; Wise, F. *Phys. Rev. B* **1997**, *55*, 9860-9865.
118. Cao, H.; Wang, G.; Zhang, S.; Zhang, X. *Nanotech.* **2006**, *17*, 3280-3287.
119. Zemlyanov, D.; Savinova, E.; Scheybal, A.; Doblhofer, K.; Schlogl, R. *Sur. Sci.* **1998**, *418*, 441-456.
120. Allara, D. *Biosens. & Bioelectron.* **1995**, *10*, 771-783.
121. Ramsier, R.; Henriksen, P.N.; Gent, A. *Surf. Sci.* **1988**, *203*, 72-88.
122. Henriksen, P.; Gent, A.; Ramsier, R.; Alexander, J. *Surf. Interf. Anal.* **1988**, *11*, 283-286.
123. Rampulla, D.; Wroge, C.; Hanson, E.; Kushmerick, J. *J. Phys. Chem. C* **2010**, *114*, 20852-20855.
124. Templeton, M.; Weinberg, W. *J. Am. Chem. Soc.* **1985**, *107*, 97-108.
125. Woodward, J.; Ulman, A.; Schwartz, D. *Langmuir* **1996**, *12*, 3626-3629.
126. Meservey, R.; Tedrow, P. *Phys. Rep.* **1994**, *238*, 173-243.